STUDIES OF DISSIMILAR ALUMINIUM ALLOY IN FRICTION STIR WELDING

A thesis submitted in fulfilment of requirements for the Degree of

Doctor of Philosophy

in

Mechanical Engineering

Submitted by

ARUN GUPTA
2K12/PHDME/09

Under the Supervision of

Prof. Vipin

DEPARTMENT OF MECHANICAL ENGINEERING
DELHI TECHNOLOGICAL UNIVERSITY
(FORMERLY DELHI COLLEGE OF ENGINEERING)
Bawana Road, Delhi-110042, India

2021

DECLARATION

I declare that the work presented in this thesis entitled “Studies of Dissimilar Aluminum alloy in Friction Stir Welding”, is submitted to the Department of Mechanical Engineering, Delhi Technological University, Delhi, India, for the award of the Doctor of Philosophy degree in Mechanical Engineering, is my original research work carried out by me. The work presented in this thesis has not been submitted to any other university or institution for the award of any degree or diploma.

ARUN GUPTA

CERTIFICATE

This is to certify that the Ph.D. thesis entitled **"Studies of Dissimilar Aluminum alloy in Friction Stir Welding"** being submitted by Mr. ARUN GUPTA for the award of degree, Doctor of Philosophy in Mechanical Engineering, Delhi Technological University, Delhi, India, is a bonafide record of original research work carried out by him under my guidance and supervision. The work presented in this thesis has not been submitted to any other university or institution for the award of any degree or diploma.

Prof. VIPIN
Department of Mechanical Engineering,
Delhi Technological University,
Delhi

ACKNOWLEDGMENT

First and foremost, I am thankful to the Almighty God for his blessings for the completion of my Ph.D. work.

I express my gratitude to Prof. Yogesh Singh, Vice-chancellor, Delhi Technological University, Delhi for providing this opportunity to carry out this work in this prestigious institute.

I thank Prof. R.S Mishra, DRC Chairman, Department of Mechanical, Production, Industrial, and Automobile Engineering, Delhi Technological University, Delhi for his support to finish this work.

With pleasure, I express my highest gratitude to my supervisor, Prof. Vipin for his proficient guidance, intelligent approach, constructive critique, wholehearted and ever available help, which had been the primary impetus behind the research. He is not only the supervisor; he is my guardian, without whose wise advice and able guidance, it would have been impossible to complete this course. He always stood by me and brought me positivity and hope when things didn't seem to be in favor. I respect the contributions of his valuable time and ideas to make my Ph.D. productive.

I am highly grateful to my parents and my wife for their love and blessings to see me scaling greater heights of life and their motivation and encouragement, the pursuit of this Ph.D. work would have never been possible. I thank them for caring and encouraging me throughout my research work.

I am thankful to Dr. Yuvraj, faculty, Department of Mechanical, Production, Industrial, and Automobile Engineering, Delhi Technological University, Delhi for generous sharing of his knowledge.

I am thankful to Mr. Netram, senior mechanic, Department of Mechanical, Production, Industrial, and Automobile Engineering, Delhi Technological University, Delhi for generous help in the lab during experimental work.

ARUN GUPTA

ABSTRACT

Welding processes have evolved as one of the joining processes with enormous potential. Different welding processes have been invented during their evolution. The increasing use of aluminum has become the basis of the need for a welding process to overcome the limitations of the fusion welding techniques. The invention of a Solid-state welding technique-Friction Stir Welding (FSW) has eliminated the drawbacks of fusion welding associated with the solidification process.

In the present research work, an empirical model has been established between tool rotational speed, tool traverse speed, tilt angle and square pin size, and mechanical properties (ultimate tensile strength, yield strength, percentage elongation and impact strength) of friction stir welded dissimilar non-heat-treatable AA 5083-O and heat treatable AA 6082-T651. Statistics based Response surface methodology (RSM) was used to perform the experiments, analyze the results and optimize the parameters. Rotatable Central composite design (CCD) was used to generate the design matrix to perform the welding. Four factors each having five levels were used to generate the matrix. Total thirty-one experiments without blocking were performed on a dedicated friction stir welding machine. The levels of the tool rotation speed and traverse speed were decided from extensive trial runs performed on a customized friction stir welding machine. The square pin size and tilt angle levels were decided after the literature review.

The experiment runs were performed randomly to eliminate inherent error in experimentation. The dissimilar base plates were welded, standard samples were machined, mechanical properties were measured and empirical relationships were established. Adequacy of the empirical relationship was ensured by Analysis of variance (ANOVA). The significance of various parameters was found and non-significant factors were omitted from the empirical model to generate reduced models. The optimized values of the input parameters were obtained to maximize each response. Multi-objective optimization was used to find the optimized values of input parameters to obtain maximum values of all responses simultaneously. Microhardness values were measured and found that on the retreating side its value minima points were found between heat affected zone and thermo mechanical affected zone.

Residual stresses of friction stir welded plates were measured and analyzed using the cos (α) method. X-Ray Diffraction (XRD) analysis was performed to check the crystallinity of the joints and base material. The scanning electron microscopy (SEM) analysis of the nugget zone of welded plates was performed. Optical microscopy of various microscopic zones was also analyzed.

TABLE OF CONTENTS

LIST OF FIGURES

LIST OF TABLES

ABBREVIATIONS & NOMENCLATURE

FSW	Friction Stir Welding
CCD	Central Composite Design
XRD	X-Ray Diffraction
JCPDS	Joint Committee on Powder Diffraction Standards
WEDM	Wire Electrical Discharge Machining
RSM	Response surface methodology
AS	Advancing Side
RS	Retreating Side
NZ	Nugget Zone
TMAZ	Thermo Mechanical Affected Zone
HAZ	Heat Affected Zone
GTAW	Gas tungsten arc welding
GMAW	Gas metal arc welding
RPM	Revolutions Per Minute
ASTM	American Society for Testing and Materials
ANOVA	Analysis of Variance

UTS	Ultimate Tensile Strength
YS	Yield Strength
EL	Percentage Elongation
I	Impact Strength
Y	A variable representing response surface
R	Tool rotation velocity
W	Tool traverse velocity
T	Tool tilt angle
S	Square pin side length
2-D	Two Dimensional
3-D	Three Dimensional
SS_{pe}	Sum of Square due to Pure Error
SS_{lofit}	Sum of Square Due to Lack of Fit of Model
SS_T	Total Sum of Squares
SS_{reg}	Sum of squares due to the regression
SS_{res}	Sum of Square due to Residual
PC	Personal computer

CHAPTER 1: INTRODUCTION

Welding processes have brought a milestone change in metal joining processes and their applications. Welding has almost eradicated some other metal joining processes (like riveting), due to its various advantages. Enormous research has been observed in the field of welding since its onset. One of the variants of joining techniques is solid-state welding. FSW established in The Welding Institute (TWI) in last decade of the 20th century, is a solid-state welding technique that is comparatively recent than other welding methods [1]. FSW is generally preferred to weld softer materials like aluminum alloys, copper alloys, magnesium, zinc, and lead; however, FSW has evolved tremendously and is being used to join steel, titanium and other hard materials [2]–[4].

1.1 INTRODUCTION TO FSW TECHNIQUE

Before FSW, the base plates may be cleaned with a suitable chemical to eradicate dust, and lubricant, if any. During welding a rotating tool with a probe is inserted into the base plate joint contour to a specific depth, allowing the shoulder to touch the plates. The base plates tend to separate apart when the pin plunges into the joint. The plates are clamped firmly on the anvil to evade the separation of the joining edges during FSW. A vertical load is essential to retain contact between the shoulder and base plate interface. The tool shoulder compresses and confines plasticized material flow close to the shoulder location and prevents material circulation to the outside of the joint. The tool is made to stay for a suitable period, to heat & yield the base material. The tool is then moved along the faying line, as shown diagrammatically in Figure 1. The Traverse movement of the tool generates a

load along the joint line, known as a transverse load. FSW machine must be rigid enough to withstand the forces necessary to perform the welding operation.

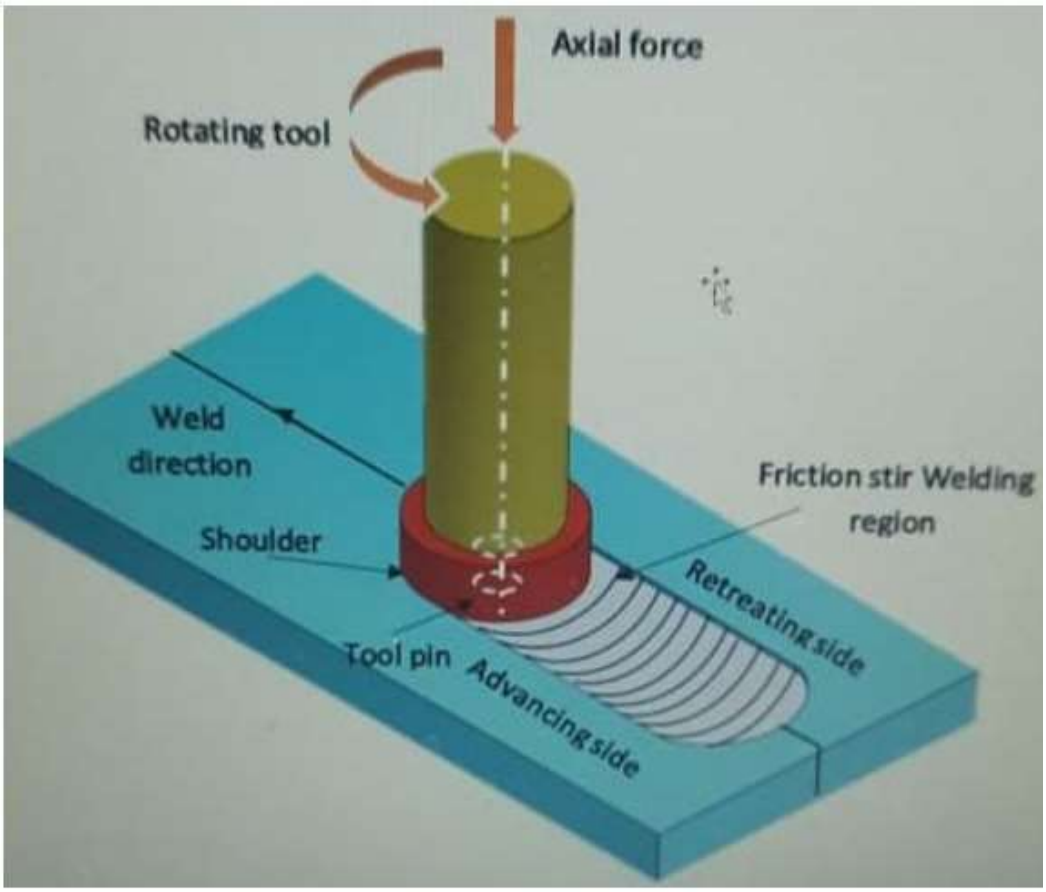

Figure 1.1: FSW diagram representation

Plunging of tool pin into the base plates causes localized frictional heat that softens and plasticizes the metal located round the pin. An amalgamation of tool rotation and linear movement results in shift of metal to the trailing edge of the probe from the forward edge of the probe and therefore filling the hole in the vacant zone created by plunging of the pin as the tool moves forward. The appropriate combination of FSW parameters results in a defect-free joint. Based on the direction of tool rotation and transverse movement, the advancing side (AS) and the retreating side (RS) may be defined. The AS shows the hand where the rotation direction of the

tool and its transverse movement coincide. The RS specifies the base plate region opposite to the AS, where the way of the tool rotary motion is opposite to that of its linear motion [5].

Based on microstructure, the Friction Stir welded material cross-section is classified into four zones: (a) Weld nugget zone (NZ), (b) Thermomechanical affected zone (TMAZ), (c) Heat affected zone (HAZ), and (d) Unaffected metal or base material. The NZ is positioned at the center of the transverse section and manifested by a recrystallized grains zone. NZ is generated by plastic deformation attributable to frictional heat created by the transverse movement of the rotating probe along the joint line. TMAZ is positioned adjacent to NZ on both sides. It is characterized by lesser temperature variation and deformation than NZ. The thermal cycle affects HAZ in terms of mechanical and microstructural changes. However, no plastic deformation is discovered in this zone[6]. Parent material, positioned away from the joint line on either side, gets heat up during FSW but does not show any variation in texture and mechanical properties. All the zones have been manifested in Figure 1.2.

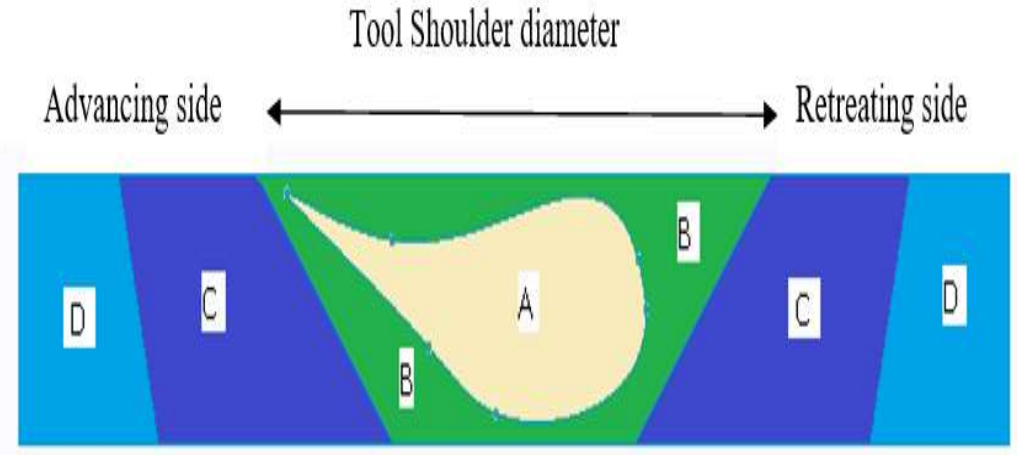

Figure 1.2: Different areas in the weld cross-section: A-NZ, B-TMAZ, C- HAZ, and D- Parent material

1.2 ADVANTAGES, LIMITATIONS AND APPLICATIONS OF FSW

There are numerous benefits of FSW as compared to different welding techniques. However, it has certain limitations also. The benefits and limitations of FSW have been enlisted as:

1. FSW is a welding technique in which no melting of base material is required.
2. As base material is not melted in FSW, distortion due to heat is less as compared to fusion welding processes.
3. The microstructure obtained is fine in friction stir welded joint as compared to other welding techniques.
4. The shielding gasses and filler materials are not required, as in the case of some other welding techniques like GTAW and GMAW.
5. FSW joints have excellent mechanical characteristics.
6. Excellent metallurgical properties are obtained in the friction stir welded joints.
7. No fumes and spatter are produced during the FSW, as in the case of Fusion welding.
8. A minor surface cleaning of the base material is required before FSW as compared to other welding processes.
9. Any kind of harmful gasses is not emitted.
10. The post-weld processes like removal of slag and brushing are eliminated.

Despite numerous advantages, FSW has few limitations also and are listed as:

1. A withdrawal hole exists where the plunged tool is lifted upwards from the weld material at the end of FSW.

2. Proper clamping arrangement is required for holding the base plates/sheets to prevent the separation of the two faying surfaces during the welding.
3. The transverse speed in FSW is lower than that in other welding processes.
4. The thin sheets may get rolled while performing the FSW.
5. The FSW is difficult for non-linear weld joints and plates of variable thickness.
6. FSW joints are vulnerable to imperfections if process variable values are not appropriate.

There are numerous applications of FSW in various industries and are given as:

1. Automotive: Vehicle body, bumpers, suspension parts, and wheel parts are welded by FSW.
2. Shipbuilding: Aluminum being light in weight is used in marine applications. FSW is used in marine industries to weld aluminum panels for the freezer and ship decks. Pre-manufactured panels of friction stir welded aluminum alloy are used at dockyards for boats and ships [7].
3. Railway: Panels of aluminum for rolling stock-based applications in various railway industries are being welded by FSW [8].
4. Aerospace: In aerospace applications, high-strength aluminum is welded by FSW for making huge size tanks for satellite launch vehicles. Lightweight airframe structures of various aircraft are manufactured by friction stir welded aluminum[9].
5. Fabrication: Panel for honeycomb and speaker's halves are welded by FSW.

1.3 ALUMINUM ALLOYS CLASSIFICATION

FSW of Aluminum alloys has been accepted in various industrial applications. Aluminum strength is one-third of the steel, but concurrently, steel is three times heavier than aluminum. Also, aluminum has three times the thermal expansion coefficient than steel. An appropriate design with aluminum alloy may compensate for its strength with lesser weight. Table 1.1 manifests physical characteristics of the aluminum.

Table 1.1: Aluminum alloys physical characteristics

Young's modulus	Density	Melting point	Boiling point	Thermal Conductivity	Crystal structure
70 GPa	2700 kg/m^3	660.32 °C	2470 °C	237 W/(m·K)	FCC

Aluminum alloys are broadly classified into two types: Wrought aluminum and cast aluminum.

The wrought aluminum alloys are hot or cold worked but not remelted. Cast aluminum is remelted before the recasting. Based on their affinity for heat treatment, aluminium alloys are categorized into heat treatable and non-heat-treatable aluminum alloys. [10]. The non-heat-treatable alloys are non-precipitation hardening alloys [6].

The wrought Aluminum designation and heat treatability have been presented in Table1.2. The designation system of the cast aluminum is presented in Table 1.3. The temper designation of aluminum alloy has been presented in Table 1.4.

Table 1.2: Designation structure of wrought aluminum Alloy

Alloy	Principal alloy elements	Affinity to heat treatment
1xxx	Aluminum, 99.00 % minimum or more	Non-Heat treatable
2xxx	Copper	Heat- treatable
3xxx	Manganese	Non- Heat- treatable
4xxx	Silicon	Non- Heat-treatable
5xxx	Magnesium	Non-Heat- treatable
6xxx	Magnesium and silicon	Heat-treatable
7xxx	Zinc	Heat-treatable
8xxx	Other elements	Heat-treatable/ Non Heat-treatable

Table 1.3: Designation structure of cast aluminum Alloy

Alloy	Principal alloy elements
1xx.x	Pure Aluminum
2xx.x	Copper
3xx.x	Silicon plus Copper and/or magnesium
4xx.x	Silicon
5xx.x	Magnesium
6xx.x	Unused Series
7xx.x	Zinc
8xx.x	Tin
9xx.x	Other elements

Table 1.4: Temper designation of the Aluminum alloy

Letter	First digit	Second digit
"F"-"as fabricated"		
"0"- "annealed"		
“H" -"strain hardened"		
H1	1- strain hardened only	
H2	2- strain hardened and partially annealed	
H3	3- strain hardened and stabilized	
HX2		2- 1/4 hard
HX4		4- 1/2 hard
HX6		6- 3/4 hard
HX8		8- full hard
HX9		9- Extra hard
"W" "solution heat-treated"		
"T" "thermally treated to produce stable tempers other than F, O or H" Applies		
“T1”	1- After cooling from an elevated temperature shaping process, such as extruding, naturally aged	
“T2”	2-After cooling, cold worked from an elevated temperature forming phase and then aged naturally.	
“T3”	3-solution heat treated, cold worked and naturally aged	
“T4”	4-solution heat processed and naturally aged	
“T5”	5- Artificially aged from an elevated temperature forming phase until the cooling	
“T6”	6-solution heat-treated and artificially aged	

“T7”	7-solution heat-treated and stabilized (over-aged)	
“T8”	8-solution heat treated, cold worked and artificially aged	
“T9”	9-solution heat treated, artificially aged and cold worked	
“T10”	10-cold worked after cooling from an elevated temperature shaping process and then artificially aged.	
		The second digit reveals the variance in a basic treatment

* Additional digits signify relief from stress. TX51 - Stretching stress relieved, TX52 - Compressing stress relieved

1.4 FSW TOOLING

The tool is an essential part to conduct FSW. An FSW tool necessarily has a projected part known as a pin, and a shoulder. The tool performs three main functions: workpiece heating, metal movement to generate the joint, and hot material containment below the shoulder. The workpiece heating is triggered by friction between the rotating pin and base plates, shoulder and workpiece. Pin generates localized heating and the workpiece's plastic deformation. The shoulder augments the heat generated and the area of the plasticized material.

1.4.1 TOOL SIZE

The tool's pin height is slightly lower as compared to thickness of the base metal. Further, probe height depends on the distance between its end and the base plate support anvil, and tilt angle [6]. The Diameter of the pin should be large enough to abide by the various loads and unite the joint. Concurrently, the diameter should be small enough so as not to rupture the base material. Generally, the pin diameter for a circular pin is kept comparable to the work piece sheet thickness.

1.4.2 TOOL MATERIAL

FSW tool material selection depends upon various criteria, including different process parameters. The characteristics of the FSW tool, which influence its material selection, are given as:

Tool refractory behavior: The tool material must have excellent strength to abide by various loads at elevated temperatures on the tool during FSW. In some applications, the tool is applied with a cycle of high temperature during FSW and cooling period during idle time. The tool microstructure may vary during this thermal cycle and lead to diminishing its mechanical properties and cause reduced property of the joint. Thus, tool material must be thermally stable at a higher temperature. The tool wear at an elevated temperature must not occur during FSW. Wear may amend tool dimensions or shape during welding and may consequence in faulty joints.

At higher temperatures, the tool material must not chemically react with the base material. The Chemical reaction contaminates the tool and the base plate material and may cause defective joints. A high thermal expansion coefficient of tool metal may increase the dimensions of the tool after the pin plunges into the base material joint. If the tool dimensions increase beyond a threshold value, FSW may result in a faulty joint. Therefore, the tool material must be thermally stable at high temperatures.

Sometimes, tool pin and shoulder may be of different materials (in case of retractable pins), different thermal expansion in pin and shoulder may induce various stresses in the tool and may cause its failure. A suitable provision should be incorporated to overcome the above difficulty.

As there is an abrupt change in dimensions of the tool at the boundary of the shoulder and probe, stress concentration may occur. During the transverse movement of the tool, various loads are induced in the tool, and due to stress concentration, the load intensity increases. Thus, the tool for FSW must have a high fracture toughness value at elevated temperatures.

Tool behavior at ambient temperature: The tool material, initially in the form of a billet, is machined and processed to attain certain design features of the pin and shoulder. The material must have good machinability to acquire the design features. Tool material must have higher hardness than the base material to perform successful FSW. The tool is heat-treated after machining to attain the required hardness value. The tool material's mechanical properties at ambient temperature play an essential role in successful FSW. The tool metal should have sufficient strength at the ambient temperature, to counter sudden load that induces in it during the initiation of plunging into the base material. The tool material should be cost-effective and readily available in the market for procurement and continuous supply for the welding.

1.5 EFFECT OF PROCESS PARAMETERS

Although various parameters influence the performance of the FSW, the four most effective factors are rotation velocity, linear velocity, tilt angle & axial force.

1.5.1 TOOL ROTATION VELOCITY

Tool Rotational velocity is a crucial factor affecting the heat caused by abrasion between the pin and base material, and the shoulder with the base plates. Depending upon an appropriate range of other essential factors setting, a suitable range of tool RPM may be decided. Its high value may cause high friction heat,

more severe blending and stirring, and hence a defective joint. Too low tool speed will not be sufficient to produce necessary heat and stirring to plasticize the base metal and result in a faulty joint [11] [12].

1.5.2 TOOL LINEAR SPEED

It is also a critical process parameter, and its suitable range depends upon a combination of other process parameters. It's very low value augments the frictional heat due to more time available to transfer the heat to a lesser volume of the base material and lead to a defective joint. High linear speed reduces the amount of heat transfer into the joint and base material may not yield properly and lead to a faulty joint.

1.5.3 TILT ANGLE OF TOOL

It represents an angle which the tool direction makes with a vertical axis, in the reverse direction to that of tool movement. The tool tilt angle from zero to three degrees has been found suitable for defect-free joints [13]. The tool tilt angle enhances the pressure on the metal beneath the tool and is responsible for the thinning. A tilt angle beyond the appropriate value may lead to a flash of material along the joint.

1.5.4 AXIAL FORCE

An axial force is the vertical downward load that compresses the tool shoulder against the base plate. A sufficient axial force is required to generate a defect-free joint. Too low axial force may consequence in defects underneath the friction stir welded surface. The defects may be in the form of voids due to insufficient stirring. If the axial force is more than a suitable value, it may lead to the thinning of the joint due to burr formation during FSW. The mentioned distinct

value of axial force depends upon other process parameters. At higher axial force, a higher FSW speed may be achieved [14].

1.6 ORGANIZATION OF THE THESIS

Chapter 1 depicts the introduction, micro structural zones, advantages, limitations and applications of FSW. The classification of aluminum alloys and their temper designation system has been described. The various aspects of the tool and its material have been discussed. Essential factors of FSW and their influence on the welded joints have been depicted.

Second chapter includes literature review on the influences of FSW parameters on the properties of the joint. A review of the FSW of aluminum alloys has been depicted. Subsequently, research gaps along with the objectives of this research have been elaborated.

. Chapter 3 presents the configurations of the machines used during the research work. Detailed specifications of machine setup have also been presented.

Chapter 4 presents the methodology and data collection, the main essence of the research. It includes various procedures, adopted DOE techniques, design matrices, Mechanical testing.

Chapter 5 depicts the result and discussions of experiments performed in the present research. The influences of the various independent factors on the mechanical properties and interaction effects are presented. Optimization of the various parameters for maximum responses has been presented. Further interpretation of various graphical representations has been elucidated. Micro hardness of the joints and their analysis has been described. This chapter includes

the characterization of the welded joints. X-Ray Diffraction and residual stresses of the welded joint have been analyzed.

Chapter 6 explains the conclusion part of this study and includes the future scope for further work.

CHAPTER 2: LITERATURE REVIEW

The literature review is an integral part of the research work. In the present research, an ample literature survey was conducted to conclude the research objectives. A part of the survey has been presented in this chapter. The literature review on the effect of process parameters on joint properties has been presented. A review of the FSW of aluminum alloys has been depicted. Subsequently, research gaps along with the objectives of this research have been elaborated.

2.1 EFFECT OF VARIOUS PARAMETERS ON JOINT PROPERTIES

FSW involves complex material stirring and movement around the tool pin and beneath the shoulder. FSW process, tool, clamp, and base material related parameters influence various joint properties. Process parameters include tool rotation speed, tool traverse speed, axial force, and tool tilt angle. Further tool material & geometry, along with process parameters are influential to affect the quality of joint [11], [12], [15], [16].

Tool material, the diameter of the shoulder, profile of pin, penetration or plunge depth, shoulder overlap, base material, and tilt angle are the parameters that command FSW. It was investigated that the ratio of tool shoulder diameter to pin diameter plays an important role to ensure the quality of joints. Also, the material on the advancing side dominates the stir zone [17].

FSW was performed on AA6061 & AA7075 to evaluate the effect of material position and traverse speed Material position on mechanical properties, hardness and metallurgical properties. The welded tensile specimens were fractured

from HAZ on the AA 6061 side. It was concluded that the maximum traverse speed and positioning of AA6061 on the advancing side attribute to the maximum tensile strength of the FSW joints. [18]. The literature review for various parameters has been presented subsequently.

2.1.1 TOOL ROTATION SPEED AND WELDING SPEED

A suitable combination of tool rotation speed and welding speed consequences in defect-free friction stir welded joint. FSW of 6063-T5 and 6063-T3 was performed and microstructure and hardness were examined at variable tool RPM. The hardness values remained almost unaffected at variable tool RPM. It was also observed that post-weld aging increases the hardness but the variation in hardness was not appreciable at lower tool RPM [19].

The effect of FSW traverse speed on the defect development, crack initiation, and fatigue life of friction stir welded 5083 H-321 has been observed. Traverse speed between eighty to two hundred millimeters per minute has been considered for the study. The kissing bond defect and crack initiation were observed in the weld and reduced fatigue life resulted [20].

A study on the effect of two different welding speeds on fatigue strength of AA 6082-T4 and 6082-T6 was performed. The fatigue tests were performed on the FSW joints and the results were compared to Metal Inert Gas-pulse (MIG-pulse) welded and Tungsten Inert Gas (TIG) welded joints fatigue strength. At low welding speed better FSW joints fatigue strength was manifested than that of MIG-pulse welding and TIG Welding [21].

It was investigated that the microstructure, mechanical properties and residual stresses are more prominently affected by thermal changes than the

mechanical distortion due to friction stir welding of AA 5083 performed at different welding speeds [22].

AA 6061-T651 FSW plates were examined for tensile properties at variable tool RPM and traverse speed. It was concluded that at a lower traverse speed and high tool RPM, tensile elongation was low due to coarse precipitate clustering. [11].

AA5083-H32, AA 6061-T651, and AA 7075-T6 were examined for tensile properties after FSW at different tool RPM and traverse speeds. The tensile elongation of Al 6061-T651 and Al 7075-T6 showed an increasing trend with an increase in traverse speed or/and reduction in tool RPM. AA5083-H32 did not show any noteworthy change in tensile properties with variation in welding parameters [24].

The effect of welding speed and tool RPM on mechanical properties and fatigue strength of friction stir welded AA 6056 was analyzed. Microhardness, tensile properties, low cycle fatigue and high cycle fatigue test were evaluated. It was concluded that the joint at 56 mm/min had given the best low cycle fatigue results. The microstructure of the Cross-section of the joint was also evaluated. [25]

The influence of welding speed and tool RPM on the tensile properties of FSW 6061-T651 was observed. The nature of fracture surfaces was also observed and it was concluded that the traverse speed is most influential among the considered welding parameters in the assessment of tensile properties and fracture modes [26].

The outcome of varying tool RPM and traverse speed of FSW AA 6061-T651 on tensile properties and microstructure was analyzed. It was observed that the tensile strength was raised with an increase in traverse speed. Tensile strength independence of variation in tool RPM was concluded[27].

Tensile properties and microstructure of friction stir welded AA 2219-T6 were analyzed. Tensile properties showed a rise and sharp fall trend with an increase in tool RPM within the considered range. The variation of microhardness in different zones of FSW was observed [28].

A model relating torque to tool RPM & traverse speed has been developed. The tool RPM variation results in an exponential decay pattern whereas traverse speed varies linearly to the torque. The results were applied to a wide range of tool RPM & traverse speed. The model of tool power & specific energy was evaluated from the said model to cover the complete range of tool RPM [29].

AA 6082-T651 plates were friction stir welded and their mechanical properties and microstructure were analyzed. The maximum tensile strength of the plates was 85 percent of that of base material at 500 tool RPM and 25 mm /min linear speed. Microstructural analysis revealed the uniformity in the distribution of grain in the nugget zone. Scanning electron microscopy images indicated the ductile failure [30].

Friction stir welded magnesium alloy sheets were examined for tensile properties, microstructure, and strain hardening nature at different traverse speed, tool RPM, and pin thread orientations. The left-handed thread pin rotating clockwise produced better joints and tensile properties than the right-handed pin rotating clockwise. Base material was fractured in ductile mode while the joints failed with cleavage like flat faces [31].

Dissimilar alloys AA5083 - AA6082 were friction stir welded and an investigation to generate a process window to produce the sound-quality welds, was performed. Nine combinations of three different tool RPM & traverse speed were made. AA5083 was positioned on the advancing side and AA6082 on the retreating

side and another way also. After various tests, it was concluded that the heat beneath the tool is dependent on the tool RPM more significantly than on traverse speed [32].

FSW of dissimilar AA2024-T351 and AA6056-T4 was performed. Tool RPM and traverse speed were varied, keeping axial force and tool configuration constant. Optimization based on microhardness testing and macrostructure analysis was performed; it was observed that at 800 rpm and traverse speed of 150 mm/min, good quality joints were produced. Tensile testing manifested that the joint strength was ninety percent of the 6056-T4 base material. It was concluded that the failure occurs in the maximum strength reduction region due to the annealing phenomenon [21].

The influence of tool RPM and traverse speed on residual stresses of dissimilar FSW AA 5083 and AA 6082 was observed and also compared with similar constituent's aluminum alloys. The residual tensile stress was induced near the joint line and balanced by compressive residual stress in the unaffected base material. Tool RPM was found more influential than traverse speed for the assessment of residual stress [34].

Thermal stresses and mechanical properties were assessed based on tool RPM and traverse speed of FSW of AA 2014. The finite element method-based model was generated and validated by experimental results performed by the design of experiments. It was concluded that the temperature under the tool was dependent on the tool RPM substantially than on traverse speed [35].

The effect of the ratio (tool RPM and welding speed) on the mechanical properties of different zones of FSW AZ31 alloy has been investigated. The shear punch test was used to evaluate the mechanical properties. It was concluded that

with an increase in the mentioned ratio, the yield strength and ultimate tensile strength showed a slightly decreasing trend in the stir zone and TMAZ [36].

Thermal changes during the FSW and residual stresses of friction stir welded AZ31 Magnesium alloy were investigated. It was concluded that the rise in tool RPM or shoulder diameter or decrease in traverse speed resulted in an enhancement in heat generation and grain growth. The stress levels on the retreating side were reported to be higher[37].

AZ31B-H24 magnesium alloy of 2 mm thickness was friction stir welded in lap joint configuration and the influence of tool RPM and pin length on the joint quality in terms of mechanical properties, microstructure, and defect formation were evaluated. The constant increase in shear load was observed with an increase in pin length. Tool RPM increment initially increased the shear load, but the further increase of the former reduced the latter [26].

AA7075-T6 was friction stir welded and the influence of the tool RPM on mechanical properties and microstructure was investigated. It was observed that tool RPM and mechanical properties are associated. With the rise in tool RPM, high peak temperature and widening of heat affected zone have been observed. [39]

Fifteen millimeters thick AA 6082 were friction stir welded with a cooling arrangement and the mechanical properties and microstructure of the joints were examined. Yield strength and elongation with cooling showed increasing and decreasing trends respectively. Traverse speed affected the width of the welded zone[40].

The weld quality of the AA 5086-H32 was examined for different values of the tool RPM and traverse speed. The value of input parameters was varied based on the “one factor at a time” method. It was concluded that tool RPM at 1000-1400 rpm

and traverse speed 60 mm/min & 60-110 mm/min traverse speed and 1000 RPM consequence in defect-free joints [41].

Underwater FSW was performed on 6082-T6 and tensile properties were examined with varying shoulder diameter, tool RPM (ω) and traverse speed, and a quadratic term of tool RPM (ω^2). A model was developed and the optimum values of these parameters were evaluated to maximize the tensile strength. It was concluded that the tensile strength of the alloy was seventy-nine percent of base metal strength [30].

2.1.2 EFFECT OF AXIAL FORCE AND TILT ANGLE

A method of assessing the torque and various forces in FSW has been depicted. FSW of 6.35 mm thick AA 6061-T6 & AA 2195-T6 plates was performed and longitudinal force, transverse force, and downward force were assessed. FSW was concluded to be more energy-efficient than other fusion welding processes under similar settings. Further, appropriate welded joints were fabricated within the range of a downward force between 10500 N and 14800 N [43].

The effect of axial force on the FSW of AA 7020-T6 was studied. The axial force was incremented continuously in the longitudinal direction, by increasing the angle between the base plate and the anvil in the vertical direction. The tool was also made to deviate in the transverse direction and a tolerance limit was evaluated to achieve a defect-free joint. The axial force was varied from 4 to 8.8 kN and observed maximum at 8.1 kN without any defective weld [44].

The effect of various input parameters was observed on mechanical strength, hardness and corrosion rate of friction stir welded AA 6061-T6. The input process parameters were traverse speed, tool RPM, axial load, probe size, shoulder size and hardness of tool. The optimum values of the input parameters were evaluated for

minimizing the corrosion rate and maximizing other output parameters using the design of experiments [45].

The axial force effect was observed on FSW AZ61A magnesium alloy and axial force was optimized for corresponding parameters. The tool RPM and traverse speed were fixed at 1200 and 90 mm / min respectively. The axial load was varied from three to seven kN. The influence of the axial load on the output parameters (tensile properties and microhardness) was evaluated [46].

The effect of the tool tilt angle on mechanical properties and microstructure of friction stir welded dissimilar materials 6061-T651 and copper was observed. The tool tilt angle was varied from zero to four degrees with 4 equal intervals. The other process parameters, tool RPM, traverse speed, probe offset and base material position were fixed. The flawless joints were obtained with tilt angles 2, 3 and 4 degrees [47].

The influence of the tilt angle on the mechanical properties and fracture position of friction stir welded polyethylene was studied. The base materials were friction stir welded with double passes & variable tilt angles. It was observed that an increment in tilt angle had reduced the thickness of the friction stir weld zone attributing to a reduction in tensile properties [48].

The effect of tool material, tilt angle, shielding gas and cooling system was observed on the friction stir welded joints of pure titanium. The titanium made shoulder and titanium carbide made probe was used for FSW. The mechanical properties of the welded joints were evaluated. Maximum mechanical properties were observed with the cooling medium as compressed air, argon as shielding gas and tilt angle of one degree [49].

Pin profile, tool RPM, traverse speed, and tilt angle have been varied and their effect on tensile properties of polypropylene composite welds has been investigated. The tool RPM of 400, 630 & 100 were employed while work traverse speeds of 8, 16 and 20 mm/min were used. Four different tool probe geometries were used for FSW while the tilt angle was kept zero, one and two degrees. It was observed that the tensile properties were enhanced with an increase in tilt angle from zero to two degrees [50].

Effects of tool tilt angle have been studied and considerable changes in mass and heat transfer characterization of weld material were observed. A computational fluid dynamics model having a geometric model & contact boundary conditions was proposed. It was concluded that due to tool tilt angle, i) more temperature is generated on the advancing side of the friction stir weld (ii) frictional load at the tool and base material interface has enhanced, & (iii) higher stirring action has occurred adjacent to the welding tool [51].

The effect of tool tilt angle variation on mechanical properties of friction stir welded AA1100 and A441 AISI was observed while maintaining other process variables (tool RPM, welding speed, tool offset & plunge depth) constant. It was observed that mechanical properties were maximum at two degrees tilt angle and equal to seventy-five percent to that of aluminum base metal. The TMAZ microstructure of AA 1100 was affected more than that of A441 AISI [52].

The effect of tool tilt angle on defect generations on friction stir welded 7 mm thick plates of AA 2219 was studied. The influence of the tilt angle on transverse force and vertical force during FSW was analyzed. The role of the tilt angle on the material flow and defect formation in FSW joints has been evaluated. It

was observed that for other similar parameters, no defect was detected at tilt angle one degree to two degrees [53].

The effect of tilt angle on lap shear strength of friction stir AA 2014-T6 has been investigated keeping other major parameters constant. It was observed that flawless joints were obtained at a tilt angle from zero to three degrees. Good quality joints were achieved at a tilt angle of two degrees and had maximum lap shear strength and microhardness [54].

AA 6061-T6 was friction stir welded and their mechanical properties were analyzed by varying tool tilt angle and tool pin profile. Tools with taper and taper threaded pins were used for FSW. It was investigated that with a rise in tilt angle the torque, axial and Z- force was increased. Tensile forces were improved with a taper screwed pin at higher tilt angles. Variations in welding forces were raised with an increase in tilt angle for the taper tool and opposite behavior was observed for the taper screw pin [43].

Two dissimilar heat-treatable aluminum alloy 5083 and 5086 were friction stir welded and the influence of variation in tool RPM, traverse speed, pin profiles, and tilt angles, on tensile properties was investigated. It was detected the variation in the above parameters had an impact on the tensile properties. Ultimate tensile strength was initially increased with a rise in tool rpm, traverse speed and tilt angle and then decrease [56].

Taguchi method was used to investigate the influence of axial force, tool RPM, traverse speed on friction stir welded RDE-40 aluminum alloy tensile strength. It was observed that all three factors influence the tensile strength of the mentioned alloy significantly. The optimum values of the input parameters were evaluated to maximize the tensile strength of RDE-40 [57].

The effect of variation in process and tool parameters on the mechanical properties of AA 7075-T6 was investigated. The process parameters, tool rpm at 1400 rpm, traverse speed at 60 mm/min and axial force at 8 kN and tool parameters, shoulder diameter at 15mm, pin diameter at 5 mm and tool hardness at 45 HRC resulted in a sound joint with maximum tensile strength as compared to other joints [58].

The acrylonitrile butadiene styrene (ABS) plates were friction stir welded with a stationary shoulder tool without any external heat source. The influence of tool RPM, welding speed, and axial force on the quality of the welded plates has been investigated. The sound welds were produced when the tool RPM and axial force had reached beyond a specific value. The defects on the retreating side stir zone were omitted when the mentioned parameters had reached beyond the threshold value [59].

FSW was performed on five different aluminum alloys (AA1050, AA6061, AA2024, AA7039 and AA7075) with different values of process parameters. The empirical relationships between base material properties and process parameters (tool RPM and traverse speed) were established for defect-free joints. It was concluded that the base material yield strength, percentage elongation and hardness affect the post-weld performance of the FSW joints [60].

Response surface methodology was used to develop a model indicating the relationship between various parameters (traverse speed, tool RPM, axial force & pin profile) and tensile strength of friction stir welded aluminum alloy AA 6061. The efficacy of the model was checked by Analysis of Variance (ANOVA) and other statistical methods. It was concluded that the developed model could be used to predict the tensile properties of welded joints with a very high confidence level [61].

T-joints of AA-5754 and polymethyl methacrylate (PMMA) were friction stir welded. Optimization of the process parameters (tool RPM, welding speed, tilt angle, and plunge depth) was performed to maximize the tensile strength and hardness of the joint. It was observed that fewer defects were developed through heat input control in the nugget zone by raising tool rpm and decreasing welding speed [62].

FSW was effectively performed on AA5052 H32 and HSLA steel IRS M42. The influence of tool speed and tilt angle on tensile and microstructural properties were observed. The sound joints were made in a very narrow band of welding speed and tilt angle values. The maximum ultimate tensile strength of the joint was observed to be 94 percent of that of AA 5052 H32 [63].

2.1.3 EFFECT OF SHOULDER CONFIGURATION AND PIN GEOMETRY

The influence of pin geometry was observed on friction stir welded AA 2014. Cylindrical pins with & without threads and taper cylindrical pins with & without screw threads were used for welding. Based on microstructure and mechanical properties, a cylindrical taper pin with threads was found to give the best results [64].

Cylindrical pin, cylindrical pin with threads, and triangular pin were used to weld AA 5083-O, AA 6061-T6, and AA 1050-H24, and their mechanical properties and microstructure were evaluated. It was observed that different pins have affected the mechanical properties of the mentioned alloys differently at different tool RPM [65].

The effect of different shoulder features on mechanical properties of 1.5 mm thick friction stir welded AA 6082-T6 has been investigated. The different tools had the following shoulder features: (i) fillet, (ii) scroll and fillet, and (iii) cavity and

fillet. The influence of the shoulder features was observed on tensile properties (transverse and longitudinal) and microhardness. It was concluded that the shoulder with fillet and cavity provided the best-welded joints [66].

The influence of variation in the welding speed, the tool dimensions, and the tool RPM on the mechanical properties of friction stir welded AA 6061-T651 was studied and it was concluded that tensile strength increased with a rise in welding speed without any interference of other factors, tool shoulder dimensions and tool RPM. The fracture occurred in a low hardness zone located in the heat-affected zone [67].

The effect of variation in tool profile and rotational speed on mechanical properties of friction stir welded AA 6061 was investigated. The welding was performed at five different tool rotation RPM. Five different shaped probes (cylindrical, taper cylindrical, threaded cylindrical, triangular and square probes) were employed for the welding. The square profile probe at 1200 rpm rotation speed was attributed to the best mechanical properties of the welded joints [68].

The influence of tool configuration on the mechanical properties and microstructure of friction stir welded aluminum alloy at constant tool RPM, linear speed, and tilt angle was studied. It was observed that 20 mm of shoulder diameter along with 6 mm of pin diameter had resulted in the least defects and best tensile properties. Further, it was concluded that the shoulder diameter of 10 mm and the probe diameter of 3 mm resulted in the least mechanical strength and defective joints [69].

Taguchi method was used to perform the FSW of AA 7075-T6 to estimate the effect of various factors (tool RPM, welding speed, plunge depth, and tool pin profile) on tensile properties. ANOVA method was used to find the significance of

various input parameters. It was investigated that the conical pin results in better joint efficiency than the square pin. Optimization for maximizing the tensile properties have been evaluated [70].

Aluminum alloy AA 6061 were friction stir welded with six tools of different shoulder feature. The tools were manufactured by the metallic layered manufacturing process. Tensile strength and other properties of the joints were evaluated to analyze the effects of shoulder features. It was concluded that tool with projected spiral shoulder consequence the best mechanical properties and surface quality [59].

The material flow of friction stir welded aluminum alloy 6082 with a tool having ridged shoulder combined with different pin profile was evaluated. The marker inserts of copper were used parallel and normal to the weld joint. It was concluded that the flow of material from bottom to top occurred due to pin movement. Square pin welded joints were observed to be sound with maximum tensile properties and uniform hardness [72].

Shoulders with four different features (concentric circle, ridge, knurling and scroll) were used to friction stir weld aluminum alloy and the respective effects on material flow, temperature variation, and axial force were observed. It was observed that the shoulder without any feature with the same diameter / larger diameter attained higher axial force, lower temperature, and comparatively high flash as compared to above mention featured shoulders. The ridge shoulder featured tool consequence in better mechanical properties and less axial force. [73].

Friction stir welding of aluminum alloy with knurling featured shoulder along with square and hexagonal pin geometries was performed. The material flow of the welded zone was analyzed using the marker insert technique. Knurling design

shoulder with square pin combination resulted in better tensile strength and hardness values [74].

The effect of tool concave angle and pin geometry on friction stir welded dissimilar aluminum alloys AA7075-T651 and AA6061 joint's mechanical and metallurgical properties was investigated. Concave shoulders with 1.5, 3.0, and 4.5 degrees angle and pin with triangular, square, and cylindrical pins were utilized. Maximum tensile strength, hardness, and bending angles were observed with a concave shoulder angle of three degrees and a square pin [75].

Ten millimeters thick Nylon 6 plates were friction stir welded with threaded pin tool at a rotational speed of 1000 rpm and traverse speed of 10 mm/min. The effect of tool rotation direction on defect formation of the welded joint was investigated. It was concluded anti-clockwise direction of the tool consequence defect-free welded joint [76].

Al–10 wt.% TiB2 metal matrix composites were friction stir welded with different tool pin geometries. The influence of tool pin geometry on mechanical and microstructural properties of welded joints was investigated. It was found that the taper pin generated a narrow stir zone than that produced by straight pins. Further, square pin produced joints with better mechanical characteristics than other pins [77].

Different pin profiles were used to perform FSW of copper and the joints were examined for comparative mechanical properties. Tools with triangular, square, pentagon, hexagonal, taper cylindrical and taper cylindrical with threads were employed to produce FSW joints. Tool speed of nine hundred RPM and traverse speed of forty millimeters per minute was used for welding. It was observed that the

square pin profile consequence in better mechanical properties and the same was confirmed by microstructural analysis [78].

The pin geometry manifests an influence on various properties of friction stir welded joints. The impact of different pin profiles on the tensile properties of welded AZ31B magnesium alloy has been investigated. The variants of cylindrical pins opted for were simple, taper and threaded. It was concluded that the taper pin had resulted in maximum tensile and best microstructural properties [79].

A three-dimensional FEM model was established to investigate the influence of the pin profile on material flow, strain and thermal distribution of friction stir welded aluminum alloy 5083. The cylindrical and square pin tools were developed for the welding. It was concluded that the square pin attributed to better results in terms of tensile properties and microstructural characteristics [80].

2.2 FSW OF ALUMINUM ALLOYS

As the aluminum alloy is lighter in weight, corrosion-resistant, and has good strength per unit weight, it is well suited to various applications in aircraft, automobiles, and maritime industries.

Marine-grade 5052 plates were Friction stir welded and a mathematical model to analyze the effect of process parameters on the mechanical properties was developed. Analysis of Variance was used to check the adequacy of the model. The response surface methodology was used to find the optimum values of the output values. Microstructure and macrostructure graphs of welded plates were also examined [81].

The weldability of the AA 2017-T351 was assessed by analyzing the relationship between process parameters and the tensile properties of the joint. It was

observed that the ratio of traverse speed to the tool rpm is optimum at 0.0666 and the ultimate tensile strength is eighty-two percent to that of the base material. The flawless joints failed at the boundary of the stir zone and TMAZ on the advancing side. The joint with flaw failed near the stir zone [82].

The tensile behavior of 6061 T4 was mapped in terms of tool rpm, linear speed, and vertical force with the help of a central composite rotatable design using twenty runs. ANOVA was used to ascertain model validity. Microstructure and fractography of the joints and fractured tensile specimens were analyzed using an optical microscope and Scanning electron microscope. Conclusions were elaborated for variation of tensile strength and elongation based on changes in input factors. Mechanical properties were optimized for different independent parameters [83].

FSW of AW7075-T651 was performed and its mechanical properties, temperature monitoring, microstructure analysis, spectroscopy, SEM analysis, and XRD analysis were performed. It was observed that the ratio of rotation speed to the rotation of linear speed does not affect the tensile strength while changes in stir zone and thermo mechanical affected zone are prominently influenced by rotational speed and linear speed [72].

Twenty millimeters thick Aluminum alloy AA 6082-T6 plates were friction stir welded and the temperature at three different locations on the tool was measured. The temperature at the shoulder circumference, the interface of tool pin and shoulder and pin tip were calculated by thermocouples. It was observed that the maximum temperature point was located at the tool pin and shoulder interface on retreating backward of the tool. The minimum temperature was found on the tooltip on the retreating front side of the tool. The consequences of the study were beneficial in

tool design, validation of temperature-based models and thermal response control [85].

AA 5083-H321 was friction stir welded using a design matrix generated by the central composite design of response surface methodology. Four input parameters tool rpm, linear speed, tilt angle and dwell period & two output parameters tensile strength and ductility were selected for the analysis. From the established empirical model, it was observed that tool rpm and tilt angle were the most influential factors than the remaining two input parameters [86].

Response surface methodology and Taguchi method were used to generate the relationship between the ultimate tensile strength of friction stir welded AA 2024-T3 and process parameters. Tool rpm, linear speed and shoulder diameter were selected as input parameters. Signal to noise ratio and ANOVA method were used to evaluate the significance of the factors. The empirical model developed was used to predict the response for the given value of input parameters. Optimum values of the independent parameters have been evaluated to find the maximum response value. It was concluded that with an increase in the tool rpm the ultimate tensile strength first increased to a maximum value and then it decreased. Further, it was observed that an increase in tool rpm or shoulder diameter consequence in an increase in grain size in the stir zone [75].

A rigid viscoplastic model FSW of aluminum alloy pipe has been developed to analyze thermal distribution, material flow and force disparity. Optimized plunge depth was predicted by simulation for weld joint fabrication. Welded joints were characterized by analyzing the impact of plunge depth on microstructure and hardness. For appropriate contact between the tool shoulder and the pipe, the plunge

depth was concluded to be 0.3 mm. Grain size increases with an increase in plunge depth from 0.3 mm to 0.5mm [88]

FSW of AA AA2219-O and AA 7475-T761 was performed to achieve similar and dissimilar alloy joints. The mechanical properties, metallurgical characteristics and fracture surfaces of the welded joints were studied. Severe plastic deformation caused grain refinement in the nugget zone. Hardness was observed minimum in the thermo-mechanical affected zone on the retreating side. The nature of fracture surfaces in similar joints was found enhanced ductile than that in dissimilar joints [89].

Thin aluminum sheets of 2024-T3 and 6082-T6 were friction stir welded to achieve similar and dissimilar joints. Mechanical properties were evaluated by static and varying load fatigue tests. Microhardness and residual stresses were also examined and analyzed for both types of joints. The residual stress nature was observed to be compressive [90].

FSW was performed to join aluminum alloy 2024 and 7075 and mechanical and microstructural properties were evaluated. The tensile test revealed that the strength in the longitudinal direction is more than that of a transverse direction. Fatigue tests were performed and results were analyzed [91].

FSW of similar and dissimilar aluminum alloys AA 5052 and AA 6061 was completed. At high tool rpm, the axial load and torque necessity was decreased. It was observed that the tensile properties of dissimilar aluminum were prominent than that of a similar welded joint of 6061. Metallurgical tests have substantially justified the outcome of tensile tests [92].

FSW of 6082-T6 and 6061-T6 was performed and their nature towards crack growth (fatigue) has been observed. For the different locations in FSW zones, the

crack propagation graph was plotted. It was observed that the 6061-T6 was less susceptible to crack propagation than other alloy friction stir joints. Further, it was concluded that the crack propagation rate for the welded joints was less than that of the corresponding base materials [93].

The tool with two shoulders also known as the bobbin tool has an advantage over convention friction stir welding. The welding zone in the joint fabricated by the bobbin tool is square as compared to triangular to that in the case of conventional FSW. The net normal forces that cancel each other originated from both shoulders. Aluminum alloy 6082-T6 was friction stir welded using the bobbin tool and tensile properties, microstructure and grain size were evaluated and compared with FSW with conventional tools [94].

The plastic nature of 5083-H111 and 6082-T6 influences friction stir weldability. The above-mentioned alloys were welded at different welding conditions. It was observed that at elevated temperature aluminum alloy 6082 showed severe flow softening under tensile force. It was concluded that AA6082 has good weldability than AA 5083 under similar weld conditions [83].

Dissimilar aluminum alloy (6082-T6 and AA 5754-H22) sheets were friction stir welded in lap joint configuration. It was intended to evaluate the effect of sheet material properties on strength of joint, fabricated by positioning different sets of base material to tool shoulder. One cylindrical and two taper cylindrical tools (of different dimensions) were used for welding. Joint strength was found independent of the tool shape when AA 6082 sheet was positioned on top, in contact with the tool shoulder. The taper cylindrical pin tool with a low value of shoulder diameter to pin diameter ratio is found most suitable for the fabrication of the welds with the same strength on advancing and retreating sides [96].

Two dissimilar aluminum alloys (AA5052-H32 and 6061-T6) were used to fabricate the FSW joint in two different positions. In one instance when the 5052 was placed on the advancing side and 6061 was placed on the retreating side, the mixing was better than another instance when the position of the alloys is reversed. It was observed that the minimum hardness of the weld joint was in the heat-affected zone of AA5052 and hence fracture was located in the same zone [97].

Aluminum alloy AA 5052 and AA6061 were friction stir welded to fabricate dissimilar joints. The influence of base material placement and tool offset on the joints mechanical properties, microstructural characteristics and thermal-based measurement of the joints was investigated. AA 6061 positioned at the advancing side resulted in better mechanical properties of the FSW joints. Irrespective of base metal placement higher peak temperature was revealed on the advancing side. Tool offset augmented advancing side metal flow in the nugget zone and constrains the material mixing [98].

Response surface methodology based central composite design was used to perform FSW of dissimilar aluminum alloy AA 7075-T651 and AA6061 by altering the levels of input process parameters, pin size, tool tilt angle and tool offset. Microhardness and ultimate tensile stress were selected as output parameters. A model was developed to correlate the input and output parameters and ANOVA was used to validate the model. It was observed that the pin size and tool offset were most influential to affect microhardness and tensile strength. The ductile mode of failure was confirmed by the fine dimples indicated in fractography [99].

2.3 RESEARCH GAP

Based on the literature survey research gaps were identified. The effect of Tool RPM, transverse speed, tilt angle and square pin side length, on mechanical properties of friction stir welded joint of dissimilar aluminum alloy AA 5083-O and AA 6082-T651 were still to be analyzed. The relationship between mechanical properties and mentioned factors was still to be established and optimization of the factors for maximizing the mechanical properties with multi-objective optimization was to be analyzed.

2.4 RESEARCH OBJECTIVES

The research objectives have been presented as:

- Selection of the base material and tool material.
- Selection of the FSW parameters based on research gap.
- Study the effect of FSW parameters on mechanical properties.
- Metallurgical tests for microstructure.

CHAPTER 3: EXPERIMENTAL SETUP

In the present chapter, the details of the machines used have been depicted.

3.1 FRICTION STIR WELDING MACHINE

FSW set up pictorial view has been presented in Figure 3.1. This machine is specially customized to perform Friction Stir Welding. The machine was procured from R V Machine Tools. The machine has an arrangement for varying the tool rotational velocity digitally. The traverse velocity may be changed as per the requirement with the help of a knob. The tool plunge speed may be modified

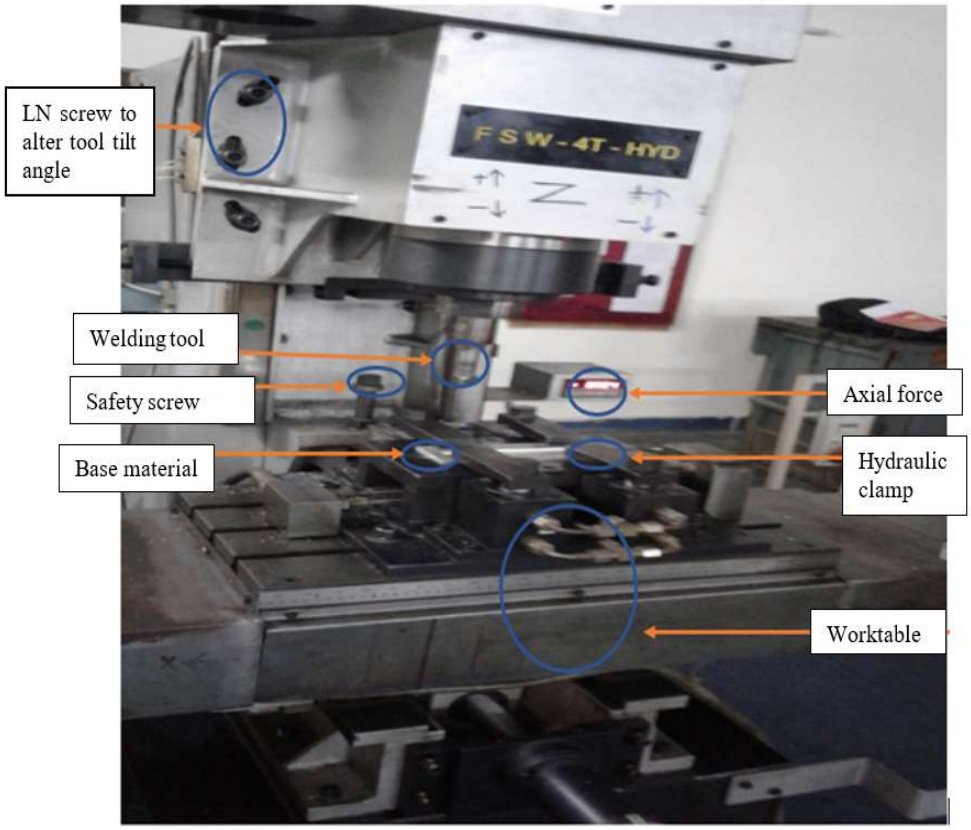

Figure 3.1: FSW machine setup

along the Z- Direction. The setup has a separate panel to operate the machine in a user-friendly manner. Provision to change tilt angle has also been provided. A display panel for showing the axial force is available in the setup. A hydraulic system has been used for holding and release of the plate.

3.2 TENSILE TESTING MACHINE

It was used for evaluating the tensile properties of the material under investigation. Before testing the specimen of the material should be prepared as per ASTM standards. The tensile specimen may be cylindrical or in form of a plate/sheet depending upon the shape of the material under investigation. Depending upon the type of ends of the tensile specimen proper grippers should be equipped in the machine before the test. Proper precautions should be followed because of the proper alignment of the two grippers/jaws of the machine. The tensile test is a destructive test in which the test material is broken into two pieces. The tensile test machine may be hydraulic or servo based. The strain rate should be carefully selected before the test.

The tensile testing machine was available at Delhi Technological University procured from Tinius Olsen. The specifications of this machine have been presented in Table 3.1. The machine set up has been presented in Figure 3.2.

Specification of tensile testing machine working range and accuracy details are presented:

- Accuracy of load measurement: +/-0.50% of specified load from 2.0 percent to 100.0 percent capacity.
- Accuracy of position measurement: +/-0.01 percent of reading or 0.001 mm whichever is greater.

- Accuracy of speed: +/-0.005 percent of prescribed speed
- Temperature range of operation: 0 to 38-degree centigrade
- Range of storage temperature: -10 to 45 degree centigrade
- Humidity variation :10.0 to 90.0 percent non-condensing; wet bulb method
- Standard optional voltages: 220/240 V AC, 50-60 Hz. Power must be free of spikes and surges exceeding 10 percent of nominal voltages.

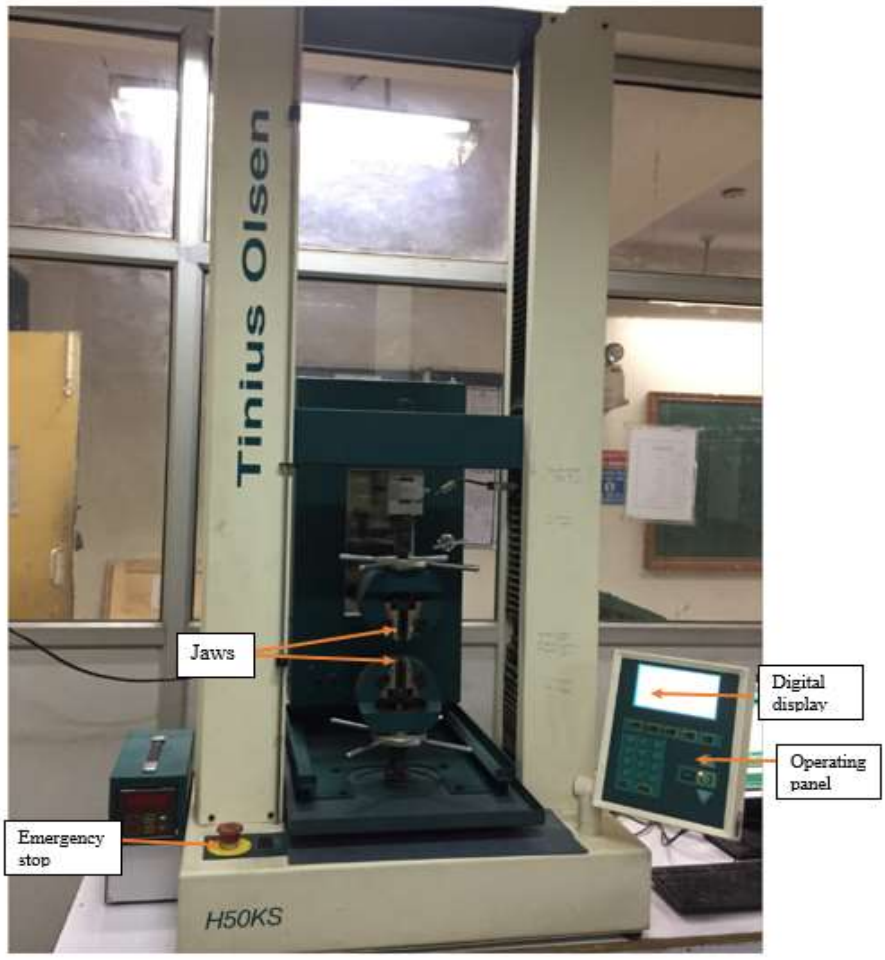

Figure 3.2: Tensile testing machine

Table 3.1: Specification of the tensile testing machine

Capacity	50 kN /5000 Kg
Clearance between columns	405 mm
Details of Load cells	Rapid change, low profile Z type load cells with digital encoding for automatic recognition.
Maximum travel of crosshead	1100 mm
Range of testing speed	0.001 to 500 mm/min
Capacity at maximum speed	25 kN
Maximum speed at capacity	250 mm/min
Jog speed	0.001 to 500 mm/min
Return speed	0.001 to 500 mm/min
Dimensions (H X W X D) of machine	1.613 m x 0.720 m x 0.50 m
Weight of machine	140 Kg

3.3 CHARPY IMPACT TESTING MACHINE

Charpy impact testing machine installed at the Delhi Institute of Tool Engineering was used to evaluate the impact strength presented in Figure 3.3. A Charpy impact testing machine is used to find the energy absorbed by a notched test specimen of

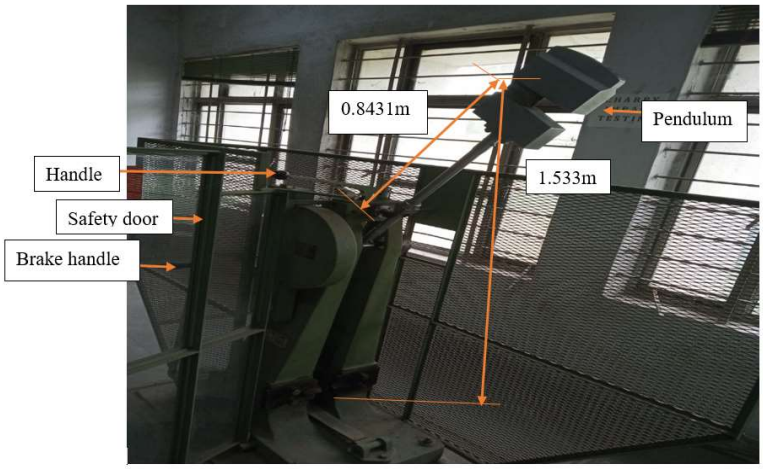

Figure 3.3: Charpy Impact testing machine

standard size during fracture. The machine works on the theory of conservation of energy. Charpy test machine has a pendulum of known length & a heavy hammer of known weight at its lower end. The hammer is raised to a known height at the beginning of the test. A standard notched specimen is placed at the lowest end of the pendulum path. The hammer is dropped and it breaks the specimen and further raises to the height on the other side. The energy absorbed during the fracture may be measured from the difference in heights on either side of the pendulum. The machine used in this study was installed at the Delhi Institute of Tool Engineering. The machine had a provision that its hammer could not be dropped from the raised position until the door remains open. Further, the machine was equipped with a hand-operated brake to stop the swinging hammer after one complete swing on both sides of the pendulum.

3.4 POLISHING STATION

The polishing station picture has been presented in Figure 3.4. The polishing

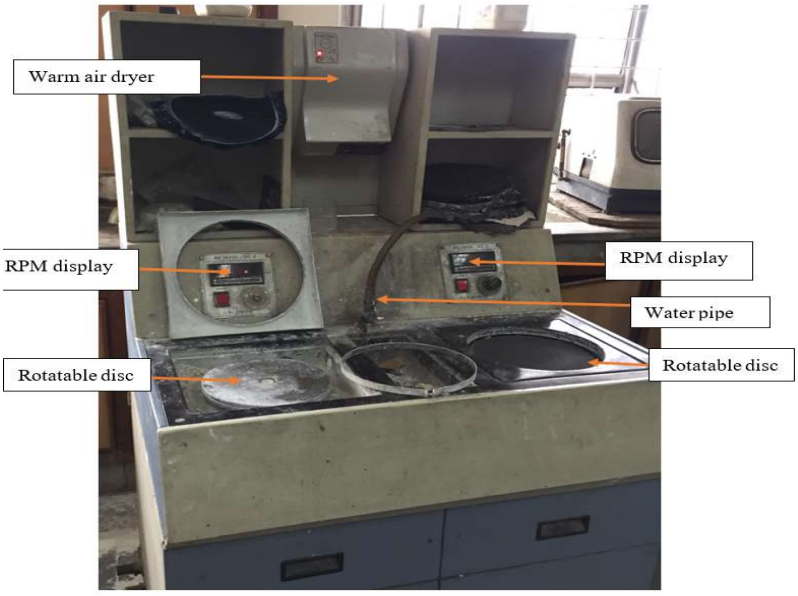

Figure 3.4:Polishing station

station was used to grind and polish the weld specimen mounted in resin mold and prepare it for the microstructural test. The polishing machine consisted of two rotatable discs capable of rotating at different speeds. The polishing machine was also equipped with two digital rotational speed indicators for the two discs. The emery paper was mounted on the disc with the help of an adjustable ring as shown in Figure 3.4. The discs were capable to rotate at a different speed. A water jet pipe was provided to wet the emery paper surface and specimen during the grinding. A warm air dryer was available for drying the specimen during the sample preparation. The polished specimens were etched and microstructure was evaluated using an optical microscope.

3.5 OPTICAL MICROSCOPE

The microstructure evaluation was performed with an Olympus GX41-optical microscope. The specifications of the microscope have been presented in Table 3.2.

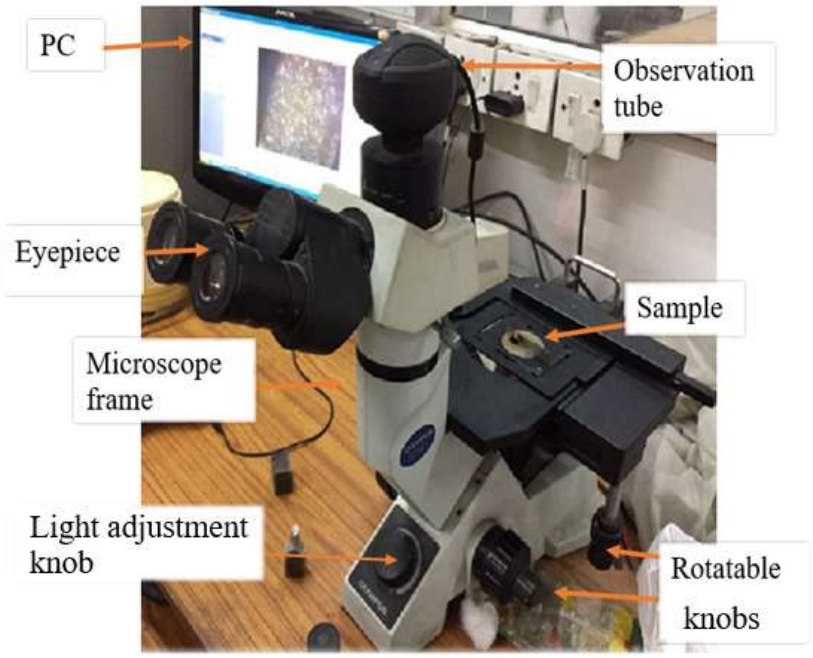

Figure 3.5: Optical microscope

Table 3.2: Specifications of the optical microscope

Optical System			UIS2 Optical System (Infinity-corrected)
Microscope Frame		Observation Method	BF/KPO
		Reflected/Transmitted	Reflected
		Illumination System	Reflected Light (30W Halogen or Fiber Light Guide (Light source:100W)
	Focus	Motorized /Manual	Manual Revolving Nosepiece Up/Down Movement (Stage Stationary Type)
		Stroke	9 mm
		Resolution/Fine Adjustment Sensitivity	Fine Stroke per Rotation 0.2 mm
	Revolving Nosepiece	Manual Type	Quadruple for BF
Stage		Stroke	120(X)x78(Y)mm
Observation Tube	Standard Field (Field Number 18)	Inverted Image	Tilting Binocular Observation Tube
	Standard Field (Field Number 20)	Inverted Image	Binocular/Trinocular/Tilting Binocular Observation Tube
	Wide Field (Field Number 22)	Inverted Image	Binocular/Trinocular/Tilting Binocular Observation Tube
	Dimensions		236(W)x624(D)x407(H)mm
	Weight		10 kg

The optical microscope used in the present study had a provision to place the specimen in the inverted position only. The microscope was equipped with a revolving objective turret, and three objective lenses with the magnification of 100 X, 200 X and 500 X. The objective lenses were mounted on the objected turret. The Objective turret may be rotated to align the lens below the specimen. Focus knobs could be used for coarse and fine adjustments separately. A light source was provided, and light intensity may be adjusted using a separate knob. The magnified image of the specimen could be viewed with an eyepiece. The microscope was

connected to a personal computer wherein the magnified images could be viewed and saved.

3.6 SCANNING ELECTRON MICROSCOPE

The scanning electron microscope picture has been presented in Figure 3.6. The detailed specification of the microscope has been presented in Table 3.3. This machine was used to extract SEM images to augment the analysis. The SEM images may be analysed and processed with the help of a personal computer/laptop. The scanning electron microscope manufactured by Hitachi TM3000 may be installed easily on the tabletop. It utilized an oil-free vacuum system and a turbo-molecular pump for major pumping. Rough pumping was handled by a diapharm based evacuation system. It may handle a sample of a maximum diameter of 70 mm and

Figure 3.6: Scanning electron microscope machine

thickness of 50 mm. A non-conducting material surface may be accumulated with a negative charge in high vacuum SEM preventing the common imaging process. Unlike conventional SEM, TM3000 may overcome this problem of low vacuum mode. Besides normal imaging TM3000 may augment the SEM analysis by presenting different compositions with different brightness levels.

Table 3.3: Specifications of the Scanning electron microscope

Item	Description
Magnification	15 to 30,000x (digital zoom: 2x, 4x)
Observation condition	5kV/15kV/Analysis
Observation mode	Standard mode/charge-up reduction mode
Sample stage traverse	X: ±17.5mm, Y: ±17.5mm
Maximum sample size	70mm in diameter, 50mm height
Signal detection system	High-sensitive semiconductor BSE detector
Auto image adjustment function	AutoStart, autofocus, auto-brightness/contrast
Evacuation system (vacuum pump)	Turbomolecular pump: 30L/s x 1 unit, Diaphragm pump: $1m^3/h$ x 1 unit
Operation help function	Image shift

3.7 RESIDUAL STRESS MEASUREMENT

The residual stress measuring machine is based on X-ray diffraction. The machine used in the present study μ-X360 was procured from Pulstec and was installed in the mechanical department of the Delhi Technological University. A personal computer may be connected to the stress measurement unit by a USB port. The machine has been presented in Figure 3.7.

Figure 3.7: X-ray residual stress analyser

The present machine setup was portable and easy to use and may be used for various applications where other bulky machine setups could not be used. The specifications of the residual stress measuring machine are as follows

- Collimator size : Diameter 1.0 mm
- X-ray Tube: Standard Computer radiography ・30kV・1mA
- Illuminated surface Approximate diameter 2 mm
- Sample position tolerance: ±5 mm
- Electric power - Only 75W during the measurement and 30W in standby mode
- Sensor Unit weight: Approx.5 kg
- Power supply unit: Approx. 6 kg

3.8 MICROHARDNESS MEASUREMENT MACHINE

The microhardness tests of the friction stir welded specimens were performed on Mitutoyo make microhardness measurement machine MVK H1. The machine picture has been presented in Figure 3.8. The machine's specifications are:

- Capacity of force: 0.01 to 1 Kgf.
- Sample size: 0.25 mm square or larger.
- The machine was equipped with a digital XY stage and offers a magnification of 100x and 400x.
- Measurement was performed with a digital ocular with precise measurement.
- The digital display shows the HV value and stage position.

Figure 3.8: Micro hardness measuring machine

3.9 X-RAY DIFFRACTOMETER

An X-ray diffractometer installed in the physics department of the Delhi Technological University was used for obtaining the XRD spectrum. BRUKER D8 ADVANCED XRD diffractometer (Figure 3.9) was operated with Cu-Kα X-ray radiation at a wavelength λ=1.54056 Angstrom at ambient temperature.

An XRD machine has the following components:

- X-ray source
- X-ray optics

Figure 3.9: XRD machine

- Detectors
- Sample stage

A sealed tube is used for an X-ray spot or line focus. A microfocus source boosts the intensity of small spots. X-rays generated by the source are shaped by optics into a useful X-ray beam, optimized for the size and shape of the sample and the application. High-tech X-ray detectors are used to detect the X-ray for various applications. Various types of sample stages may be used to place the sample into the XRD machine for different applications.

CHAPTER 4: METHODOLOGY

In the present chapter, the selection of base materials, tool material and their respective size have been presented. The experimental methodology and data collection details have been depicted.

4.1 SELECTION OF BASE MATERIAL

Two dissimilar grades of aluminum alloys were selected for this study. The 6.35 mm thick aluminium alloy 5083-O and 6082-T651 were selected. Base plate material selection was justified by their various applications in marine, and industries wherein corrosion-resistant lightweight material are required. The percentage composition and mechanical characteristics of both alloys are manifested in Table 4.1 and Table 4.2, respectively. AA 5083-O and AA 6082-T651 were machined and sized to 200 X 40 mm using a band saw and a shaper machine. Band saw machine was used for giving rough size and rectangular shape of length 200mm and width 40mm to the specimens. A shaper machine was used for giving exact rectangular shape and accurate dimensions to the specimens. Sixty-two specimens were prepared of the above size including thirty-one samples of both alloys each.

Table 4.1: Percentage composition of the base plate

Alloy/Percentage composition	Si	Fe	Cu	Mn	Mg	Cr	Zn	Ti	Al
6082-T651	1.0	0.25-.26	0.07-0.08	0.7	0.8	0.05	0.03	0.05	Remaining
5083-O	0.1	0.16	0.03	0.66	4.5	0.06	0.03	0.07	Remaining

Table 4.2: Base plate mechanical properties

Alloy/Mechanical properties	Ultimate tensile strength (MPa)	Yield Strength (MPa)	Percentage Elongation	Hardness (HB)
6082-T651	310-320	255	11-13	94
5083-O	270-350	200	25-27	74

4.2 FSW PARAMETERS IDENTIFICATION

The process parameters and factors that have an effect on the quality of the FSW joint have been presented in Table 4.3. Proper selection of the values of the variables for conducting welding has an ample impact on the mechanical features of the weld base material. In the present study, three process parameters and one tool-based parameter were selected. Tool's rotational velocity, linear velocity, tilt angle and square pin size were chosen for analysis.

Table 4.3: Parameters affecting the welded joint performance

Process parameters	Material-based parameters	Tool-based parameters	Clamp design
Tool Rotational speed	Melting point	Tool material	Clamp force
Traverse speed	Material properties	Pin geometry	Clamp Geometry
Tilt angle	Material thickness	Pin size	
Plunge force	Base material type (Similar / Dissimilar)	Shoulder features	
		Shoulder size	
		Thread pitch	

4.3 SELECTION OF OUTPUT PARAMETERS

Four mechanical properties selected as output parameters were (a) ultimate tensile strength (UTS), (b) Yield Strength (YS), (c) percentage elongation (EL), and (d) impact Strength (I). UTS of a metal is the highest tension it can withstand prior to fracture, under the tensile load. YS of a material is the stress at which plastic deformation begins. For materials that do not have a distinct yield point in the stress-

strain diagram, the strain value at 0.2 percent is treated as a yield point. Percentage elongation is the total change in length of a material under tensile test in percentage compared with the original length. The above values may be evaluated by the tensile test of the standard tensile specimen. The impact strength may be calculated using an impact testing machine.

4.4 TOOL SELECTION AND MANUFACTURING

The tool geometry is an essential parameter in FSW. A tool with a square pin has been selected for the welding (tool design and tool after welding have been manifested in Figure 4.1 and Figure 4.2 respectively). The tools of different sizes have been used for seeking their influence on the mechanical characteristics of FSW joints.

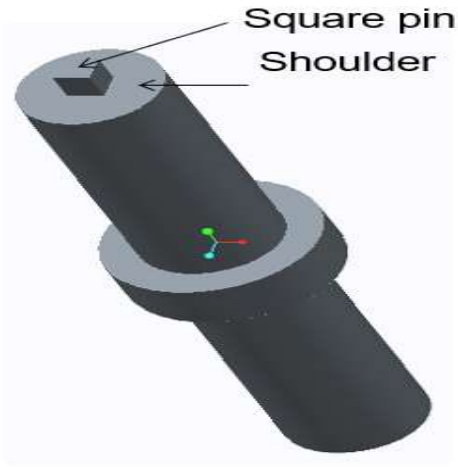

Figure 4.1:Design of FSW tool

Five tools with the square pins of the side 4.2, 4.6, 5.0, 5.4, and 5.8 mm with shoulder diameter 20 mm have been manufactured. The size of square pin side length is selected such that proportion of shoulder diameter to the diagonal of the square pin remains between 2.4 and 3.4 and accordingly square pin size has been

decided. A round bar of H-13 material with a diameter of 30 mm was procured and cut with the bandsaw machine to attain rods of length 125 mm each. Each bar was turned by the lathe machine to achieve a shoulder of twenty millimetres diameter with a cylindrical probe of height 6mm. The cylindrical pin was machined on a CNC vertical milling machine to attain an accurate square size. The tool was further

Figure 4.2: FSW tool after welding

hardened to a hardness value of 45 HRC.

4.5 SELECTION OF THE DESIGN OF EXPERIMENTS TECHNIQUE (DOE)

The DOE is a systematized methodology to conduct a set of tests to reach a predefined goal. During experimentation, input variables are varied in a manner that the cause of changes in output variables may be assessed and analyzed. There are various types of techniques that may be used for this purpose. Few methods are one factor at a time, full Factorial design, fractional factorial design, and response surface methodology.

4.5.1 ONE FACTOR AT A TIME

In this technique, a starting point and a bottom line for each input factor are decided. Each parameter is differed within its predetermined set while maintaining other parameters unchanged at its bottom line. Input factors are changed in the prescribed manner, the response is noted, graphs are drawn for each factor, and the effect on the response is analyzed. The interaction effects between the input factors could not be explained by this method.

4.5.2 FULL FACTORIAL DESIGN

The above drawback of the one factor at a time method may be eliminated by changing factors concurrently rather than varying a one parameter at a time. This method exhibits the main effects and interaction effect, as well. In this method, the total number of runs is represented by the formula (L^k), where L represents numbers of levels, and k represents the number of factors. For instance, if there are four factors, each having two levels, then the total number of tests shall be (2^4), i.e., 16. An increase in essential input parameters, raises the quantity of runs, which becomes non-feasible to perform due to significant time and resource consumption.

4.5.3 FRACTIONAL FACTORIAL DESIGN

In the fractional factorial design, for more than four, five, or more factors, it is possible to attain similar results as that of full factorial design by performing a lesser number of runs. Factorial design of fraction is a variant of full factorial design where in part tests are performed. For instance, in half fractional factorial, only half of the total runs are performed than that of full factorial with similar effectiveness.

4.5.4 RSM

It is a combination of statistical and mathematical methods used to accommodate an empirical model with statistical information obtained from the experiments. It is used to generate linear as well as quadratic model to explain a process. This method is further used to find the input variables value to optimize the goal or output variables. The response variable may be maximized, reduced, or set to a goal value depending on the requirement. CCD is a part of DOE that includes factorial runs, a group of axial or star point runs, and central runs. The factorial run may have a full or fractional factorial (4.6.2 and 4.6.3) run. The factorial runs lead to the assessment of interaction results; axial points lead to evaluation of quadratic terms in the model. Center point runs estimate the error and also evaluate quadratic terms. The different variants of CCD are as follows Rotatable-CCD, face-centered-CD. Rotatable CCD may further be of two types: circumscribed and inscribed. The former is a basic form of rotatable CCD, including a star point/axial point at a distance of α from the middle of the model. For rotatable CCD, α depends on the number of factors, and may be found by the formula: $[(2)^k]^{1/4}$, where k indicates the number of variables. Face centered composite design has 3 levels with alpha equal to one and minus one, and center point at zero.

4.5.5 DESIGN SELECTION

The aim the study is to analyze the influences of specific FSW variables on the mechanical characteristics of the weld by developing a suitable model for further prediction and optimization. Because of the goals of the present study, response surface methodology has been selected. In RSM, rotatable CCD has been opted to generate the matrix.

The design matrix has been presented in Table 4.4. In the design matrix, a total of thirty-one runs (sixteen factorial runs, eight star runs with alpha value two, and seven central runs with no blocking) have been included. The four parameters, each having five levels, have been manifested in Table 4.5.

Table 4.4: Design matrix for performing welding in coded form

Experiment	R	W	T	S
1	-1	-1	-1	-1
2	1	-1	-1	-1
3	-1	1	-1	-1
4	1	1	-1	-1
5	-1	-1	1	-1
6	1	-1	1	-1
7	-1	1	1	-1
8	1	1	1	-1
9	-1	-1	-1	1
10	1	-1	-1	1
11	-1	1	-1	1
12	1	1	-1	1
13	-1	1	1	1
14	1	-1	1	1
15	-1	1	1	1
16	1	1	1	1
17	-2	0	0	0
18	2	0	0	0
19	0	-2	0	0
20	0	2	0	0
21	0	0	-2	0
22	0	0	2	0
23	0	0	0	-2
24	0	0	0	2
25	0	0	0	0
26	0	0	0	0
27	0	0	0	0
28	0	0	0	0
29	0	0	0	0
30	0	0	0	0
31	0	0	0	0

Table 4.5: FSW variables and levels

Parameter	Units			Levels		
		(-2)	(-1)	(0)	(+1)	(+2)
Tool rotation velocity (R)	RPM	600	700	800	900	1000
Welding velocity (W)	mm/min	30	47.5	65	82.5	100
Tilt angle (T)	Degrees	0	0.50	1.00	1.50	2.00
Side of square pin(S)	mm	4.2	4.6	5	5.4	5.8

The actual factor level and coded value are related using the below formula

$$Xi = \frac{2X-(Xmax+Xmi\ )}{(Xmax-Xmin)/_2} \quad (3.1)$$

Xi indicates the coded value for the i[th] variable, X refers to the actual value of the variable for which coded value is required, and *Xmax* and *Xmin* are the maximum and minimum value of the variable under consideration. The equation is used to find out the values of intermediate levels.

In the present study, the design matrix has $2^{4=}16$ factorial runs, 2 X 4=8 axial runs with $\alpha = \sqrt{4}=2$, and 7 center point runs.

4.6 PERFORMING FSW

Aluminum plates were properly cleaned with a suitable chemical to eliminate oil and dust before FSW. The plates were positioned and hydraulically clamped in FSW machine fixture. The plates of AA 6082 T-651 being harder than AA 5083-O were placed on the AS during FSW. The tool was held in the tool holder and the LN screws were tightened on flats cut on it, with LN key. The suitable tool was mounted in the tool holder as per the design matrix. The proper tool tilt angle was set on the machine as per the design matrix. Tool rotation speed and welding speed were set as

per the design matrix. After commencing the tool rotation, it is brought down till the pin touches the plates. After the pin plunges into the base plates and the shoulder contacts the plates, the downward movement is continued till the axial force reaches 600 N on the display screen of the machine. The further downward movement of the rotating tool is stopped and is maintained in the same position to heat the plate material. After a few seconds, the table was moved in a direction to facilitate the relative linear movement between the rotating tool and plates. The simultaneous movement of the tool rotation and the linear speed resulted in the FSW joint.

The dissimilar plates were welded perpendicular to the rolling direction of the grains to achieve butt joints of size 200 X 80 mm. After the first run, the hydraulic clamps were released, welded plates were removed. Tool and other parameters were changed as per the design matrix to conduct the second run. FSW

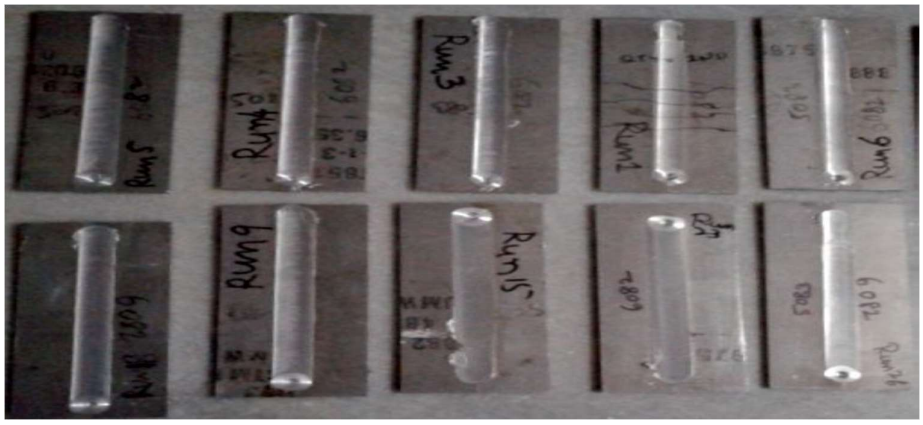

Figure 4.3: Pictures of a few welded plates

was performed in random sequence to ensure balance in the effects of uncontrollable factors. A total of thirty-one joints were made during the experimentation. A few welded plates have been presented in Figure 4.3.

4.7 MECHANICAL TESTS OF WELDED JOINTS

Tensile and impact test specimen preparation and conduct are presented.

4.7.1 TENSION TEST

The tension test results have been tabulated corresponding to the design matrix in Table 4.6. The tensile sub specimens of gauge length 25 mm (presented in Figure 4.4) were cut in the transverse direction from the welded joints using a wire EDM machine as per ASTM B557 specifications.

Table 4.6: Design matrix and response values

Standard	R	W	T	S	UTS	YS (MPa)	EL (%)	I (Joules)
1	700	47.5	0.5	4.6	176	130	14.2	35.1
2	900	47.5	0.5	4.6	175	118	18.8	34.0
3	700	82.5	0.5	4.6	176	134	13.5	32.0
4	900	82.5	0.5	4.6	176	110	15.1	34.0
5	700	47.5	1.5	4.6	175	124	12.5	36.0
6	900	47.5	1.5	4.6	158	101	17.9	38.0
7	700	82.5	1.5	4.6	192	136	14.4	29.2
8	900	82.5	1.5	4.6	179	110	16	36.0
9	700	47.5	0.5	5.4	168	120	15.2	28.5
10	900	47.5	0.5	5.4	168	108	17.3	27.0
11	700	82.5	0.5	5.4	150	115	9.8	24.0
12	900	82.5	0.5	5.4	155	99	10.1	18.6
13	700	47.5	1.5	5.4	173	120	13.4	36.0
14	900	47.5	1.5	5.4	165	103	18.3	40.0
15	700	82.5	1.5	5.4	191	138	14.8	30.0
16	900	82.5	1.5	5.4	180	114	17.1	31.0
17	600	65	1	5	187	142	13.2	31.0
18	1000	65	1	5	185	107	19.2	32.0
19	800	30	1	5	161	108	16.8	40.0
20	800	100	1	5	175	115	10.6	34.0
21	800	65	0	5	144	106	6.95	19.9
22	800	65	2	5	164	112	11.1	34.0
23	800	65	1	4.2	189	135	18.6	35.5
24	800	65	1	5.8	181	127	19.7	29.9
25	800	65	1	5	171	109	14.2	25.0
26	800	65	1	5	174	110	11.2	24.0
27	800	65	1	5	176	111	13.6	25.0
28	800	65	1	5	172	114	15.0	26.0
29	800	65	1	5	174	108	11.7	23.0
30	800	65	1	5	173	110	12.1	26.0
31	800	65	1	5	170	108	13.7	26.0

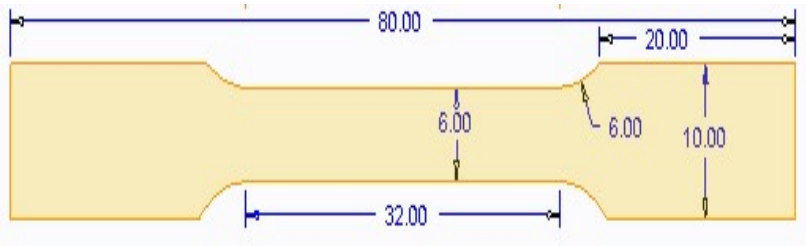

Figure 4.4: Tensile test specimen based on ASTM B 557

The specimens were sliced normal to welding direction. The tension tests have been performed at 2.5 mm/min strain rate, on the Tensile testing machine. The samples were marked with suitable identification symbols.

4.7.2 IMPACT TEST

Two techniques of measuring impact are available, Izod and Charpy impact test. Both methods are used to find the impact strength in various applications. The picture of a few impact specimens has been presented in Figure 4.5. These tests were


Figure 4.5: Charpy impact tests specimens

performed to assess the amount of energy absorbed to break the specimens using a swinging hammer falling from a particular height. The dimensions of the specimens in the Charpy impact test are different from that of the Izod impact test. Also, the positioning of the specimen of the Charpy and the Izod impact test is different. In this study, the Charpy impact test has been performed for all the welded specimens.

The impact test specimens were prepared for the Charpy test. The samples were machined from the middle of the FSW joint as ASTM Standards A-370. The specimens were machined accurately using the EDM wire cut machine. The specimens of size 55 X 10 mm and thickness 6.35 mm were prepared. A notch with a depth of two millimetres, an included angle of forty-five degrees, and a root tip radius of 0.25 mm were incorporated in the impact specimens. The Charpy impact testing machine used has been shown in Figure 4.6.

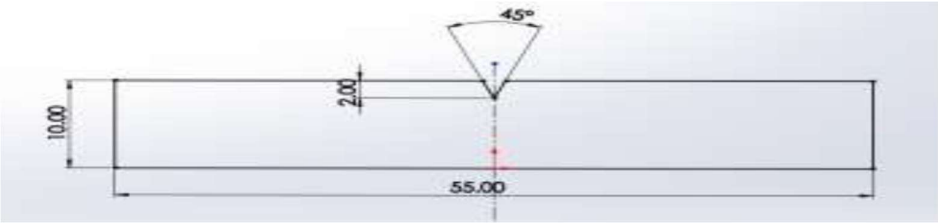

Figure 4.6: Design of Charpy impact test specimen

4.8 METALLURGICAL EXAMINATION

The samples of size 28 X 5 X 6.35 mm were sliced from the middle weld zone in a direction normal to the FSW for microstructural inspection. The grinder was used to ground the samples for smoothing the corners and level the uneven surfaces. The cut samples were installed in the resin mold. The specimens installed in mold, were ground using sandpaper with an increasing grit size (rough to fine) on a round-shaped rotating machine sequentially. Rough and fine polishing was performed using Aluminum oxide on the velvet paper. Etching with the Keller agent was performed before the final inspection on the optical microscope.

Etching (by Keller's agent) including distilled water-190ml, nitric acid-5ml, hydrochloric acid-3ml, hydrofluoric acid-2 ml was performed. The magnification of 100 X, 200 X and 500 X were available and samples were examined at different magnifications.

4.9 MICROHARDNESS MEASUREMENT

A Microhardness test is used to assess the hardness of material at the microscopic level. The Vickers microhardness test was used to measure the microhardness of the welded sample. In this test, the microhardness is measured at a load of up to 1.0 kg. The indenter is made to indent on the workpiece for a few seconds and the hardness is evaluated by using a formula based on size of indentation. Samples from the mid transverse section were cut, samples were mounted on mold, ground and polished before the microhardness test. In this study hardness values were measured along the transverse section at the mid-point of the thickness of the specimens. The hardness values were measured at a distance of two millimetres from the joint line on the AS and RS as presented schematically in Figure 4.7. Microhardness values were measured at 0.2 Kg load and 15 seconds of indentation time.

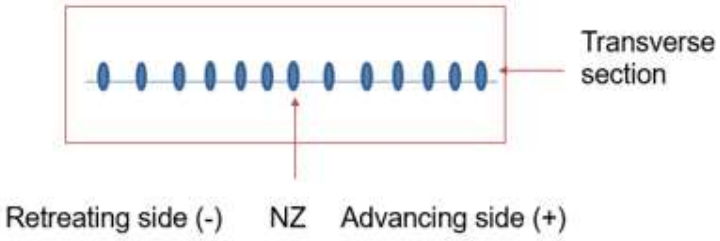

Figure 4.7: Microhardness measurement on the welded zone

4.10 XRD-ANALYSIS

It is a method used to recognize the phases, orientation and crystallinity in a material, and chemical composition related investigation. XRD analysis is based on the Braggs law. In the present study, the samples of size 5 X 5 X 6.35 mm were machined from the NZ of the welded samples using an EDM wire cut machine. The

samples were marked and were used to generate the data. The XRD analysis was performed on the machine available at Delhi Technological University as presented in the previous chapter. Angle 2 (theta) was varied from 10-70 degrees and data files were generated. Data files include 2 (theta) valued at an interval of 0.04 from 10-70 degrees and corresponding intensity values were recorded. Approximately 1500 readings were taken per sample. From the readings/data, graphs were generated using 'Origin' software and data was matched to the JCPDS standard database to find the phases and miller indices values. For matching with diffraction standards of JCPDS, "X'pert High Score Plus" software was used.

4.11 RESIDUAL STRESSES MEASUREMENT

Residual stresses are induced in a material due to 1) thermal changes, 2) Mechanical processing and 3) phase transformations. In FSW, the above-mentioned variations take place and maybe measured due to various causes in critical applications.

Presently, numerous non-destructive testing techniques are available to measure residual stresses. X-Ray residual stress measurement techniques are being used by various industries. $Sin^2\psi$ method and Cos α method are based on X-ray diffraction. Cos α method is increasingly being used due to the portability of measuring instruments. For measurement of the residual stress, Cos (α) method has been used, where alpha (α) indicates the azimuthal angle. The setup consists of an X-ray tube of 30kV and 1mA and a collimator size of diameter 1mm. Aluminum alloy has differently oriented crystal grains, which, when illuminated with an X-ray spot having a size larger than that of grains, it is diffracted at different orientations.

The orientations of different grains that satisfy Bragg's law only diffract the X-Ray. Bragg's law is represented by the following relation as given below:

$n \lambda = 2d\sin \theta$

n=An integer

λ=Wavelength of the incident X-rays,

d = Interplanar spacing of the joint crystal

θ = Diffraction angle.

As the compressive stress is induced in an alloy, the interplanar spacing is reduced and consequences in an increase in diffraction angle, theta. On the contrary, as the tensile stress is induced in the material, the interplanar spacing increases and results in a reduction of diffraction angle, theta. In the cos α method, the following procedure was followed to calculate the residual stress: X-ray is illuminated on the welded aluminum alloy grains, and the diffracted X-rays were received by a receptor in the form of a ring known as a Debye-Scherrer ring. A cone of diffracted rays is formed around the incident ray due to variation in the grain's orientation. The accurate position of the full Debye ring may be utilized to give the measure of strain produced by using mathematical equations. As the strain is calculated, the stress value was calculated by finding the slope of the graph between the calculated strain and cos α where alpha denotes the azimuthal angle of the Debye-Scherrer ring. The residual stress was calculated using the machine setup (presented in Figure 4.8) available at Delhi Technological University. The residual stress was calculated at the nugget zone, AS and RS.

CHAPTER 5: RESULTS AND DISCUSSION

In present chapter effect of process parameters on various responses using RSM has been discussed. Responses were maximized by optimizing the process parameters. Micro hardness plot analysis has been depicted. Residual stress and its influence on mechanical characteristics of the FSW joint has been elaborated. X-ray Diffraction analysis for the weld material has been described. In the last section of the chapter, the microstructure study using optical microscopy and SEM has been performed.

5.1 DEVELOPMENT OF EMPIRICAL RELATIONSHIP

The desired responses, ultimate tensile strength (UTS), yield strength (YS), percentage elongation (EL) and impact strength (I), and process parameters i.e. R, W, T & S may be functionally mapped as in equations (5.1-5.4):

$$UTS = f(R, W, T, S) \tag{5.1}$$

$$YS = f(R, W, T, S) \tag{5.2}$$

$$EL = f(R, W, T, S) \tag{5.3}$$

$$I = f(R, W, T, S) \tag{5.4}$$

The generalized second-order equation representing the response surface Y is given by equation (5.5).

$$Y = b_0 + \sum b_i x_i + \sum b_{ii} x^2_i + \sum b_{ij} x_i x_j + e_r \tag{5.5}$$

The term e_r, the residual error, is a measure of summation of pure error and lack of fit error. For the present investigation, UTS or YS or EL and I, a general regression equation has been given in equation (5.6)

UTS or YS or EL or I= b_0+ b_1 R + b_2 W + b_3T + b_4S + $b_{11}R^2$ + $b_{22}W^2$ + $b_{33}T^2$+ $b_{44}S^2$ + b_{12}RW + b_{13} RT + b_{14} RS + b_{23}WT + b_{24}WS + b_{34}TS (5.6)

In equation 5.6, b_0 indicates the intercept of the regression line. The coefficient terms b_1, b_2, b_3, and b_4 are the linear terms while quadratic terms are represented by coefficients b_{11}, b_{22}, b_{33} and b_{44}. Interaction terms are indicated by coefficients b_{12}, b_{13}, b_{14}, b_{23}, b_{24} and b_{34}.

The empirical models have been developed with a 95% confidence level of significant coefficients. The final reduced models were developed to predict the UTS, YS, EL and 'I' in the actual form with the help of statistics-based software Design Expert 12.0. The models of various responses have been presented in form of equations 5.7 to 5.10 in actual form.

UTS = 929.726 - 0.603R + 1.476 W - 50.532 T - 208.285 S + 0.0002 RW - 0.066 RT + 0.026 RS + 0.721 WT - 0.330 WS + 20.937 TS + 0.0003 R^2 -0.004 W^2 - 19.482 T^2 + 17.996 S^2 (5.7)

YS = 1341 - 0.665 R + 0.403 W - 83.9 T-354.7 S - 0.000929 RW - 0.0325 RT + 0.0250 RS + 0.485WT - 0.017 WS + 16.88 TS + 0.0003 R^2 + 0.0004 W^2 - 2.00 T^2 +31.25 S^2 (5.8)

EL= 272.207 - 0.073 R + 0.396 W - 23.058 T - 93.670 S - 0.0004 RW + 0.006 RT - 0.005 RS + 0.121 WT - 0.072 WS + 3.766 TS + 0.00008 R^2 + 0.0007 W^2 - 3.787 T^2 + 9.863 S^2 (5.9)

I= 444.236 - 0.187 R - 0.634 W - 68.039 T - 110.918 S + 0.00003 RW + 0.024 RT - 0.018 RS-0.055 WT - 0.143 WS + 10.85 TS + 0.0001 R^2 + 0.009 W^2 + 1.801 T^2 + 11.862 S^2 (5.10)

The equations in form of real variables may be used to forecast responses for given levels. The levels must be stated in the original units for each variable. To calculate the relative effect of each factor, these equations cannot be used since the intercept is not at the core of the design space and the coefficients are scaled to the units of each factor. The calculations in coded form, however, can be used to find the relative influence of different variables.

5.2 INFLUENCE OF INPUT PARAMETERS ON ULTIMATE TENSILE STRENGTH (UTS)

The detailed analysis and interpretation of RSM based graphs of UTS have been explained in the present section.

5.2.1 INSPECTION OF THE COMPETENCE OF THE MODEL-ANOVA FOR UTS

ANOVA indicates the quantification of change in response due to the change in levels of input variables. ANOVA is built on the concept of comparing the cause of variation in response variables. The variation in response variables may be based upon the following: (a) the variation due to change in levels of input variables, and, (b) error caused during the measurement of output responses. By comparing the sum of squares due to (a) and (b), the significance of the developed model and lack of fit may be assessed.

The total sum of squares may be bifurcated into the sum of squares due to the regression model and sum of square due to residual as given:

$$SS_T = SS_{reg} + SS_{res} \quad (5.11)$$

SS_T = Total sum of squares

SS_{reg} = Sum of squares due to the regression

SS_{res} = Sum of squares due to residual

The sum of squares due to residual (SS_{res}) may further be disintegrated into two parts:

$$SS_{res} = SS_{pe} + SS_{lofit} \quad (5.12)$$

SS_{pe} = Sum of squares due to pure error

SS_{lofit} = Sum of squares due to lack of fit of the model

The mean sum of squares may be evaluated by dividing the sum of squares by respective degrees of freedom. The adequacy of the regression equation may be assessed by the ratio of the mean sum of squares of regression (MS_{reg}) to the mean sum of squares of residuals (MS_{res}). This ratio is compared to the F- value for the given degrees of freedom associated with MS_{reg} and MS_{res}.

The developed model is significant as its F- Value is more than the tabulated value at a 95% confidence level. The lack of fit for the developed model is found to be non-significant as F-value for lack of fit is less than that of the tabulated value. A non-significant lack of fit is desirable for a model. Table 5.1 indicates the ANOVA table for response UTS. The fit summary has been presented in Table 5.2.

The significance of various terms may be assessed based on P-value. The terms with a P-value of more than 0.1 indicate the non-significant terms. In the model for the UTS the significant terms are as follows:

- Significant main effect terms: R, W, T and S.
- Significant interaction terms: RT, WT, WS and TS.
- Significant quadratic terms: R^2, W^2, T^2 and S^2.

The following terms are non-significant in the estimation of UTS:

- Non-significant interaction terms: RW and RS

The F-value of lack of fit is 2.66 and the corresponding P-value of 0.1216 signifies that there is only a 12.16 percent probability that lack of fit of F-value 2.66 may happen due to noise. R-squared value for the empirical model specified by Equation 5.7 is 0.9640 indicating that the remaining 3.6% variation in the prediction of UTS value could not be explained by variation in independent variables.

Table 5.1: ANOVA table of UTS

UTS						
"Source"	"Sum of Squares"	"Dof"	"Mean Square"	"F-value"	"p-value"	
"Model"	3613.67	14	258.12	30.57	< 0.0001	Significant
A-R	100.04	1	100.04	11.85	0.0033	
B-W	198.37	1	198.37	23.49	0.0002	
C-T	495.04	1	495.04	58.63	< 0.0001	
D-S	222.04	1	222.04	26.30	0.0001	
RW	3.06	1	3.06	0.3627	0.5555	
RT	175.56	1	175.56	20.79	0.0003	
RS	18.06	1	18.06	2.14	0.1630	
WT	637.56	1	637.56	75.50	< 0.0001	
WS	85.56	1	85.56	10.13	0.0058	
TS	280.56	1	280.56	33.23	< 0.0001	
R^2	280.05	1	280.05	33.17	< 0.0001	
W^2	53.71	1	53.71	6.36	0.0226	
T^2	678.35	1	678.35	80.33	< 0.0001	
S^2	237.10	1	237.10	28.08	< 0.0001	
Residual	135.11	16	8.44			
Lack of Fit	110.25	10	11.02	2.66	0.1216	Not significant
Pure Error	24.86	6	4.14			
Cor Total	3748.77	30				

Table 5.2: Fit summary for response UTS

"R-squared"	0.9640
"Adjusted R- squared"	0.9324
"Predicted R-squared"	0.8216
"Adequate Precision"	24.3442

The adjusted R-squared value for equation 5.7 is 0.9324 and is obtained by making adjustments in the R-squared value to accommodate the increase in the latter due to less valuable multiple independent variables. The predicted R-squared value for UTS is 0.8216 and its difference from the adjusted R-squared value is less than 0.2. Adequate precision representing signal-to-noise ratio for UTS is 24.34 which is more than 4.0 indicating that the empirical model is appropriate to navigate the design space.

5.2.2 ANALYSIS OF RESPONSE SURFACES AND CONTOUR PLOTS FOR UTS

Response surfaces and contour plots serve the following purposes: 1) to signify the interaction/independence of the factors, 2) to manifest the stationary points, and 3) to indicate an optimum value of desired response with sufficient accuracy.

Response surfaces and contour plots for UTS have been presented in Figures 5.1 to 5.8. The response surfaces and contour plots signify the plots of independent factors R & T, W & T, W& S, and T & S with UTS as response and the other two independent factors kept at the center points in each graph respectively. Red dots in the mentioned response surfaces and contour plots indicate the design points. Response surfaces and contour plots in Figures 5.1 and 5.2 show local maxima at the center point, however, the maximum value of the response is shown by red color in both the diagrams. The maximum response value was observed at a tilt angle of two degrees and tool rpm at 600 RPM. The elliptical nature of the contour plot indicates the interaction effect presence. Figures 5.3 and 5.4 present the response surface and contour plot of welding speed (W) and tilt angle (T) while fixing the remaining factors at their respective center point levels

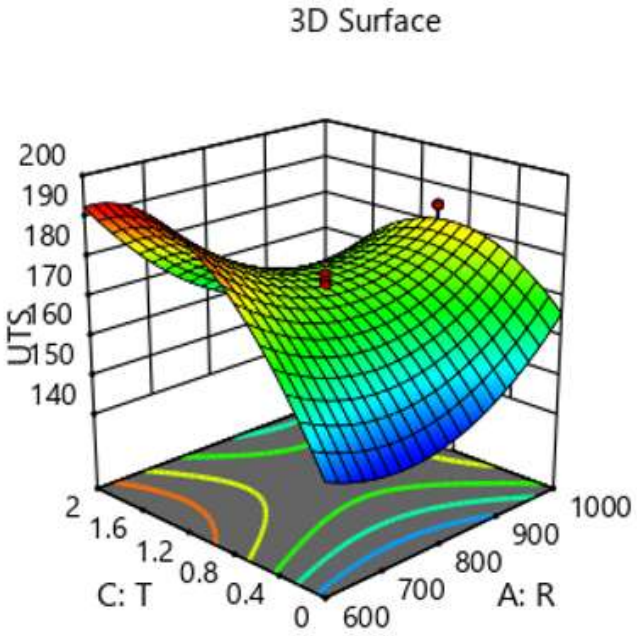

Figure 5.1: 3-D response surface of UTS for rotational speed and tilt angle

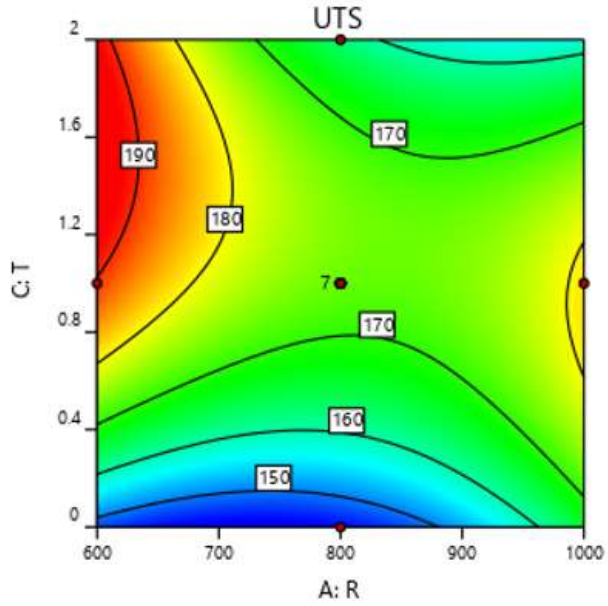

Figure 5.2: 2-D contour plot of UTS for rotational speed and tilt angle

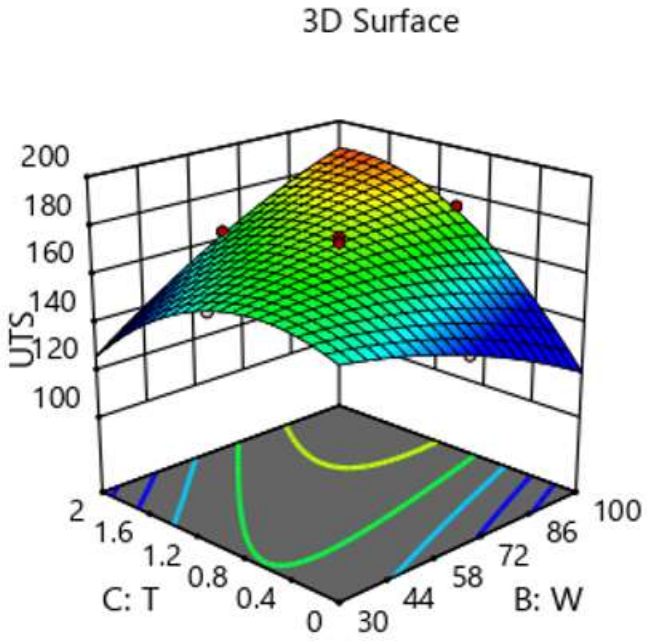

Figure 5.3: 3-D response surface of UTS for welding speed and tilt angle

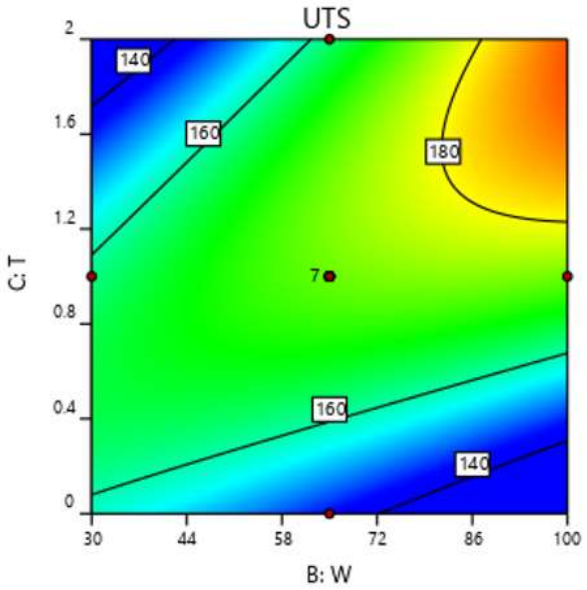

Figure 5.4: 2-D contour plot of UTS for welding speed and tilt angle

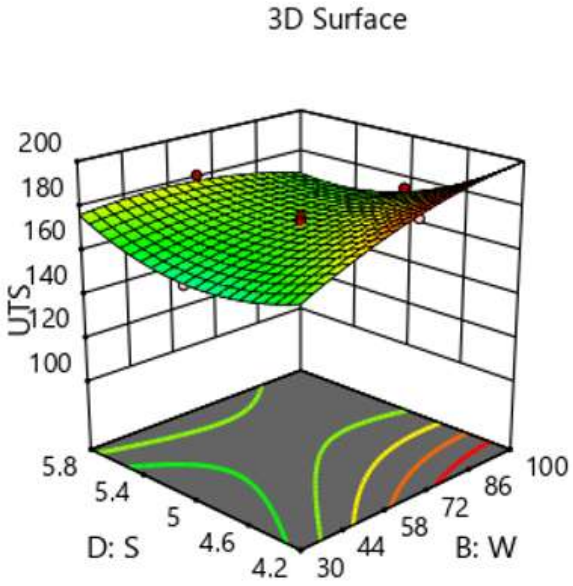

Figure 5.5: 3-D response surface of UTS for transverse speed and tool pin size

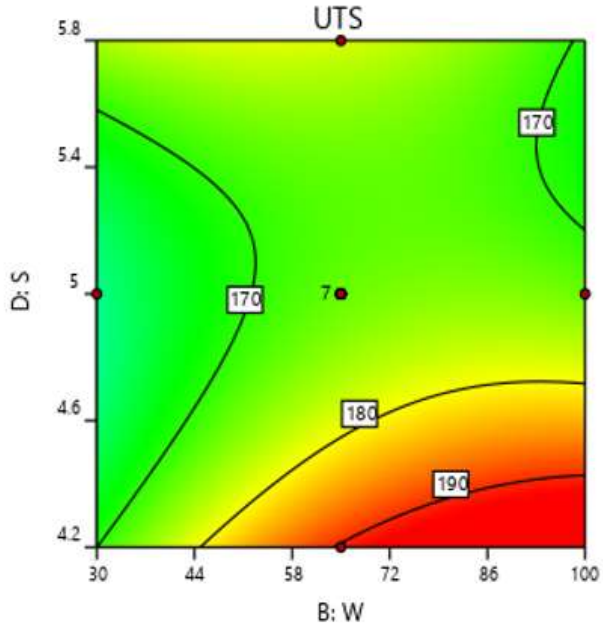

Figure 5.6: 2-D contour plot of UTS for traverse speed and pin size

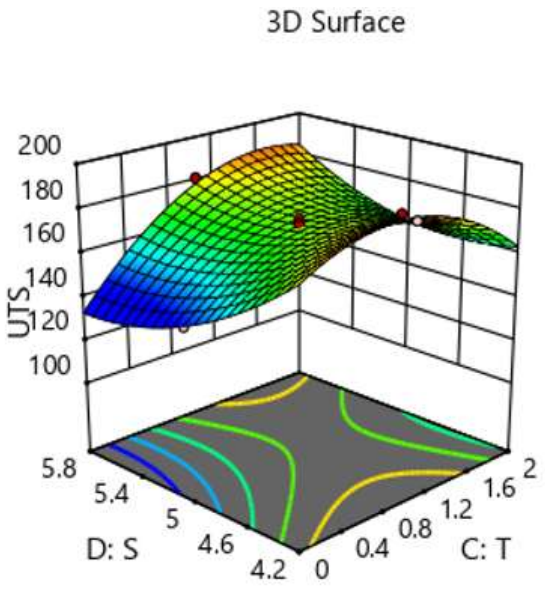

Figure 5.7: 3-D response surface of UTS for tilt angle and pin size

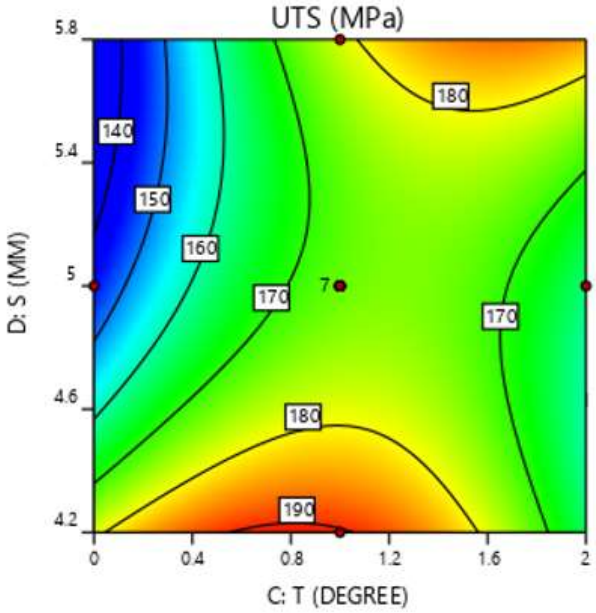

Figure 5.8: 2-D contour plot of UTS for tilt angle and pin size

The response surface indicates the maximum value of UTS at 100 mm/min welding speed and two degrees of tilt angle. As the contour plot of W and T is not circular, two-way interaction between the two parameters may be concluded.

Response surface and contour plot of W and S for response UTS, while fixing the remaining factors at their respective center point values, have been presented in Figure 5.5 and 5.6. The response surface indicates the maximum value of UTS at 100 mm/min welding speed and 4.2 mm square pin size. The contour plot of W and S is not circular and two-way interaction between the two parameters may be concluded.

Figures 5.7 and 5.8 present the response surfaces and contour plots of tilt angle (T) and pin size (S) while fixing the remaining factors at their respective center point values. The response surface and contour plot indicate the maximum value of UTS at the contour between 0.5-1.0 degrees of tilt angle and 4.2 mm pin size. The contour plot of T and S is not circular and two-way interaction between the two parameters may be concluded.

5.2.3 MAIN EFFECTS FOR RESPONSE UTS

The main effect of independent factors on UTS has been presented in Figure 5.9. The UTS increases with an increase in rotational speed (R) within the specified range. A slight curvature was observed in the main effect curve. The UTS value decreases with an increase in the welding speed (W). A slight curvature has also been observed in the main effect curve of welding speed and UTS. The UTS value decreases with an increase in the tool tilt angle and slight curvature has also been observed in this plot. In the main effect curve of UTS and pin size, an appreciable

curvature has been observed. In this plot, the UTS value first increases with an increase in pin size up to 5 mm pin size and then the UTS value reduces.

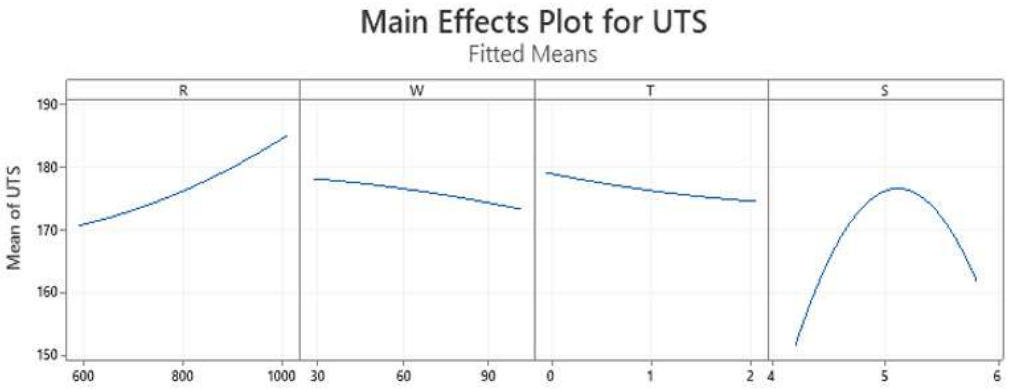

Figure 5.9: Main effects plot of input factors for UTS

5.2.4 INTERACTION EFFECTS FOR RESPONSE UTS

The interaction between two independent factors occurs when the effect of one factor is affected by the variation in the levels of the other. The interaction effects of various factors on UTS have been presented in Figure 5.10 (a), (b) and (c). The value of R ranges from 600 to 1000 rpm while W has been taken at three levels i.e., 47.5, 65 and 82.5 mm/min.

Figure 5.10 (a) indicates that the change in levels of welding speed (W) (shown in different colors) results in a change in the effects of rotational speed. The curves of R intersect one another at different levels of W indicating the presence of a two-way interaction effect between R and W.

The intersecting curves of R at different levels of tilt angle (T) indicate the existence of an interaction between R and T. The levels of T have been varied at three different levels 0.5, 1.0 and 1.5 degrees whereas R has been varied

continuously from 600 to 1000 rpm. It has been observed that as the level of T is changed from 0.5 to 1.5 the maximum value of UTS may be achieved at 1000 rpm.

The interaction effect of R and S on UTS has been observed as non significant. The values of R have been varied continuously from 600 to 1000 rpm whereas levels of S have been varied at three different levels 4.6, 5.0 and 5.4 mm. As the levels of square pin side length are varied, the curve of R and UTS remain parallel indicating the non significant two-way interaction.

The intersecting curves of welding speed (W) in Figure (b) at different levels of tilt angle (T) indicate the existence of an interaction between W and T. The levels of T have been varied at three different levels 0.5, 1.0 and 1.5 degrees whereas W has been varied continuously from 30 to 100 mm/ min. It has been observed that at T-level 0.5 and 1.5 degrees, the maximum value of UTS may be achieved at 100 mm/min and 30 mm/min respectively.

The interaction effect of W and S, on UTS, has been observed slightly significant. The value of W has been varied continuously from 30 to 100 mm/min whereas levels of S have been varied at three different levels 4.6, 5.0 and 5.4 mm. It was investigated that at S level 5.0, and 5.4 mm the W-UTS curve intersects at 90 mm/min and also at S level 4.6 and 5.4 mm the W-UTS curve intersect at 30 mm/min. The intersection of curves indicates the presence of two-way interaction.

The interaction effect of T and S on UTS has been observed as non significant as shown in Figure 5.10 (c). The value of T has been varied continuously from zero to two degrees whereas levels of S have been varied at three different levels 4.6, 5.0 and 5.4 mm. As the levels of square pin side length are varied, the

curves of T and UTS remain parallel indicating the nonexistence of two-way interaction.

A plot of normal probability (%) against externally studentized residuals of UTS has been presented in Figure 5.11. The plot is a check to ensure that the residual follows the normal distribution for response UTS. The presence of any pattern in the plot like an S-shape indicates the need for transformation of response for better analysis. Figure 5.12 presents the plot of residuals versus increasing predicted response values and should be randomly scattered and should not follow any pattern. This plot ensures the assumption of constant variance for the predicted values of UTS.

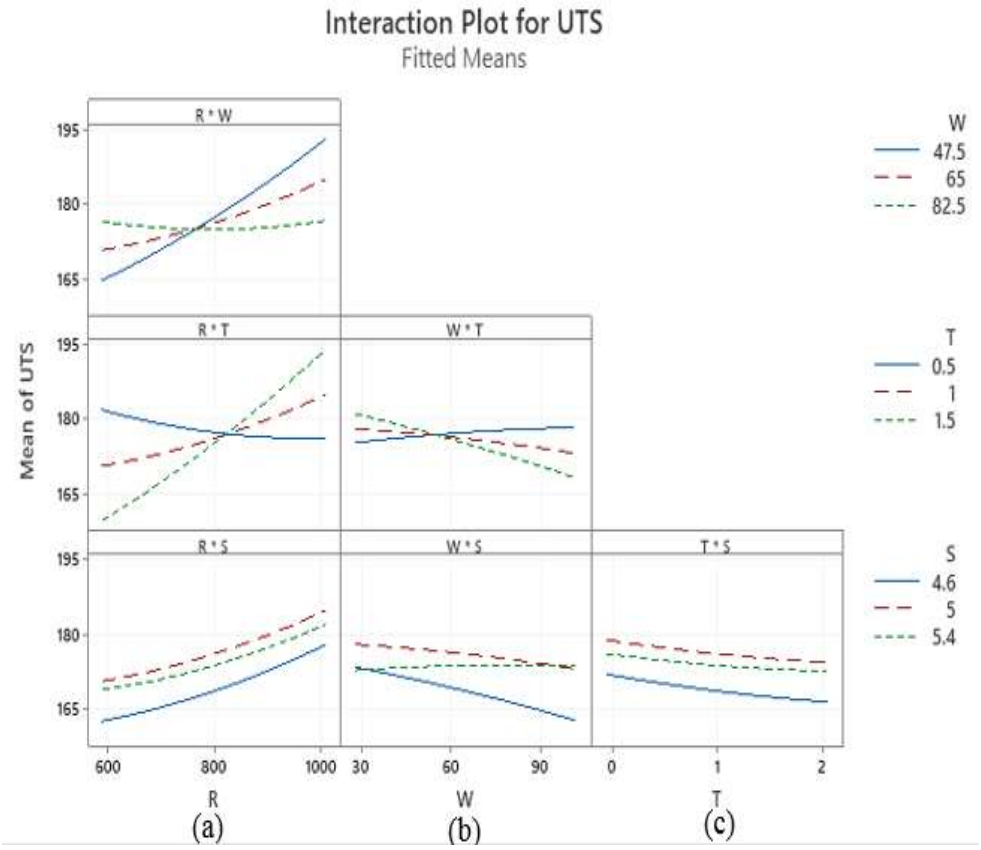

Figure 5.10: Interaction effects for different combination for UTS

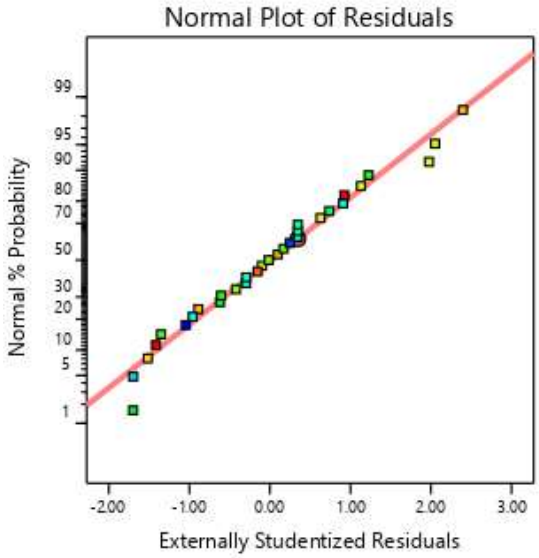

Figure 5.11: Plot of normal probability (%) against externally studentized residuals for UTS

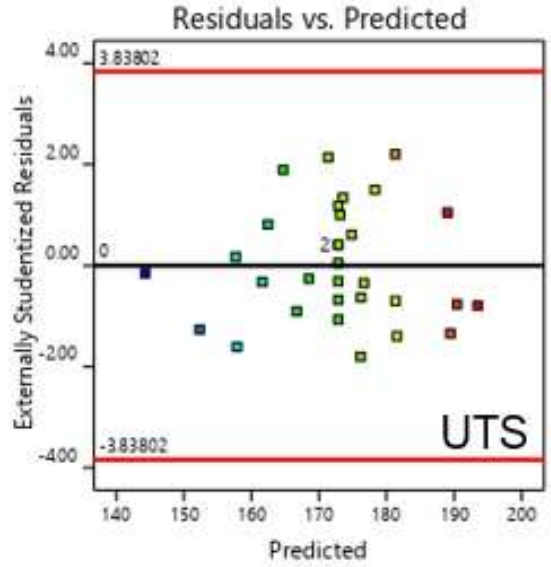

Figure 5.12: Plot of predicted values against externally studentized residuals for UTS

5.3 INFLUENCE OF INPUT PARAMETERS ON YIELD STRENGTH (YS)

The detailed analysis and interpretation of RSM based graphs of YS have been explained in the present section.

5.3.1 INSPECTION OF THE COMPETENCE OF THE MODEL - ANOVA FOR YS

Table 5.3 indicates the ANOVA table for the YS. The fit summary for YS has been presented in Table 5.4.

Table 5.3: ANOVA table of YS

YS						
"Source"	"Sum of Squares"	"Dof"	"Mean Square"	"F-value"	"p-value"	
"Model"	3942.84	14	281.63	54.95	< 0.0001	significant
A-R	2090.67	1	2090.67	407.93	< 0.0001	
B-W	88.17	1	88.17	17.20	0.0008	
C-T	24.00	1	24.00	4.68	0.0459	
D-S	160.17	1	160.17	31.25	< 0.0001	
RW	42.25	1	42.25	8.24	0.0111	
RT	42.25	1	42.25	8.24	0.0111	
RS	16.00	1	16.00	3.12	0.0963	
WT	289.00	1	289.00	56.39	< 0.0001	
WS	0.2500	1	0.2500	0.0488	0.8280	
TS	182.25	1	182.25	35.56	< 0.0001	
R^2	325.72	1	325.72	63.56	< 0.0001	
W^2	0.4468	1	0.4468	0.0872	0.7716	
T^2	7.15	1	7.15	1.39	0.2548	
S^2	714.89	1	714.89	139.49	< 0.0001	
Residual	82.00	16	5.12			
Lack of Fit	56.00	10	5.60	1.29	0.3919	not significant
Pure Error	26.00	6	4.33			
Cor Total	4024.84	30				

Table 5.4: Fit summary for response YS

"R-squared"	0.9796
"Adjusted R-squared"	0.9618
"Predicted R-squared"	0.9111
"Adequate Precision"	26.6180

The terms with a P-value of more than 0.1 indicate the non-significant terms. In the model generated for the YS the significant terms are as follows:

- Significant Main effects: R, W, T, S
- Significant Interaction terms: RW, RT, RS WT, TS,
- Significant Quadratic terms: R^2, S^2

The following terms in the estimation of YS are non-significant:

- Non-significant Interaction terms: WS
- Non-significant Quadratic terms W^2, T^2

The F value of lack of fit is 1.29 and the corresponding P-value 0.3919 signify that there exists only a 39.19 percent probability that lack of fit of F value 1.29 may happen due to noise. R-squared value for the empirical model specified by Equation 5.8 is 0.9796 indicating that the remaining 2.4% of the variation in the predicted YS value could not be explained by variation in independent variables. The adjusted R-square value for equation 5.8 is 0.9618 and is obtained by making adjustments in the R-squared value to accommodate the increase in the latter due to less valuable multiple independent variables. The predicted R-squared value for YS is 0.9111 and its difference from the adjusted R- square value is less than 0.2. Adequate precision representing signal-to-noise ratio for YS is 26.6180 which is more than 4.0 indicating that the empirical model is appropriate to navigate the design space.

5.3.2 ANALYSIS OF RESPONSE SURFACES AND CONTOUR PLOTS FOR YS

Response surface and contour plots for YS have been presented in Figure 5.13 to 5.22. The response surfaces and contour plots signify the plots of independent factors R & W, R & T, R & S, W & T, and T & S with YS as response and the other two independent factors kept at the center points in each graph, respectively. Red dots in the graph indicate the design points.

Figures 5.13 and 5.14 present the response and contour plot of tool rpm (R) and welding speed (W) while fixing the remaining factors at their respective center point values. The response surface indicates the maximum value of YS at 600 rpm tool rpm and 100 mm/min welding speed. The contour plot of W and T is not circular and two-way interaction between the two parameters may be concluded.

The response surface and contour plot in Figures 5.15 and 5.16 shows the variation of YS when tool rpm and the tilt angle are varied while keeping the other two input parameters at a constant value (center points). The red color curve indicates the maximum valued common response curve. The response is maximum near 600 rpm and a two-degree tilt angle. Curvature in the response surface has been observed along an axis parallel to that of tool rpm. Since circular contour is not present the existence of the interaction effect may be concluded. Figure 5.21 and 5.22 present response surface and contour plot of tilt angle and the pin size while keeping rotation rpm and traverse speed at constant levels (center points). As the contour plot is elliptical, the presence of the interaction effect may be concluded. The maximum value of the response YS up to 140 Mpa could be observed in the contour plot at tilt angle and pin size of 0.5 degrees and 4.2 mm respectively.

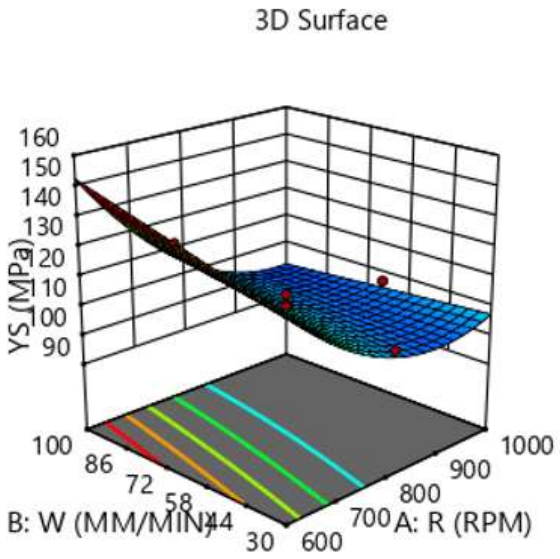

Figure 5.13: 3- D response surface of YS for tool rpm and welding speed

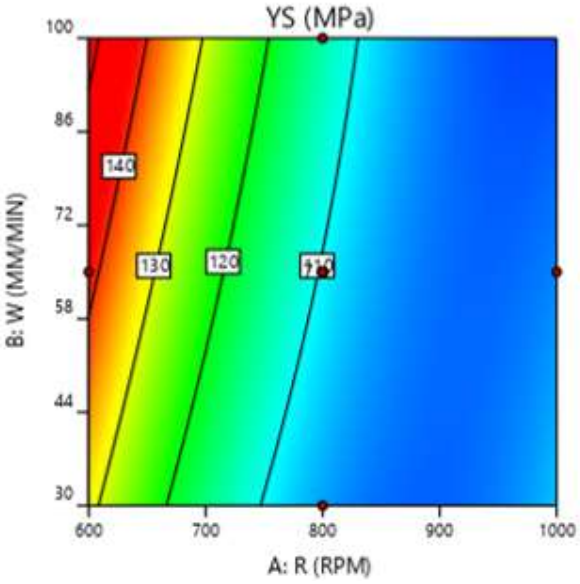

Figure 5.14: 2-D contour plot of YS for tool rpm and welding speed

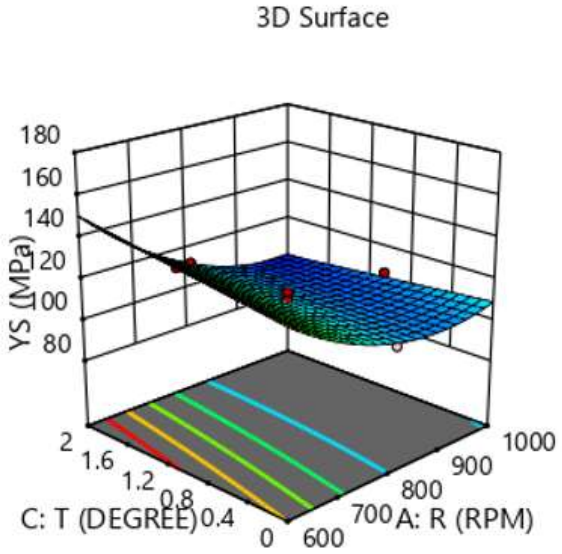

Figure 5.15: 3-D response surface of YS for tool rpm and tilt angle

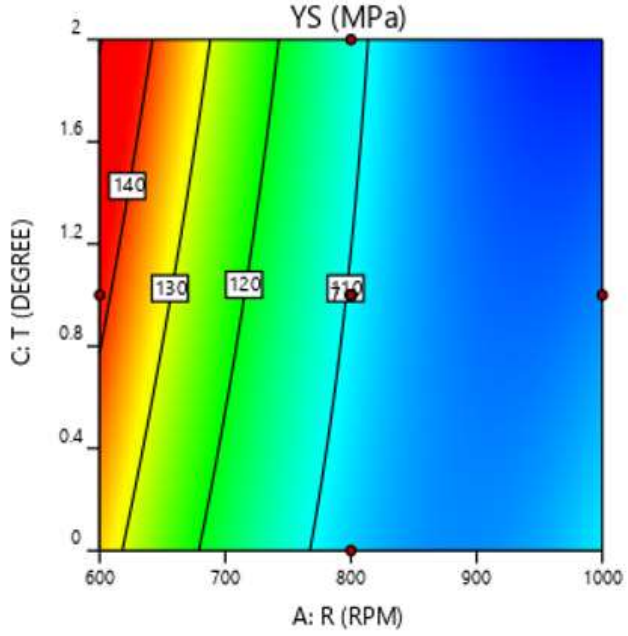

Figure 5.16: 2-Dimensional contour plot of YS for tool rpm and tilt angle

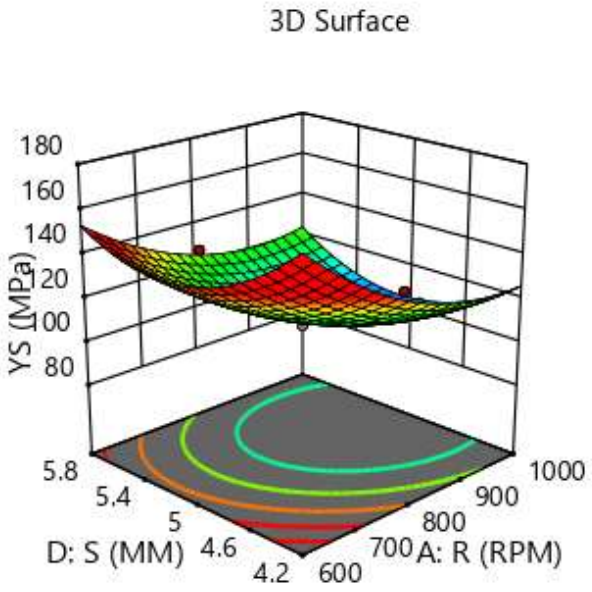

Figure 5.17: 3-D response surface of YS for tool rpm and pin size

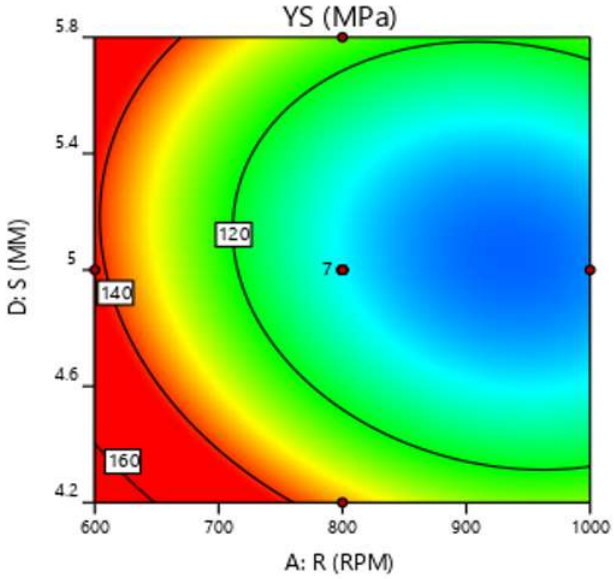

Figure 5.18: 2-D contour plot of YS for tool rpm and pin size

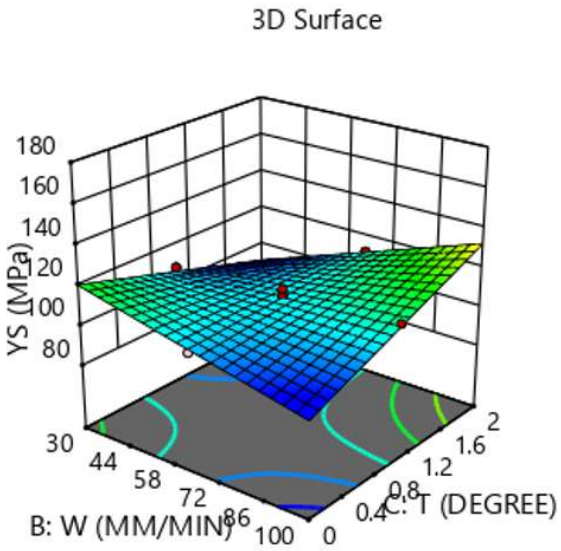

Figure 5.19: 3-D response surface of YS for welding speed and tilt angle

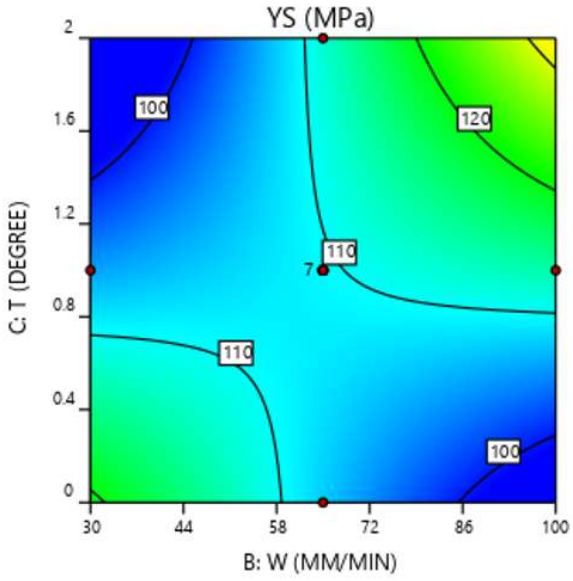

Figure 5.20: 2-D contour plot of YS welding speed and tilt angle

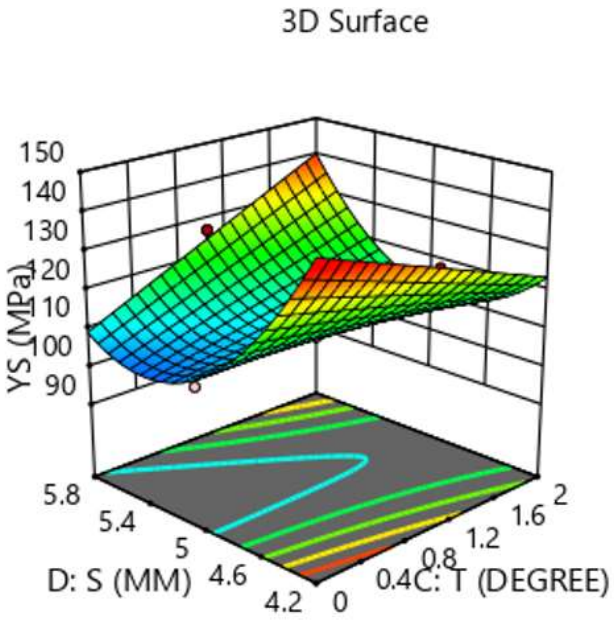

Figure 5.21:3-D response surface of YS for tool tilt angle and Pin size

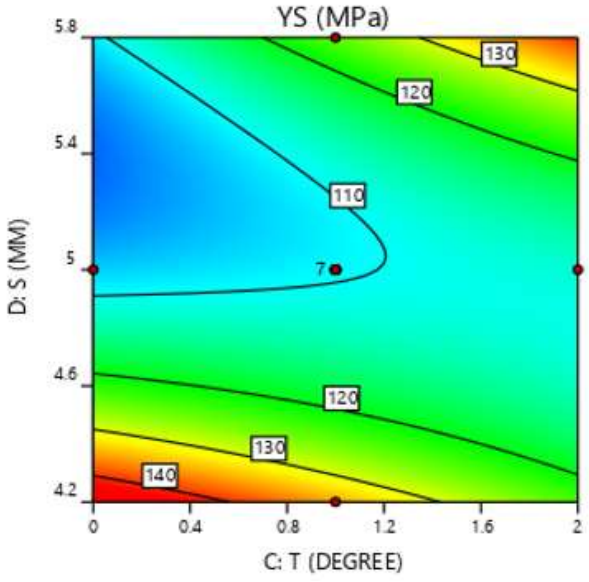

Figure 5.22:2-D contour plot of YS for tool tilt angle and Pin size

5.3.3 MAIN EFFECTS FOR RESPONSE YS

The main effect of independent factors on YS has been presented in Figure 5.23. The YS increases with an increase in rotational speed (R) till approximately 800 rpm and decreases afterward up to 1000 rpm.

The YS decreases slightly with an increase in the welding speed (W). A slight curvature has also been observed in the main effect curve of welding speed and YS.

The curve was observed approximately parallel to t the horizontal axis.

The YS value decreases with an increase in the tool tilt angle from zero degrees and becomes steady at about 1.5 degrees to 2 degrees. The curve has appreciable curvature indicating the quadratic nature.

In the main effect curve of YS and pin size, an appreciable curvature has been observed. In this plot, the YS value first increases with an increase in pin size up to 5 mm pin size and then the YS value reduces.

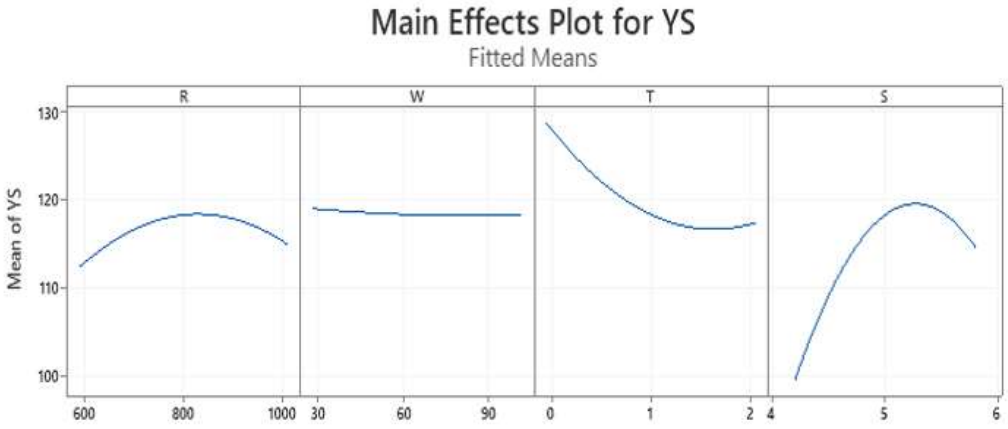

Figure 5.23: Main effect of YS

5.3.4 INTERACTION EFFECTS FOR RESPONSE YS

The interaction effects of various factors on YS have been presented in Figure 5.24 (a), (b) & (c). The value of R has a range from 600 to 1000 rpm while W has been taken at three levels i.e., 47.5, 65 and 82.5 mm/min.

Figure 5.24 (a) indicates that the change in levels of welding speed (W) (shown in different colors) results in a change in the effects of rotational speed. The effect curves of R intersect one another at different levels of W indicating the presence of a two-way interaction effect between R and W.

The curves of R at different levels of tilt angle (T) are almost parallel, indicating very slight or no interaction between R and T. The levels of T have been varied at three different levels 0.5, 1.0 and 1.5 degrees whereas R has been varied continuously from 600 to 1000 rpm.

The interaction effect of R and S on YS has been observed as significant. The value of R has been varied continuously from 600 to 1000 rpm whereas levels of S have been varied at three different levels 4.6, 5.0 and 5.4 mm. As the levels of square pin side length are varied the curves of R and YS intersect one another indicating the significant two-way interaction.

Figure 5.24 (b), intersecting curves of welding speed (W) at different levels of tilt angle (T) indicates the existence of an interaction between W and T. The levels of T have been varied at three different levels 0.5, 1.0 and 1.5 degrees whereas W has been varied continuously from 30 to 100 mm/ min. It has been observed that at T-level 0.5, the maximum value of YS may be achieved at 100 mm/min of welding speed.

The interaction effect of W and S, on YS, has been observed non-significant. The value of W has been varied continuously from 30 to 100 mm/min whereas levels of S have been varied at three different levels 4.6, 5.0 and 5.4 mm. It was investigated that at all S levels the W-YS curves do not intersect. The parallel nature of curves indicates the presence of no interaction.

The interaction effect of T and S on YS in Figure 5.24(c) has been observed as significant. The value of T has been varied continuously from zero to two degrees whereas levels of S have been varied at three different levels 4.6, 5.0 and 5.4 mm. As the levels of square pin side length are varied, the curves of T and YS intersect, indicating the existence of two-way interaction. A plot of normal probability (%) against externally studentized residuals of YS has been presented in Figure 5.25. The plot is a check to ensure that the residual follows the normal distribution for response YS. The presence of any pattern in the plot like an S-shape indicates the

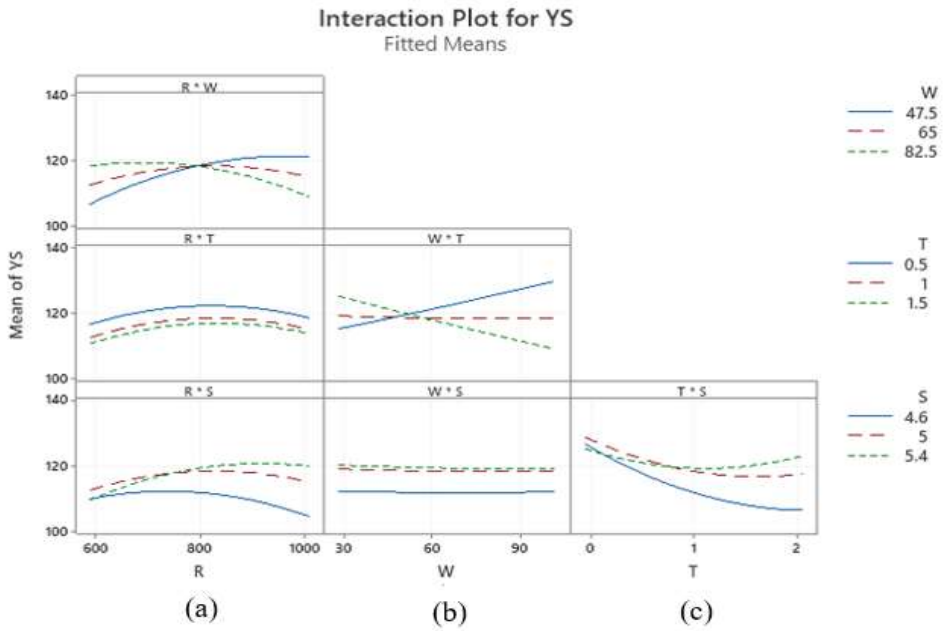

Figure 5.24: Interaction plot of yield strength

need for transformation of response for better a analysis. Figure 5.26 presents the plot of residual versus increasing predicted response values and should be randomly

scattered and should not follow any pattern. This plot ensures the assumption of constant variance for the predicted values of response YS.

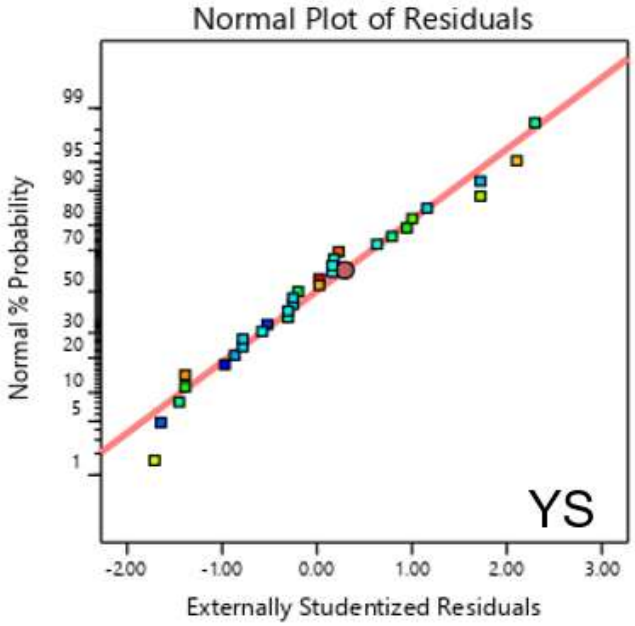

Figure 5.25: Plot of normal probability (%) against externally studentized residual

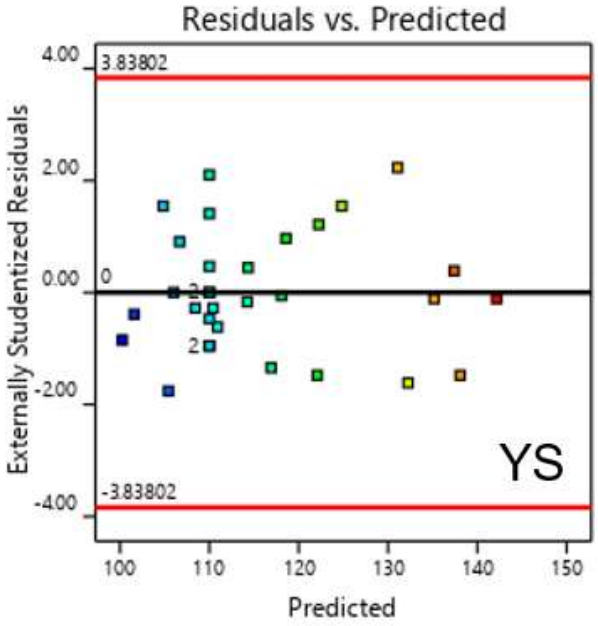

Figure 5.26: Plot of residuals versus increasing predicted response values

5.4 INFLUENCE OF INPUT PARAMETERS ON RESPONSE ELONGATION (EL)

The detailed analysis and interpretation of RSM based graphs of EL have been explained in the present section.

5.4.1 INSPECTION OF THE COMPETENCE OF THE MODEL -ANOVA FOR RESPONSE EL

Table 5.5 indicates the ANOVA table for the EL. The fit summary for EL has been presented in Table 5.6.

Table 5.5: ANOVA table for response EL

EL						
"Source"	"Sum of Squares"	"Dof"	"Mean Square"	"F-value"	"p-value"	
"Model"	269.33	14	19.24	13.21	< 0.0001	Significant
A-R	50.46	1	50.46	34.66	< 0.0001	
B-W	35.53	1	35.53	24.40	0.0001	
C-T	14.57	1	14.57	10.01	0.0060	
D-S	0.7350	1	0.7350	0.5049	0.4876	
RW	7.84	1	7.84	5.39	0.0338	
RT	1.96	1	1.96	1.35	0.2629	
RS	0.8100	1	0.8100	0.5564	0.4665	
WT	18.49	1	18.49	12.70	0.0026	
WS	4.00	1	4.00	2.75	0.1169	
TS	9.00	1	9.00	6.18	0.0243	
R^2	20.45	1	20.45	14.05	0.0018	
W^2	1.39	1	1.39	0.9566	0.3426	
T^2	25.70	1	25.70	17.65	0.0007	
S^2	71.67	1	71.67	49.23	< 0.0001	
Residual	23.29	16	1.46			
Lack of Fit	11.30	10	1.13	0.5652	0.7972	not significant
Pure Error	11.99	6	2.00			
Cor Total	292.63	30				

Table 5.6: Fit summary for response EL

"R-squared"	0.9197
"Adjusted R-squared"	0.8495
"Predicted R-squared"	0.7184
"Adequate Precision"	14.2719

The terms with a P-value of more than 0.1 indicate the non-significant terms (Table 5.5). In the model generated for the EL the significant terms are as follows:

- Significant Main effects: R, W, T, S
- Significant Interaction terms: RW, WT, TS
- Significant Quadratic terms R^2, T^2, S^2

The following terms in the estimation of EL are non-significant:

- Non-significant interaction terms: RT, RS, WS
- Non-significant Quadratic terms: W^2

The F value of lack of fit is 0.56 and the corresponding P-value 0.7972 signify that there is only a 79.72 percent probability that lack of fit of F value 0.56 may happen due to noise. R square value for the empirical model specified by Equation 5.9 is 0.9197 indicating that the remaining 8.03% of the variation in the predicted EL value could not be explained by variation in independent variables.

The adjusted R-squared value for equation 5.9 is 0.8495 and is obtained by making adjustments in the R-squared value to accommodate the increase in the latter due to less valuable multiple independent variables. The predicted R-squared value for EL is 0.7418 and its difference from the adjusted R- square value is less than 0.2. Adequate precision representing signal-to-noise ratio for EL is 14.27 which is more than 4.0 indicating that the empirical model is appropriate to navigate the design space.

5.4.2 ANALYSIS OF RESPONSE SURFACE AND CONTOUR PLOTS FOR EL

Response surface and contour plots for EL have been presented in Figure 5.27 to 5.32. The response surfaces and contour plots signify the plots of independent factors R & W, W & T, and T & S with response EL and the other two independent factors kept at the center points in each graph, respectively. Red dots in the graph indicate the design points.

Figures 5.27 and 5.28 present the response and contour plot of tool rpm (R) and welding speed (W) while fixing the remaining factors at their respective center point values. The response surface indicates the maximum value of EL at 1000 rpm tool rpm and 30 mm/min welding speed. The contour plot of W and T is not circular and two-way interaction between the two parameters may be concluded.

The response surfaces and contour plots in Figures 5.29 and 5.30 show the variation of EL when traverse speed (W) and the tilt angle (T) are varied while keeping the other two input parameters at a constant value (center points). Curvature in the response surface has been observed along an axis parallel to that of the tool tilt angle. Since circular contour is not present the existence of the interaction effect may be concluded. Figure 5.31 and 5.32 present response surfaces and contour plot of tilt angle and the pin size while keeping rotation rpm and traverse speed at constant levels (center points). As the contour plot is elliptical, the presence of the interaction effect may be concluded. The maximum value curve of the response EL could be observed in the contour plot at tilt angle varying from zero to 1.6 degrees and pin size at 4.2 mm respectively.

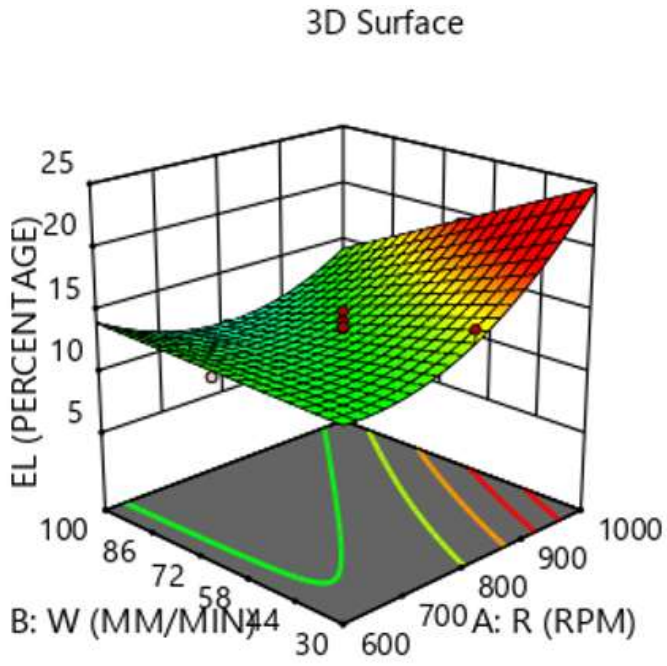

Figure 5.27: 3-D response surface for EL of rotation speed and traverse speed

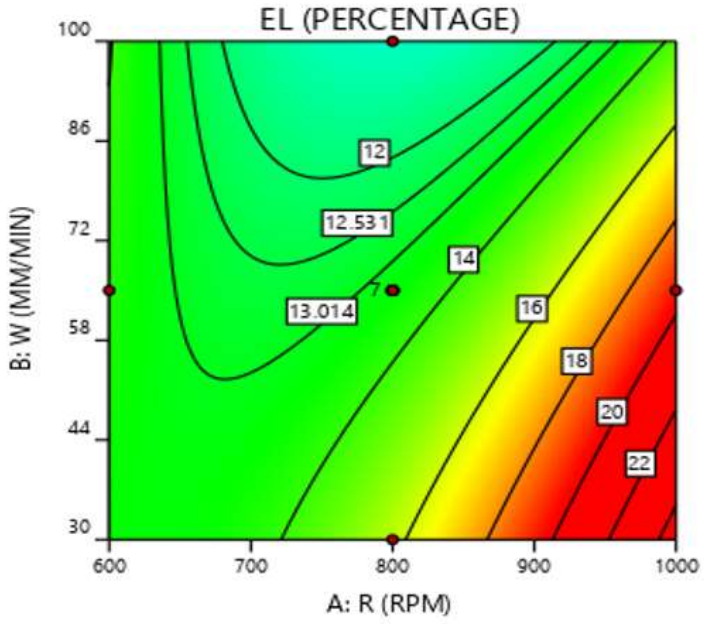

Figure 5.28: 2-D contour plot of EL for-rotation speed and traverse speed

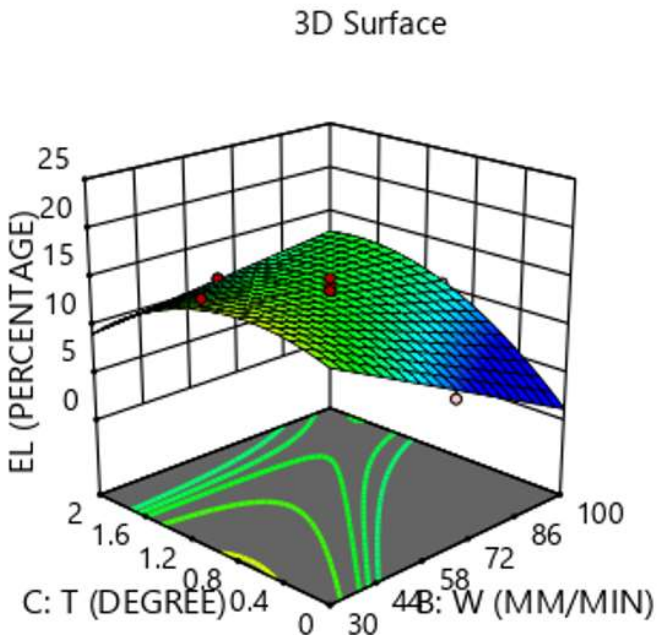

Figure 5.29:3-D response surface of EL for-welding speed and tilt angle

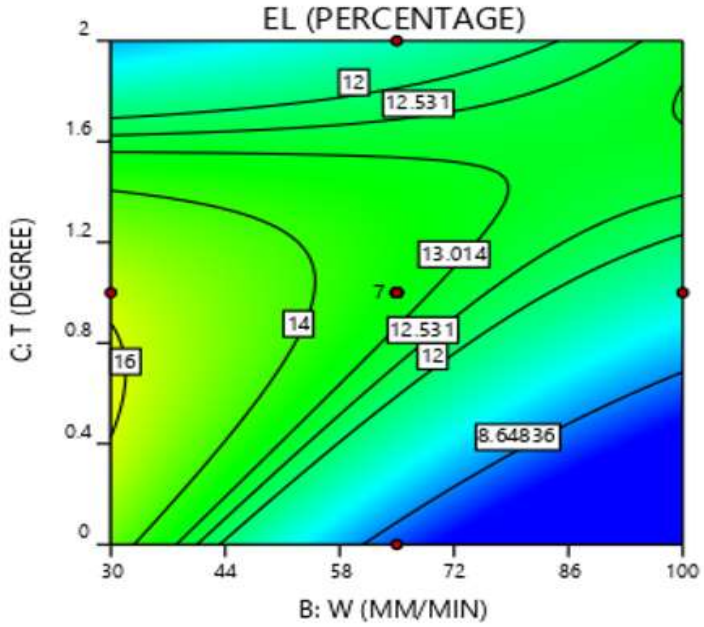

Figure 5.30: 2-D contour plot for EL of welding speed and tilt angle

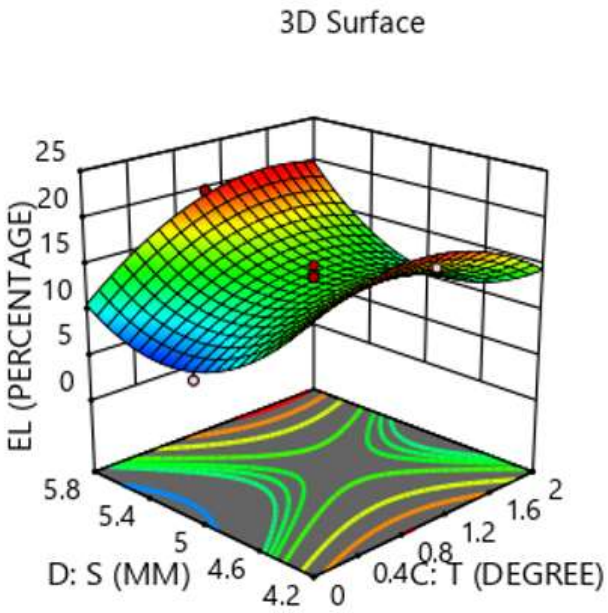

Figure 5.31: 3-D response surface for EL of tilt angle and pin size

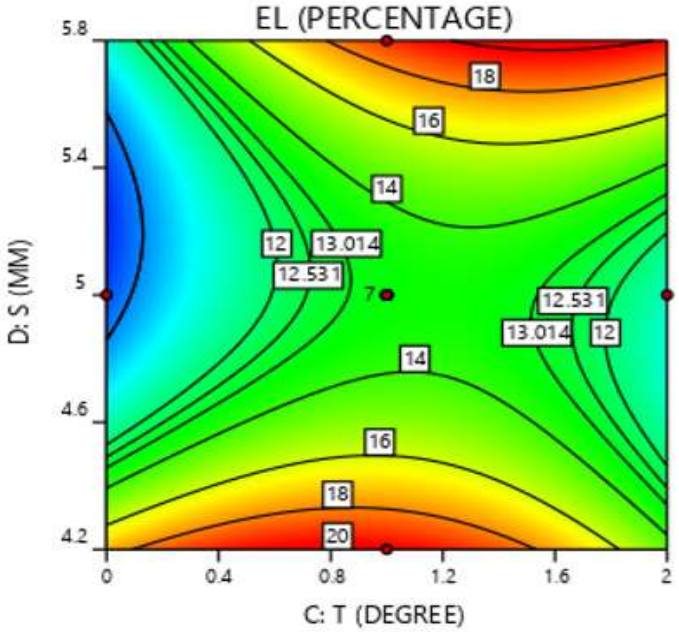

Figure 5.32: 2-D contour plot for EL of tilt angle and pin size

5.4.3 MAIN EFFECTS FOR RESPONSE EL

The main effects of all the input parameters on EL have been presented in Figure 5.33. With an increase in tool rpm up to 800 rpm, the main effect EL first decreases and increases continuously afterward, while keeping other factors at center levels. An appreciable amount of curvature has been observed in the main effect curve of R. With an increase in tool traverse speed up to approximately 60 mm/min, the main effect first decreases, and increases continuously afterward, while holding other factors at center levels. Some amount of curvature has been observed in the main effect curve of W but the amplitude of curvature was less than that of R. With an increase in tool tilt angle up to a few degrees, the main effect EL remains constant and starts increasing continuously to 12 percent while holding other factors at center levels. Some amount of curvature has been observed in the main effect of the curve of EL with respect to T. With an increase in pin size from 4.2 mm to 5.4 mm, the main effect increases, and decreases slightly afterward while holding other factors at center levels. Some amount of curvature has been observed in the main effect of EL with respect to S

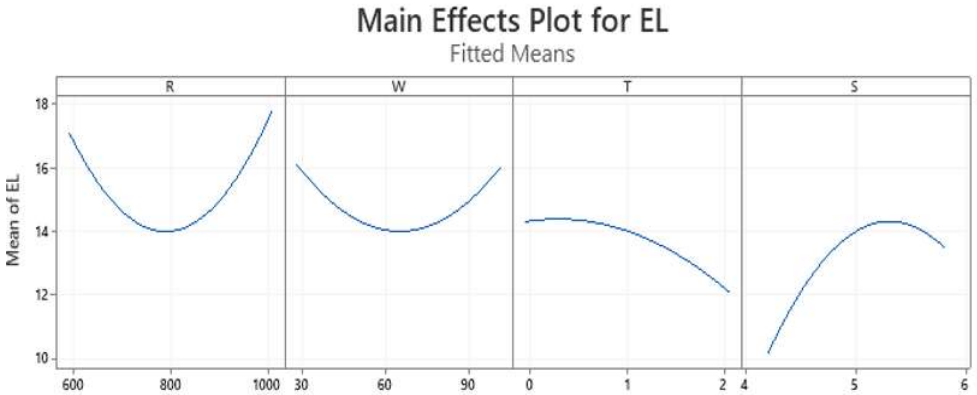

Figure 5.33: Main effects plot for EL

5.4.4 INTERACTION EFFECTS FOR RESPONSE EL

The interaction effects of various factors on EL have been presented in Figure 5.34 (a), (b) & (c). The value of R ranges from 600 to 1000 rpm while W has been taken at three levels i.e. 47.5, 65 and 82.5 mm/min.

Figure 5.34 (a) indicates that the change in levels of welding speed (W) (shown in different colors) results in a change in the effects of rotational speed. The effect curves of R intersect one another at different levels of W indicating the presence of a two-way interaction effect between R and W.

The intersecting curves of R at different levels of tilt angle (T) indicate the existence of an interaction between R and T. The levels of T have been varied at three different levels 0.5, 1.0 and 1.5 degrees whereas R has been varied continuously from 600 to 1000 rpm.

The interaction effect of R and S on EL has been observed as significant. The value of R has been varied continuously from 600 to 1000 rpm whereas levels of S have been varied at three different levels 4.6, 5.0 and 5.4 mm. As the levels of square pin side length are varied the curves of R and EL intersect one another indicating the significant two-way interaction.

The intersecting curves of welding speed (W) at different levels of tilt angle (T) are presented in Figure 5.34 (b) indicate the existence of an interaction between W and T. The levels of T have been varied at three different levels 0.5, 1.0 and 1.5 degrees whereas W has been varied continuously from 30 to 100 mm/ min. It has been observed that at T-level 0.5, the maximum value of EL may be achieved at 100 mm/min of welding speed.

The interaction effect of W and S, on EL, has been observed non-significant. The value of W has been varied continuously from 30 to 100 mm/min whereas levels of S have been varied at three different levels 4.6, 5.0 and 5.4 mm. It was investigated that at all S levels the W-EL curves do not intersect in the range of the process parameters levels.

The interaction effect of T and S, on EL presented in Figure 5.34 (c), has been observed as significant. The value of T has been varied continuously from zero to two degrees whereas levels of S have been varied at three different levels 4.6, 5.0 and 5.4 mm. As the levels of square pin side length are varied, the curves of T and EL, intersect, indicating the existence of two-way interaction.

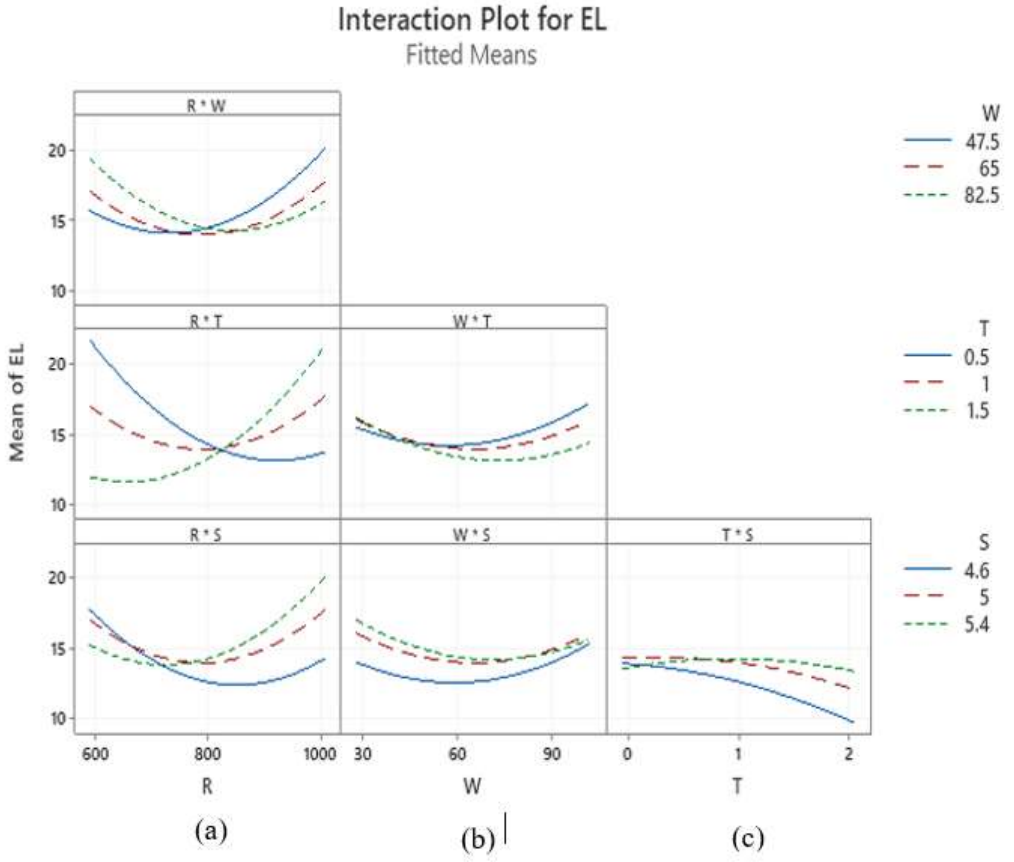

Figure 5.34: Interaction effects plot for EL

A plot of normal probability (%) against externally studentized residuals of EL has been presented in Figure 5.35. The plot is a check to ensure that the residual follows the normal distribution for response EL. The presence of any pattern in the plot like an S-shape indicates the need for transformation of response for better analysis. Figure 5.36 presents the plot of residuals versus increasing predicted response values and should be randomly scattered and should not follow any pattern. This plot ensures the assumption of constant variance for the predicted values of response EL.

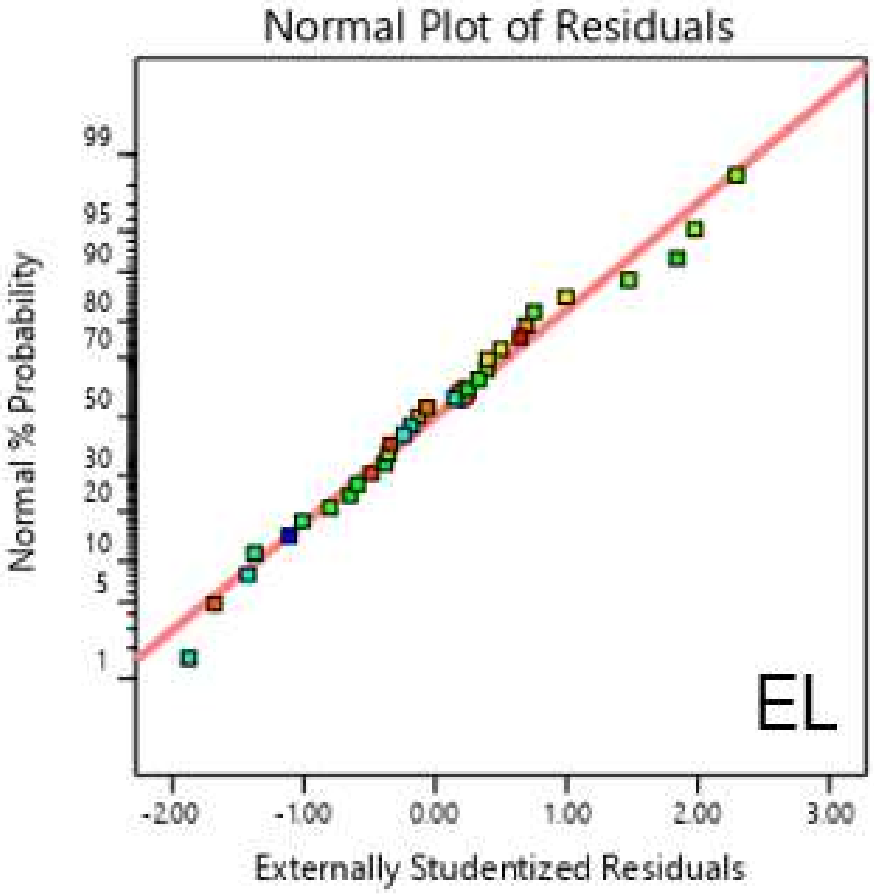

Figure 5.35: Plot of normal probability (%) against externally studentized residuals of EL

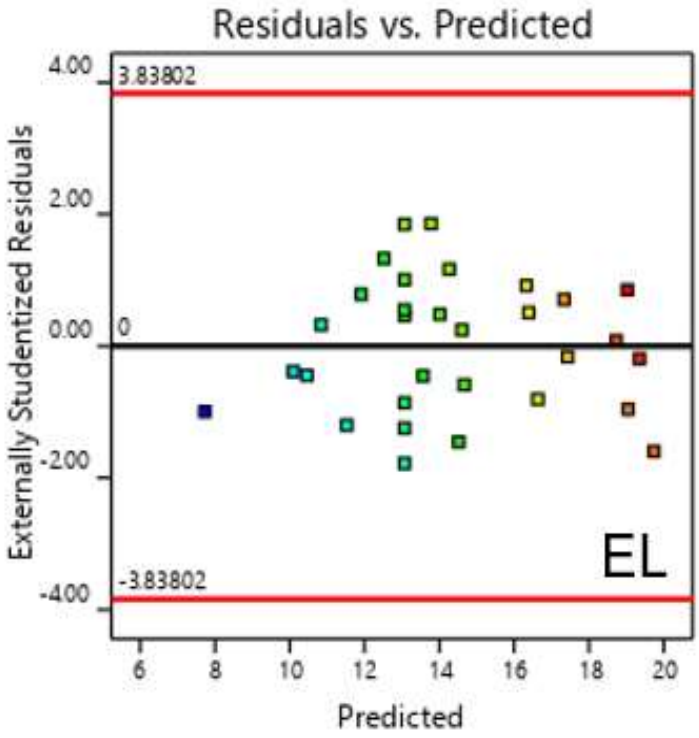

Figure 5.36: Plot of externally studentized residuals versus increasing predicted response

5.5 INFLUENCE OF INPUT PARAMETERS ON IMPACT STRENGTH (I)

The detailed analysis and interpretation of RSM based graphs of 'I' have been explained in the present section.

5.5.1 INSPECTION OF THE COMPETENCE OF THE MODEL - ANOVA FOR I

Table 5.7 indicates the ANOVA table for the response 'I'. The fit summary for I has been presented in Table 5.8.

Table 5.7: ANOVA table of 'I'

"Source"	"Sum of Squares"	"Dof"	"Mean Square"	"F-value"	"p-value"	
"Model"	922.38	14	65.88	26.71	< 0.0001	Significant
A-R	4.02	1	4.02	1.63	0.2200	
B-W	111.80	1	111.80	45.33	< 0.0001	
C-T	211.70	1	211.70	85.83	< 0.0001	
D-S	105.50	1	105.50	42.78	< 0.0001	
RW	0.0506	1	0.0506	0.0205	0.8879	
RT	24.30	1	24.30	9.85	0.0063	
RS	8.35	1	8.35	3.39	0.0844	
WT	3.74	1	3.74	1.52	0.2357	
WS	16.20	1	16.20	6.57	0.0209	
TS	75.34	1	75.34	30.55	< 0.0001	
R^2	72.44	1	72.44	29.37	< 0.0001	
W^2	251.67	1	251.67	102.04	< 0.0001	
T^2	5.80	1	5.80	2.35	0.1446	
S^2	103.00	1	103.00	41.76	< 0.0001	
Residual	39.46	16	2.47			
Lack of Fit	31.46	10	3.15	2.36	0.1527	not significant
Pure Error	8.00	6	1.33			
Cor Total	961.84	30				

Table 5.8: Fit summary for the response I

"R-squared"	0.9590
"Adjusted R-squared"	0.9231
"Predicted R-squared"	0.8003
"Adequate Precision"	18.9334

The terms with a P-value of more than 0.1 indicate the non-significant terms. In the model generated for the response 'I', the significant terms are as follows:

- Significant Main effects: R, W, T, S
- Significant Interaction terms: RT, RS, WS and TS
- Significant Quadratic terms R^2, W^2, S^2

The following terms in the estimation of 'I' are non-significant:

- Non-significant Interaction terms: RW, WT
- Non-significant Quadratic terms: T^2

The F value of lack of fit is 2.36 and the corresponding P-value 0.1527 signifies that there is only a 15.27 percent probability that lack of fit of F value 2.36 may happen due to noise. R squared value for the empirical model specified by Equation 5.10 is 0.9590 indicating that the remaining 4.1 % of the variation in the predicted 'I' value could not be explained by variation in independent variables.

The adjusted R-squared value for equation 5.10 is 0.9231 and is obtained by making adjustments in the R-squared value to accommodate the increase in the latter due to less valuable multiple independent variables. The predicted R-squared value for 'I' is 0.8003 and its difference from the adjusted R- squared value is less than 0.2. Adequate precision representing signal-to-noise ratio for 'I' is 18.9334 which is more than 4.0 indicating that the empirical model is appropriate to navigate the design space.

5.5.2 ANALYSIS OF RESPONSE SURFACE AND CONTOUR PLOTS FOR 'I'

Response surfaces and contour plots for 'I' have been presented in Figures 5.37 to 5.44. The response surfaces and contour plots signify the plots of independent

factors R & T, R & S, and W & S and T & S with the response ‘I’ and the other two independent factors kept at the center points in each graph, respectively. Red dots in the graphs indicate the design points.

Figure 5.37 and Figure 5.38 present the response and contour plots of tool rpm (R) and tilt angle (T) while fixing the remaining factors at their respective center point values. The response surface indicates the maximum value of ‘I’ at 1000 rpm tool speed and 2 degrees tilt angle. The contour plot of R and T is elliptical, the two-way interaction between the two parameters may be concluded.

The response surface and the contour plot in Figure 5.39 and Figure 5.40 show the variation of ‘I’ when tool rpm (R) and the pin size (S) are varied while keeping the other two input parameters at a constant value (center points). Since circular contour is not present the existence of the interaction effect may be concluded.

Figure 5.41 and 5.42 present response surface and contour plot of traverse speed (W) and the pin size (S) while keeping rotation rpm and tilt angle at constant levels (center points). As the contour plot is elliptical, the presence of the interaction effect may be concluded.

Figure 5.43 and 5.44 present the response surface and contour plot of tilt angle (T) and the pin size (S) while keeping rotation rpm and traverse speed at constant levels (center points). As the contour plot is elliptical, the presence of the interaction effect may be concluded. The response surface and contour plot indicate the maximum value of ‘I’ at 2 degrees tilt angle and 5.8 mm pin size. The response surfaces and contour plots of response ‘I’ have been manifested subsequently:

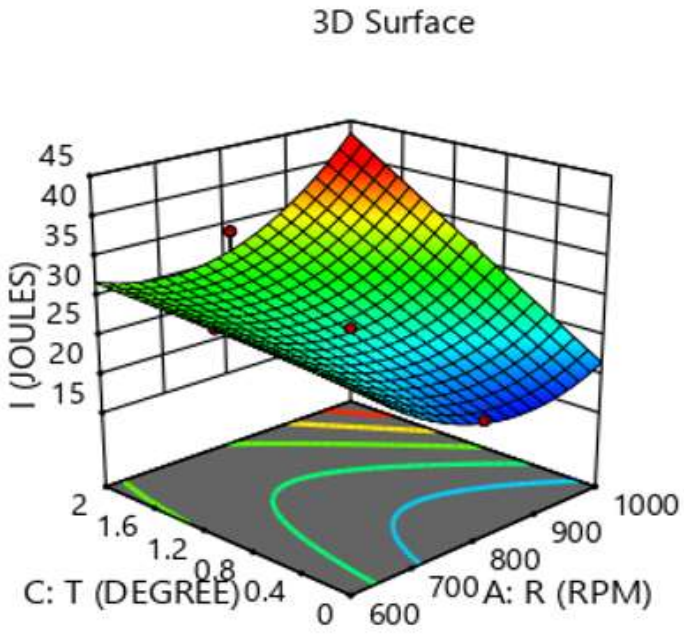

Figure 5.37: 3-D response surface of I for-tool rpm and tilt angle

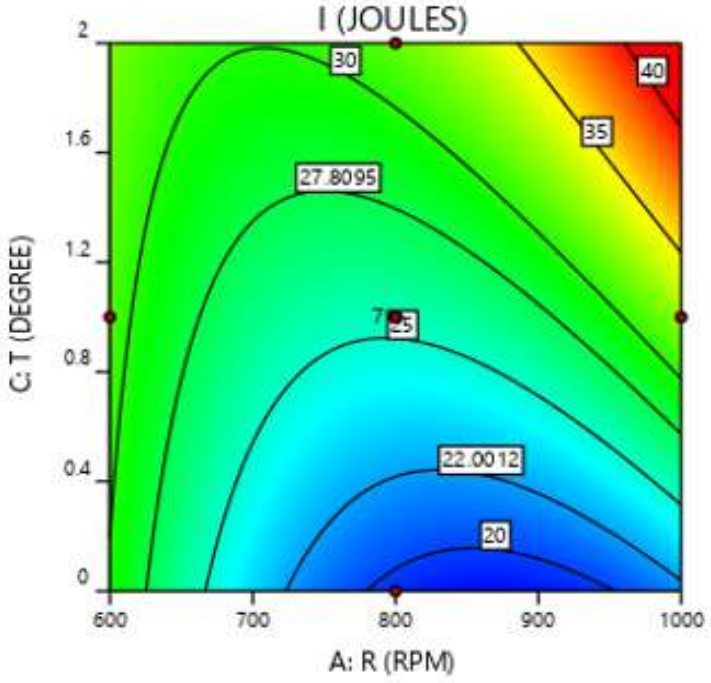

Figure 5.38: 2-D contour plot of I for- tool rpm and tilt angle

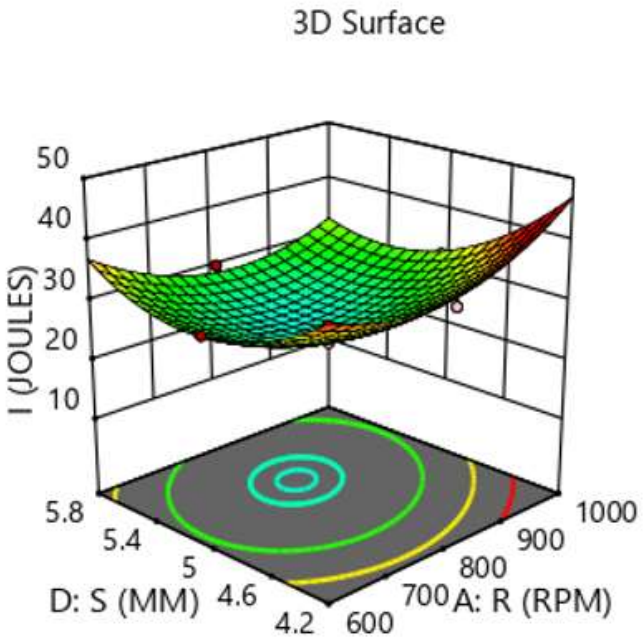

Figure 5.39: 3-D response surface of I for-tool rpm and pin size

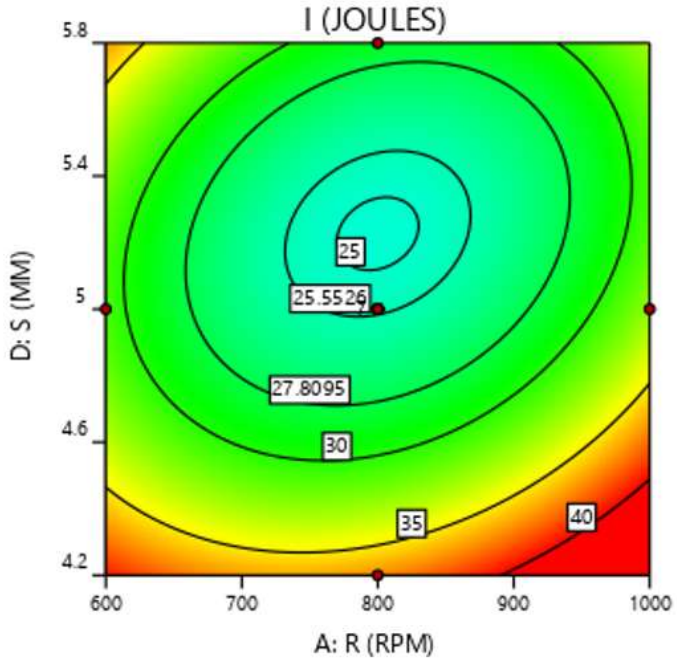

Figure 5.40: 2D contour plot of I – tool rpm and pin size

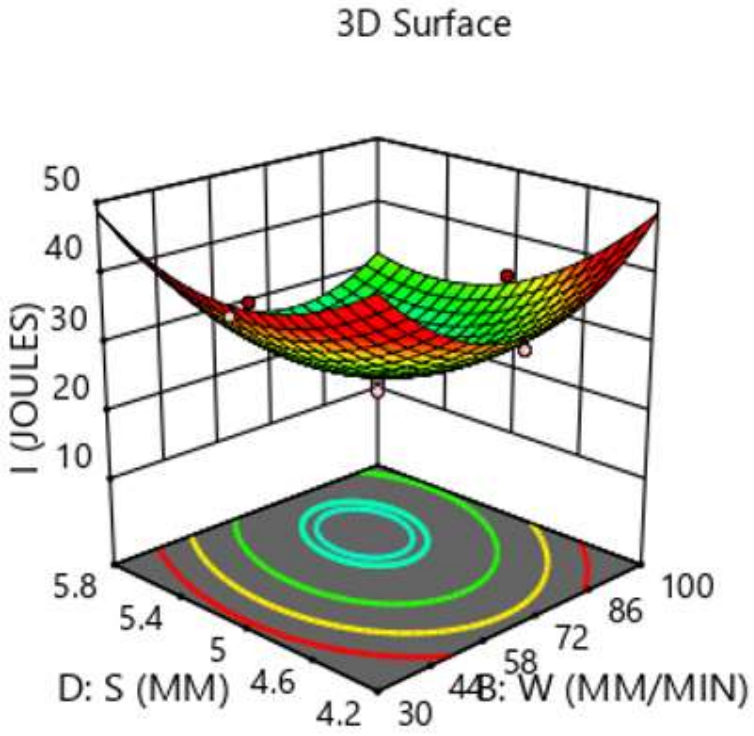

Figure 5.41: 3-D response surface of I-welding speed and pin size

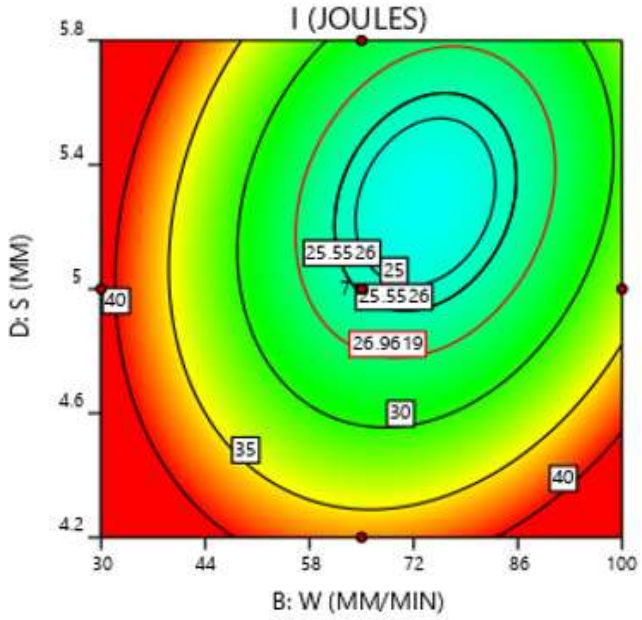

Figure 5.42: 2-D contour plot of I for-welding speed and pin size

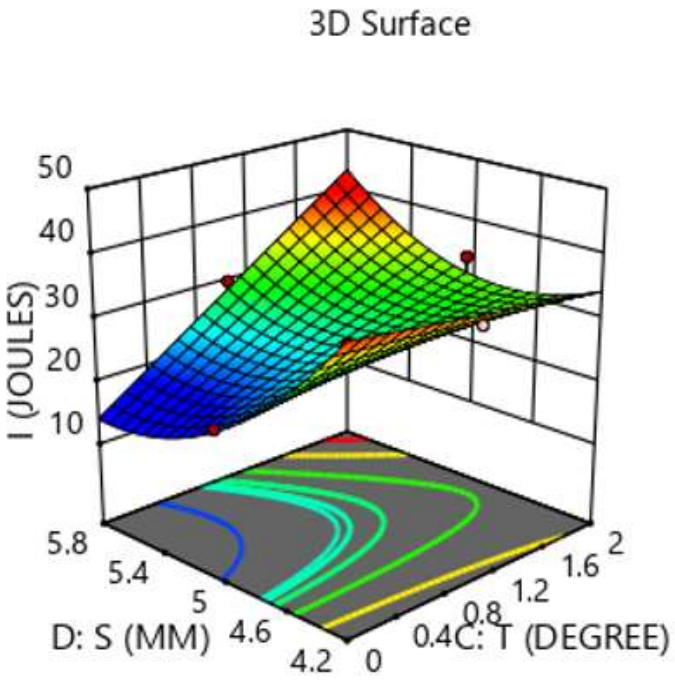

Figure 5.43: 3-D response surface of I for tilt angle and pin size

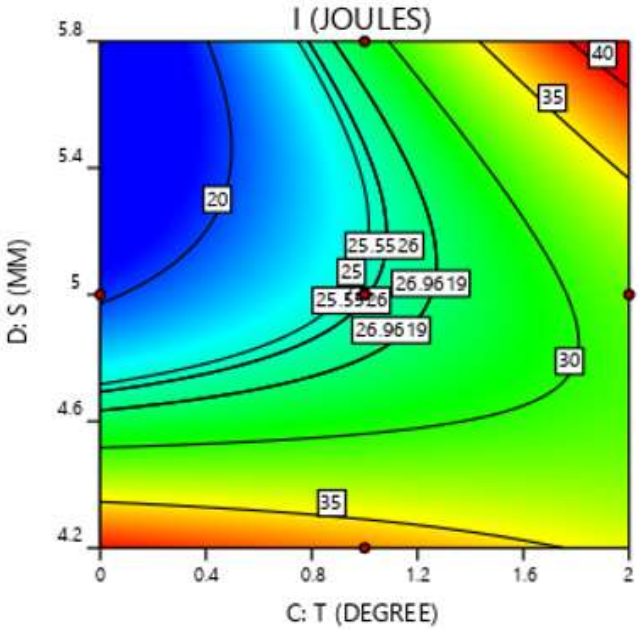

Figure 5.44: 2-D contour plot of I for tilt angle and pin size

5.5.3 MAIN EFFECTS FOR RESPONSE I

The main effects of all the input parameters on 'I' have been presented in Figure 5.45. With an increase in tool rpm up to 800 rpm, the main effect of 'I' first decreases, and increases continuously afterward, while keeping other factors at center levels. An appreciable amount of curvature has been observed in the main effect curve of R.

With an increase in tool traverse speed up to approximately 65 mm/min, the main effect 'I' first decreases, and increases continuously afterward, while holding other factors at center levels. The curvature has been observed in the main effect curve of W but the amplitude of curvature was less than that of R.

With an increase in tool tilt angle, the main effect 'I' constantly decreases, while holding other factors at center levels. Slight curvature has been observed in the main effect curve of 'I' with respect to T.

With an increase in pin size from 4.2 mm to 5.4 mm, the main effect 'I' increases, and decreases slightly afterward, while holding other factors at center levels. Slight curvature has also been observed in the main effect of 'I' with respect to S.

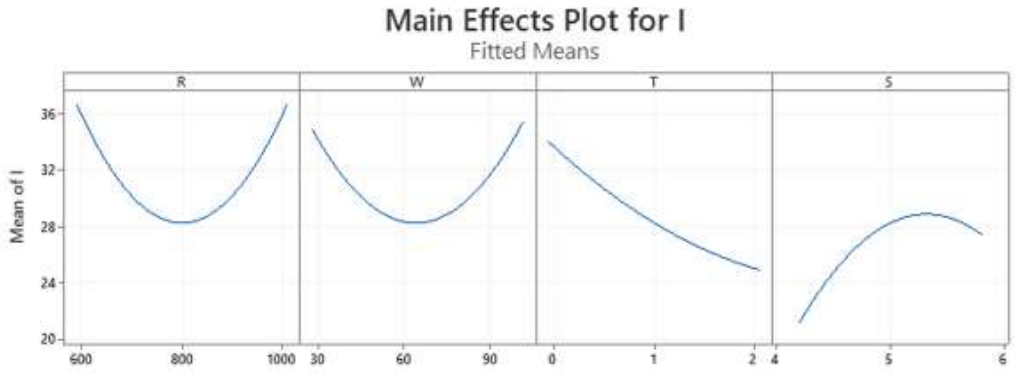

Figure 5.45: Main effects plot for I

5.5.4 INTERACTION EFFECTS FOR RESPONSE 'I'

The interaction effects of various factors on 'I' have been presented in Figure 5.46, a, b & c. The value of R has a range from 600 to 1000 rpm while W has been taken at three levels i.e. 47.5, 65 and 82.5 mm/min. The first plot indicates that the change in levels of welding speed (W) (shown in different colors) results in a change in the effects of rotational speed. The effect curves of R intersect one another at different levels of W indicating the presence of a two-way interaction effect between R and W.

The levels of T have been varied at three different levels 0.5, 1.0 and 1.5 degrees whereas R has been varied continuously from 600 to 1000 rpm. The intersecting curves of R at different levels of tilt angle (T) indicate the existence of an interaction between R and T. But the interaction has been observed only at 1000 rpm. The value of R has been varied continuously from 600 to 1000 rpm whereas levels of S have been varied at three different levels 4.6, 5.0 and 5.4 mm. The interaction effect of R and 'S' on 'I' has been observed non-significant for pin size at 4.6 mm & 5mm and 4.6 mm & 5.4 mm. But at S levels of 5 mm & 5.4 mm the R & response 'I' curves intersect one another indicating the significant two-way interaction.

The levels of T have been varied at three different levels 0.5, 1.0 and 1.5 degrees whereas W has been varied continuously from 30 to 100 mm/min. The intersecting curves of welding speed (W) at different levels of tilt angle (T) indicate the existence of an interaction between W and T. It has been observed that at T-level 0.5, the maximum value of 'I' may be achieved at 30 mm/min of welding speed.

The value of W has been varied continuously from 30 to 100 mm/min whereas levels of S have been varied at three different levels 4.6, 5.0 and 5.4 mm.

The interaction effect of W and S, on ‘I’, has been observed as non-significant. It was investigated that at all S levels the W-’I’ curves do not intersect in the range of the process parameters levels.

The interaction effect of T and S, on ‘I’, has been observed as significant. The value of T has been varied continuously from zero to two degrees whereas levels of S have been varied at three different levels 4.6, 5.0 and 5.4 mm. As the levels of square pin side length are varied, the curves of T and ‘I’, intersect, indicating the existence of two-way interaction.

A plot of normal probability (%) against externally studentized residuals of ‘I’ has been presented in Figure 5.47. The plot is a check to ensure that the residual curvefollows the normal distribution for response ‘I’. The presence of any pattern in the plot like an S-shape indicates the need for transformation of response for better analysis. Figure 5.48 presents the plot of residuals versus increasing predicted response values and should be randomly scattered and should not follow any pattern.

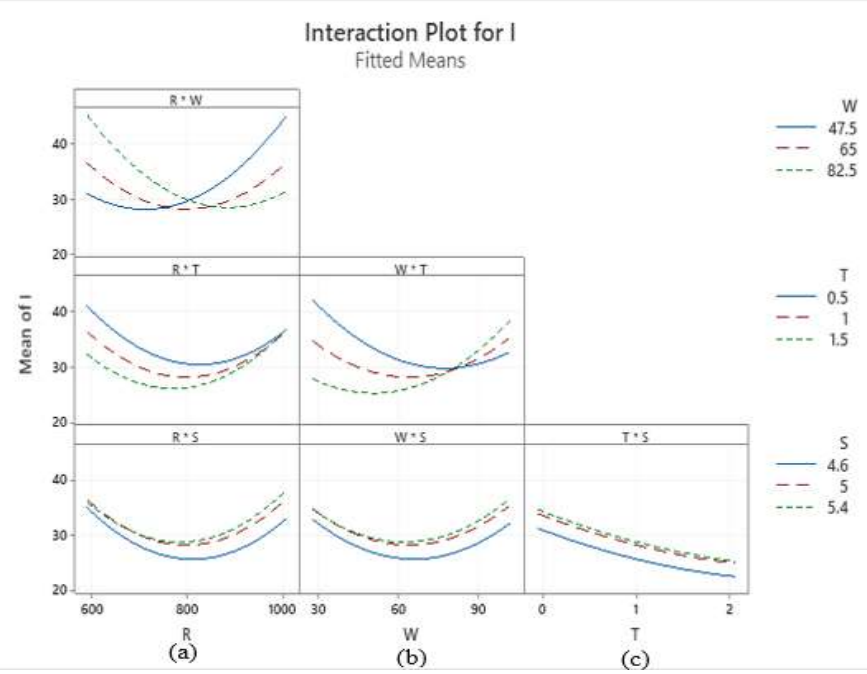

Figure 5.46: Interaction effects plots for I

This plot ensures the assumption of constant variance for the predicted values of response ‘I’.

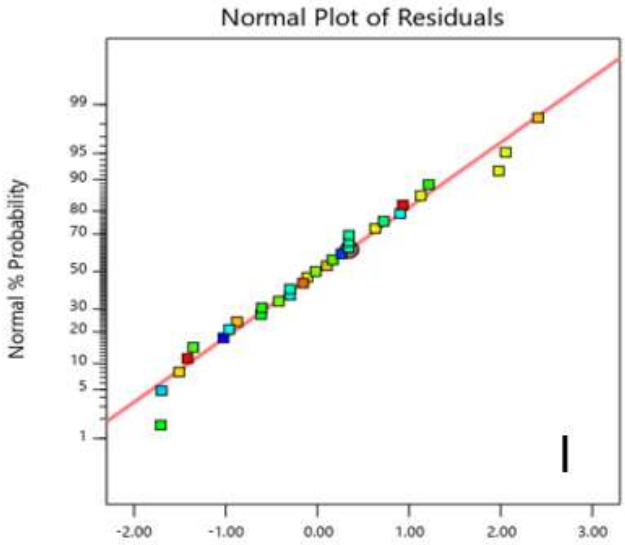

Figure 5.47: Plot of normal probability (%) & externally studentized residuals of I

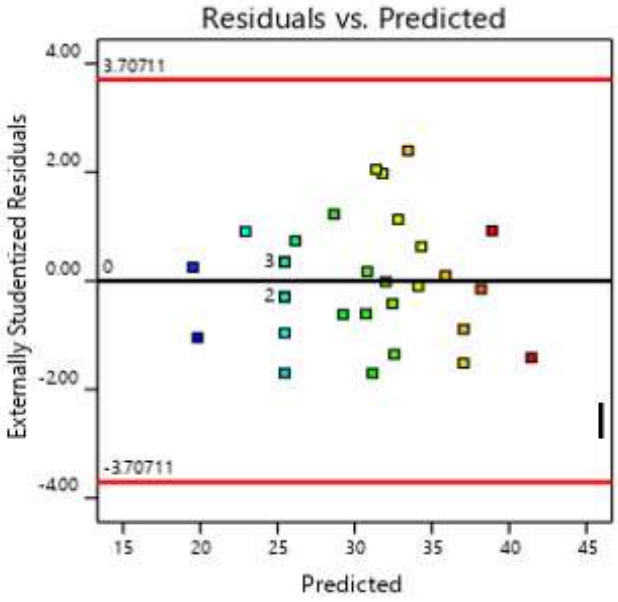

Figure 5.48: Plot of predicted values & externally studentized residuals of I

5.6 REDUCTION OF MODEL

It was observed that the equations generated (equations 5.7-5.10) constitute both significant and non-significant terms. The different terms of having a P-value of more than 0.1 were non-significant. After omitting the non-significant terms fit statistics terms were changed. A comparison between the fit statistics before and after the reduction of the equation has been presented in Table 5.9.

Table 5.9: Comparison of fit statistics before and after the reduction of model

		BEFORE REDUCTION	AFTER REDUCTION
UTS	R-squared	0.9640	0.9583
	Adjusted R-squared	0.9324	0.9305
	Predicted R-squared	0.8216	0.8492
	Adequate Precision	24.3442	25.4652
YS	R-squared	0.9796	0.9776
	Adjusted R-squared	0.9618	0.9646
	Predicted R-squared	0.9111	0.9286
	Adequate Precision	26.6180	30.5853
EL	R-squared	0.9197	0.8918
	Adjusted R-squared	0.8495	0.8377
	Predicted R-squared	0.7184	0.7418
	Adequate Precision	14.2719	16.0477
Impact strength (I)	R-squared	0.9590	0.9490
	Adjusted R-squared	0.9231	0.9195
	Predicted R-squared	0.8003	0.8430
	Adequate Precision	18.9334	21.9370

It has been observed that although R-squared and Adjusted R-squared have decreased whereas predicted R squared and adequate precision has improved. It is more important to achieve high predicted R-squared and adequate precision than to achieve R-squared and adjusted R-squared.

5.6.1 ACTUAL EQUATIONS AFTER REDUCTION OF MODEL

$$UTS = 929.73 - 0.604\,R + 1.47\,W - 50.53\,T - 208.28\,S - 0.066\,RT + 0.721\,WT - 0.330\,WS + 20.94\,TS + 0.0003\,R^2 - 0.004\,W^2 - 19.4821\,T^2 + 17.99\,S^2 \quad (5.13)$$

$$YS = 1341 - 0.665\,R + 0.403\,W - 83.9\,T - 354.7\,S - 0.000929\,RW - 0.032\,RT + 0.0250\,RS + 0.4857\,WT + 16.88\,TS + 0.000338\,R^2 + 31.25\,S^2 \quad (5.14)$$

$$EL = 272.21 - 0.074\,R + 0.3963\,W - 23.06\,T - 93.67\,S - .0004\,RW + 3.77\,TS + 0.121\,WT + 0.00008\,R^2 - 3.79\,T^2 + 9.86\,S^2 \quad (5.15)$$

$$I = 433.67 - 0.17\,R - 0.64\,W - 68.06\,T - 107.93\,S + 0.024\,RT - 0.018\,RS - 0.143\,WS + 10.85\,TS + 0.00015\,R^2 + 0.009\,W^2 + 11.56\,S^2 \quad (5.16)$$

Some main effect terms/interaction terms have been retained in the reduced equations to maintain the hierarchy during the reduction of the model. The actual equations are used to predict dependent mechanical properties. The coefficient terms in actual form should not be used to compare the relative effect of the various terms. A comparison of predicted values generated from the model and experimental values has been presented in Table 5.10. The differences between experimental and predicted values (residuals) were found small. The scatter diagrams representing plots between predicted values and the experimental values have been presented in Figures 5.49, 5.50, 5.51 and 5.52. A decent agreement between the two values was assured from the scatter diagrams.

5.6.2 DETERMINATION OF COEFFICIENTS IN CODED FORM

After the omission of insignificant terms, the model in actual form was developed. The model developed can be used to predict the responses for different values/levels of input factors. The levels of the factors should be considered in their original units. As each factor has a different unit, the equations should not be used to quantify their relative significance because coefficients are scaled to accommodate

Table 5.10: Experimental and predicted values of output parameters

Std order	UTS (MPa)		YS MPa)		EL (%)		I (Joules)	
	Expt	Pred	Expt	Pred	Expt	Pred	Expt	Pred
1	176	175.17	130	132.48	14.2	14.99	35.1	34.34
2	175	177.71	118	118.31	18.8	19.29	34.0	34.13
3	176	172.92	134	131.06	13.5	11.80	32.0	32.02
4	176	175.46	110	110.39	15.1	13.30	34.0	31.81
5	175	169.88	124	122.48	12.5	12.90	36.0	33.45
6	158	159.17	101	101.81	17.9	17.20	38.0	38.19
7	192	192.88	136	138.06	14.4	14.02	29.2	31.13
8	179	182.17	110	110.89	16	15.52	36.0	35.87
9	168	165.33	120	118.56	15.2	13.14	28.5	29.24
10	168	167.88	108	108.39	17.3	17.44	27.0	26.13
11	150	153.83	115	117.14	9.8	9.95	24.0	22.92
12	155	156.38	99	100.48	10.1	11.45	18.6	19.81
13	173	176.79	120	122.06	13.4	14.05	36.0	37.05
14	165	166.08	103	105.39	18.3	18.35	40.0	38.89
15	191	190.54	138	137.64	14.8	15.17	30.0	30.73
16	180	179.83	114	114.48	17.1	16.67	31.0	32.57
17	187	189.46	142	141.96	13.2	13.69	31.0	30.82
18	185	181.29	107	104.63	19.2	19.49	32.0	32.45
19	161	161.63	108	105.82	16.8	15.73	40.0	41.45
20	175	173.13	115	113.49	10.6	10.86	34.0	32.82
21	144	144.29	106	107.65	6.9	7.82	19.9	19.53
22	164	162.46	112	111.65	11.1	10.96	34.0	31.40
23	189	190.46	135	134.96	18.6	19.89	35.5	37.04
24	181	178.29	127	124.63	19.7	19.19	29.9	28.64
25	171	172.86	109	109.65	14.2	13.30	25.0	25.46
26	174	172.86	110	109.65	11.2	13.30	24.0	25.46
27	176	172.86	111	109.65	13.6	13.30	25.0	25.46
28	172	172.86	114	109.65	15	13.30	26.0	25.46
29	174	172.86	108	109.65	11.7	13.30	23.0	25.46
30	173	172.86	110	109.65	12.1	13.30	26.0	25.46
31	170	172.86	108	109.65	13.7	13.30	26.0	25.46

the units of each factor. The factor coefficients of the equations in coded form may be used to identify the relative impact of each factor.

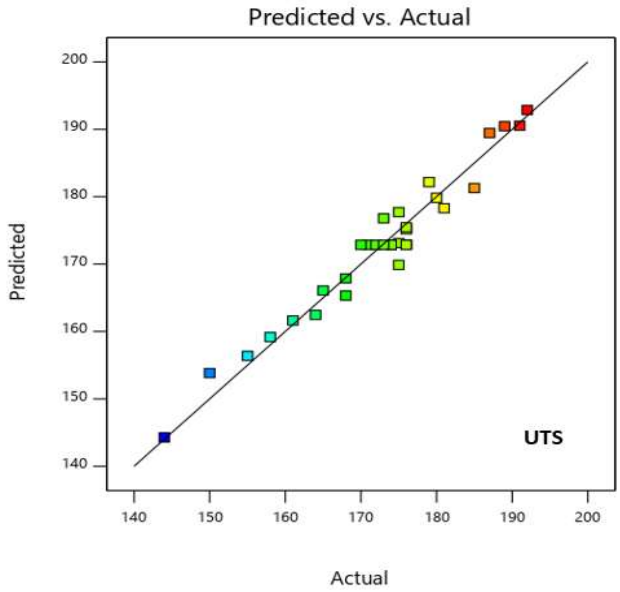

Figure 5.49: Plot of predicted & actual values of ultimate tensile strength

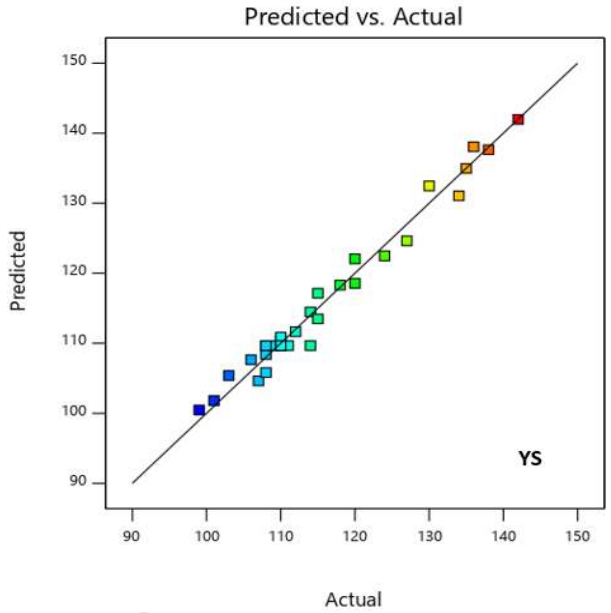

Figure 5.50: Plot of predicted & actual values of yield strength

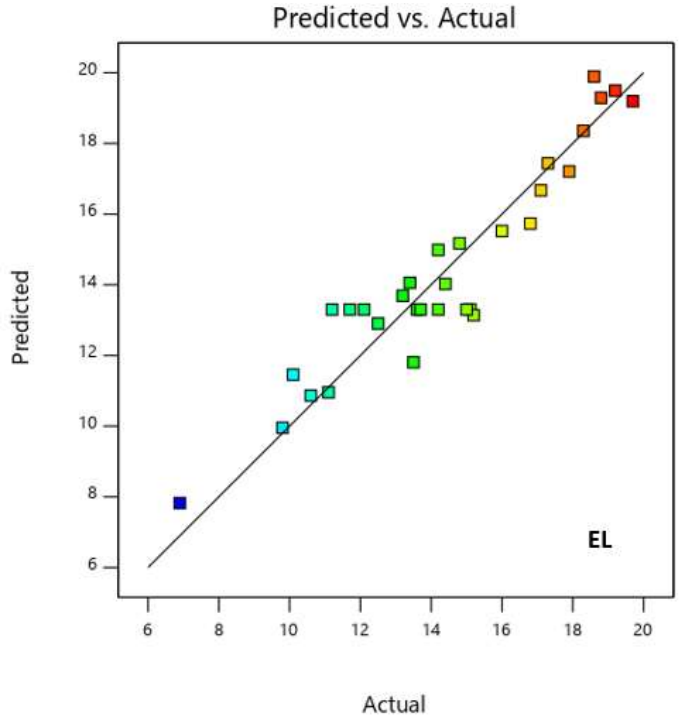

Figure 5.51: Plot of predicted & actual values of percentage elongation

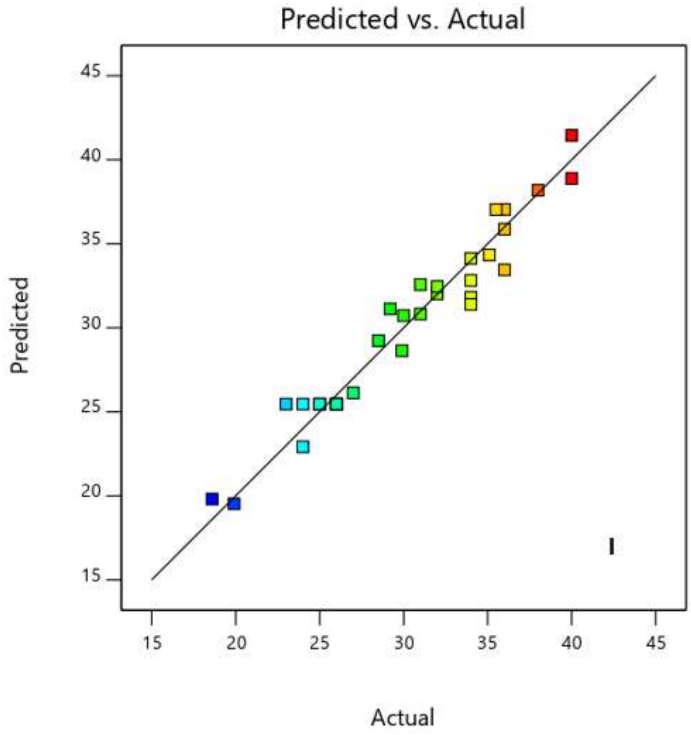

Figure 5.52: Plot of predicted & actual values of impact strength

The equations in coded form, from equation 5.17 to 5.20, have been given:

$$UTS = 172.86 - 2.04\,R + 2.87\,W + 4.54T - 3.04S - 3.31RT + 6.31WT - 2.31\,WS + 4.19TS + 3.13R^2 - 1.37W^2 - 4.87T^2 + 2.88S^2 \quad (5.17)$$

$$YS = 109.65 - 9.33R + 1.92W + 1.000T - 2.58S - 1.62RW - 1.62RT + 1.00RS + 4.25WT + 3.38\,TS + 3.41R^2 + 5.04S^2 \quad (5.18)$$

$$EL = 13.30 + 1.45R - 1.22W + 0.7784T - 0.1781S - 0.7016RW + 1.06\,WT + 0.7534TS + 0.8233R^2 - 0.9704T^2 + 1.55S^2 \quad (5.19)$$

$$I = 25.46 + 0.4092R - 2.16W + 2.97T - 2.10S + 1.23RT - 0.7225RS - 1.01WS + 2.17TS + 1.54R^2 + 2.92W^2 + 1.85S^2 \quad (5.20)$$

5.6.3 THE RELATIVE IMPACT OF DIFFERENT FACTORS ON THE RESPONSES

The coefficients of the equation 5.17 to 5.20 have been presented in Table 5.11. The blank cells of the table indicate the omission of the non-significance of corresponding factors in reduced equations. Based on the table a comparative analysis has been presented:

- The relative effect of the tool tilt angle on response UTS was most prominent among all main effects.
- The relative effect of the tool rotation speed on response YS was most prominent among all main effects. The negative value of the respective regression coefficient indicates that increasing the tool rotation speed would decrease the response YS. For positive values, the influence of the welding speed on response YS was most prominent among all main effects.
- Tool rotation speed emerged as the most significant main effect on response EL.

- The relative effect of the tool tilt angle on the response 'I' was most prominent among all main effects.

Table 5.11: Coefficients of factors in coded form

Factor	UTS	YS	EL	I
Intercept	172.86	110	13.07	25.46
A-R	-2.04	-9.33	1.45	0.4092
B-W	2.87	1.92	-1.22	-2.16
C-T	4.54	1	0.7784	2.97
D-S	-3.04	-2.58	-0.1781	-2.1
AB	-	-1.62	-0.7016	-
AC	-3.31	-1.62	-	1.23
AD	-	1	-	-0.7225
BC	6.31	4.25	1.06	-
BD	-2.31	-	-	-1.01
CD	4.19	3.38	0.7534	2.17
A^2	3.13	3.37	0.8469	1.54
B^2	-1.37	-	-	2.92
C^2	-4.87	-	-0.9468	-
D^2	2.88	5	1.58	1.85

5.6.4 THE RELATIVE IMPACT OF DIFFERENT INTERACTION EFFECTS ON THE RESPONSES

- Welding speed and tool tilt angle interaction effect was observed the most significant for responses UTS, YS and EL.
- The interaction effect of tool tilt angle and pin size is the second most significant for responses UTS and YS.
- The interaction effect of tool tilt angle and tool pin size was observed maximum for impact strength.

5.6.5 THE RELATIVE IMPACT OF DIFFERENT QUADRATIC EFFECTS ON THE RESPONSES

- Tool tilt angle was observed most influential in the estimation of quadratic effects of response UTS.
- Tool RPM was found second most prominent in the estimation of quadratic effects of response UTS.
- Analysis of quadratic effects of the tool pin size revealed its prominence on YS and EL.
- The quadratic effect of tool linear speed on impact strength 'I' was found maximum.
- Tool pin size was observed second most influential in the estimation of quadratic effects of response 'I'.

5.7 OPTIMIZED VALUES OF VARIOUS FACTORS FOR MAXIMUM RESPONSE

After the development of the empirical model, the requirement of finding optimum values of various factors for the desired outcome may arise. The desirable outcome may be maximization, minimization, or target value of the different responses. RSM may be used to find the optimized values based on numerical solutions/graphical solutions. Numerical optimization may be performed by obtaining the optimum values of the input factors for one response at a time. Sometimes it becomes obligatory to find the optimum values of the factors to obtain multiple desired outcomes simultaneously. In the present study, individual responses, as well as all multi-objective optimization, have been performed. Optimization includes a desirability function and its value varies from zero to one.

5.7.1 NUMERICAL OPTIMIZATION FOR ULTIMATE TENSILE STRENGTH

The optimum value of the factors was evaluated by setting the goal of ultimate tensile strength to be maximum, with lower and upper limits at 144 & 300 MPa respectively.

The values of the input factors were initially set within the range of lower and upper levels considered in the present study (Table 5.12). The maximum value of UTS was evaluated to be 225 MPa at the optimal value of factors at 600 tool rpm, 100 mm/min welding speed, 2-degree tilt angle and 5.8 mm side length at the desirability of 0.761.

Table 5.12: The constraints used in optimization

Name	Goal	Lower Limit	Upper Limit	Lower Weight	Upper Weight	Importance
R	is in range	600	1000	1	1	3
W	is in range	30	100	1	1	3
T	is in range	0	2	1	1	3
S	is in range	4.2	5.8	1	1	3
UTS	maximize	144	300	1	1	3
YS	maximize	99	250	1	1	5
EL	maximize	6.9	25	1	1	3
I	maximize	18.6	80	1	1	3

5.7.2 NUMERICAL OPTIMIZATION FOR YIELD STRENGTH

After evaluating optimum conditions above yield, strength maximum value was estimated. The optimum value of the factors was evaluated by setting the goal of yield strength to be maximum, with lower and upper limits at 99 & 250 MPa respectively. The values of the input factors were initially set within the range of lower and upper levels considered in the present study (Table 5.12). The important

criteria for yield strength were set to five unlike that of other factors as the yield strength is generally considered as criteria of failure in the design of various machine parts and applications.

The maximum value of YS was evaluated to be 200 MPa at the optimal value of factors at 600 tool rpm, 100 mm/min welding speed, 2-degree tilt angle and 5.8 mm side length at the desirability of 0.998.

5.7.3 NUMERICAL OPTIMIZATION FOR PERCENTAGE ELONGATION

In this section, optimum conditions for maximum percentage elongation have been estimated. The optimum values of the factors were evaluated by setting the goal of percentage elongation to be maximum, with lower and upper limits at 6.9 & 25 percent respectively. The values of the input factors were initially set within the range of lower and upper levels considered in the present study (Table 5.12). The maximum value of EL was evaluated to be 25 percent at the optimal value of factors at 1000 tool rpm, 60 mm/min welding speed, 1.75-degree tilt angle and 4.6 mm side length at the desirability of 1.0.

5.7.4 NUMERICAL OPTIMIZATION FOR IMPACT STRENGTH

The optimum value of the factors was evaluated by setting the goal of impact strength to be maximum, with lower and upper limits at 18.6 & 80 J respectively.

The values of the input factors were initially set within the range of lower and upper levels considered in the present study (Table 5.12). The maximum value of impact strength was evaluated to be 63.3 J at the optimal value of factors at 1000 tool rpm, 30 mm/min welding speed, 1.8-degree tilt angle and 4.2 mm side length at the desirability of 0.55.

5.7.5 MULTI-OBJECTIVE OPTIMIZATION

In previous sections, optimum values of factors were estimated for one response at an instance. In Multi-objective optimization, each factor level is obtained in a way that every response fulfills desired outcome condition simultaneously (maximum, minimum, target value).

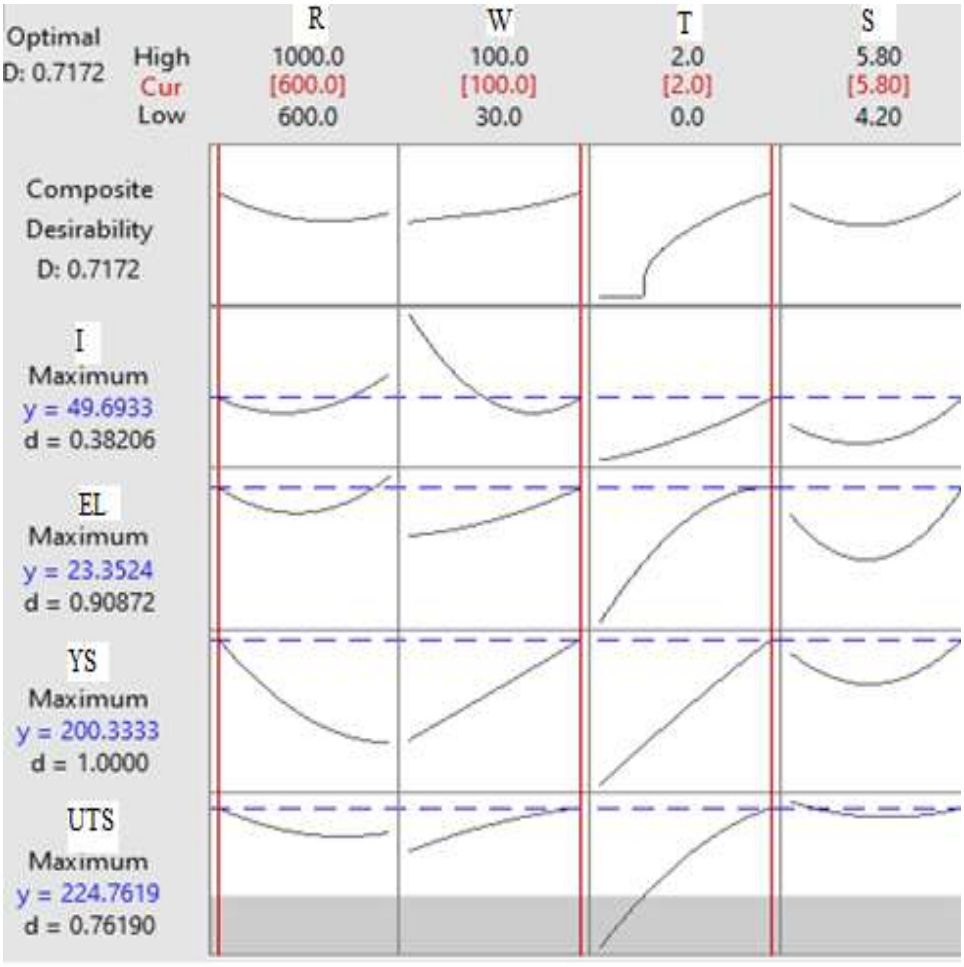

Figure 5.53: Multi-objective optimization plots

The plots indicating the multi-objective optimization have been presented in Figure 5.53. In the plots, the x-axes indicate the factor value and y-axes indicate the responses. The red line in each plot indicates the value of input factors corresponding to maximum response. The blue line in each plot indicates the

maximum value of each response while fulfilling the optimization criteria of all responses simultaneously.

The constraints imposed on the input factors and criteria for various responses have been presented in Table 5.12. Optimal values according to multi-objective analysis for ultimate yield strength, yield strength and percentage elongation and impact strength are 224.7 MPa, 200.2 MPa, and 23 percent and 49.69 J respectively at 600 rpm, 100mm/min traverse speed, 2-degree tilt angle and 5.8 mm square pin size at desirability 0.717. The results are also tabulated in Table 5.13.

Table 5.13: Multi-objective optimization results

R (RPM)	W (mm/min)	T (degrees)	S (mm)	UTS (MPa)	YS (MPa)	EL (%)	I (Joules)	Desirability
600	99.8	2	5.8	225	200	23	49.69	0.717
Confirmatory runs				227.7	199.3	22.7	52	

The confirmatory runs were performed to verify the multi- optimization results. The experiments were performed using dissimilar alloy at 600 rpm, 99.8 welding speed, 2-degrees tilt angle with a tool pin of size 5.8 mm. After FSW at specified input values responses were measured and summarized in Table 5.13. The values obtained from confirmatory runs were within a close tolerance of optimization results.

5.8 MICROHARDNESS ANALYSIS

The micro hardness of the transverse section was measured as discussed in the previous chapter. The graph between the distance from the center of weld on the X-axis and microhardness on the Y-axis has been presented in Figure 5.54 and 5.55.

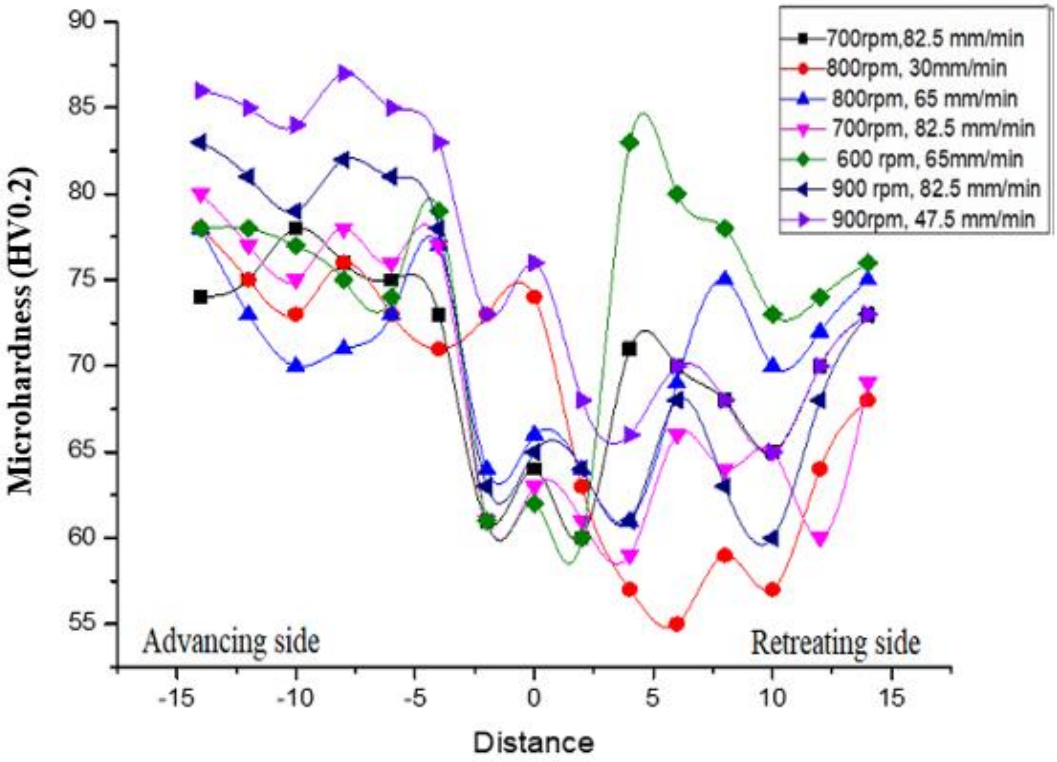

Figure 5.54: Microhardness profile

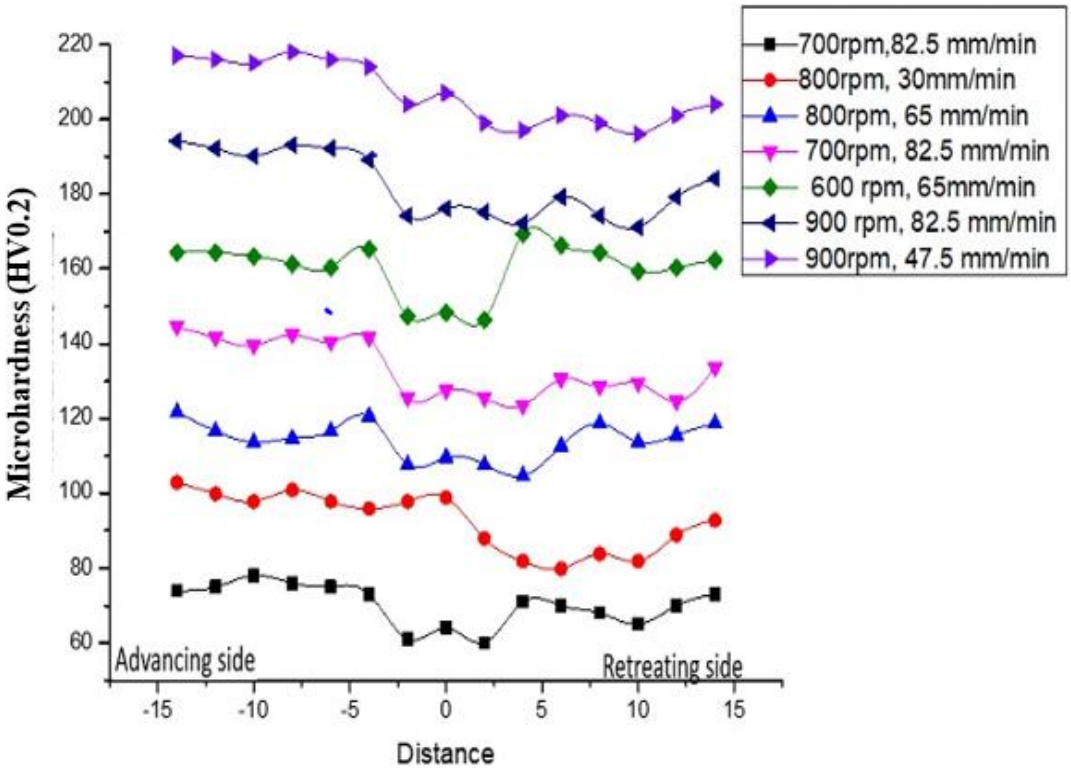

Figure 5.55: Offset Microhardness profile

The graphs were plotted with the help of "Origin" software without and with offset. Minimum hardness value was observed on the retreating side in TMAZ/HAZ. The fracture of the tensile specimen occurred in the least hardness zone. Approximately, a W- shaped curve pattern was observed in the micro hardness curve.

5.9 RESIDUAL STRESS ANALYSIS

In the previous chapter, the residual stress measurement methodology has been depicted. Some samples with corresponding process parameters have been presented in Table 5.14. Residual stresses in the nugget zone of these samples have been presented in Table 5.15. The residual stresses in the advancing and retreating side of the samples have been presented in Table 5.16.

Table 5.14: FSW process parameters for different samples

Sample no.	Tool RPM	Tool speed(mm/min)	Tilt angle(°)	Pin size (mm)
R4	700	82.5	0.5	5.4
R5	1000	65	1	5
R15	800	65	2	5
R18	700	82.5	0.5	4.6
R30	700	82.5	1.5	5.4

Table 5.15: Residual stresses of the nugget zone

Sample no.	Normal residual stress & Std. Dev. (MPa)	Tangential residual stress & Std. Dev. (MPa)	FWHM (Degree)
R4	-52 (Comp.) & 8	7 & 4	2.61
R5	-85 (Comp.) & 12	-22 & 9	2.75
R15	252 &133	-28 & 112	3.44
R18	Zero & 29	-20 & 24	3.09
R30	-20 (Comp.) & 10	3 & 6	2.31

Table 5.16: Residual stresses of advancing and retreating side

Sample no.	AS			RS		
	Normal residual stresses & std. dev. (MPa)	Tangential residual stress & std. dev. (MPa)	FWHM (Degree)	Normal residual stresses & std. dev. (MPa)	Tangential residual stress & std. dev. (MPa)	FWHM (Degree)
R4	-118 & 13	-9 & 12	2.97	-27 & 4	-2 & 2	2.69
R5	24 & 28	-2 & 39	2.70	23 & 27	-21 & 33	2.52
R15	-22 & 42	6 & 20	2.60	-39 & 40	-14 & 39	2.66
R18	-176 & 226	28 & 205	2.53	11 & 80	-25 & 70	2.60
R30	-233 & 46	28 & 26	2.76	61 & 49	-40 & 61	4.42

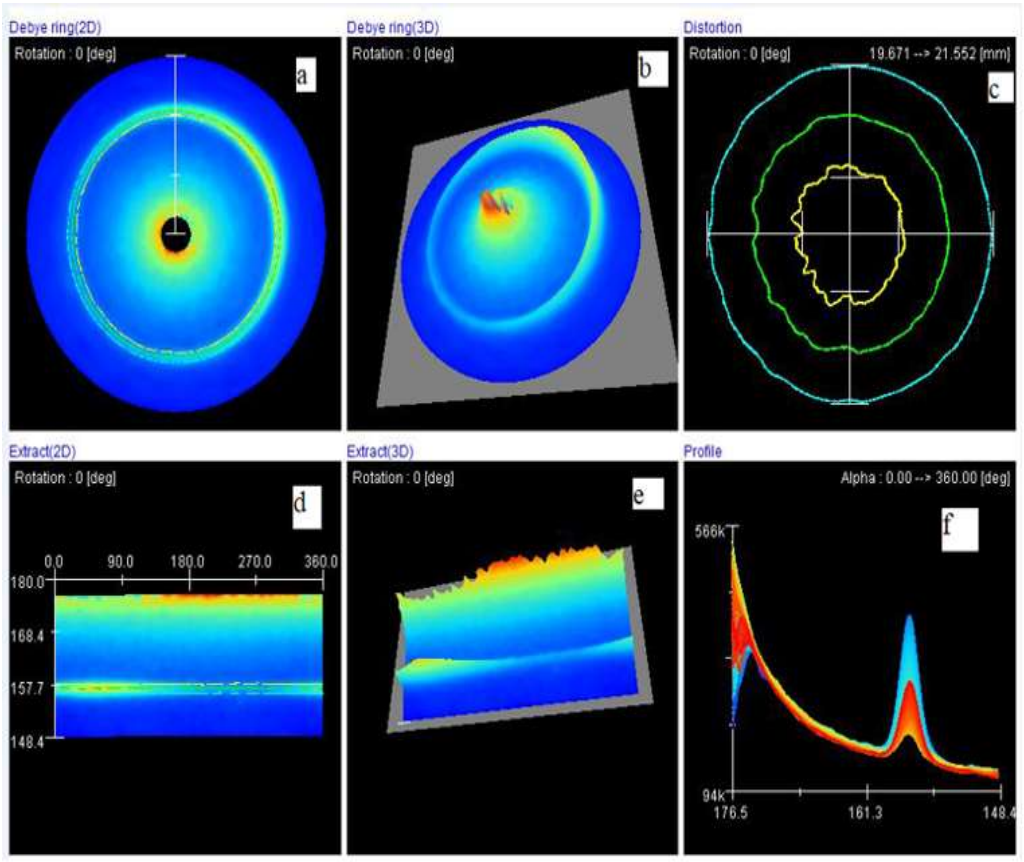

Figure 5.56: Debey ring at 700 rpm & 82.5 mm/min for sample R30 in NZ

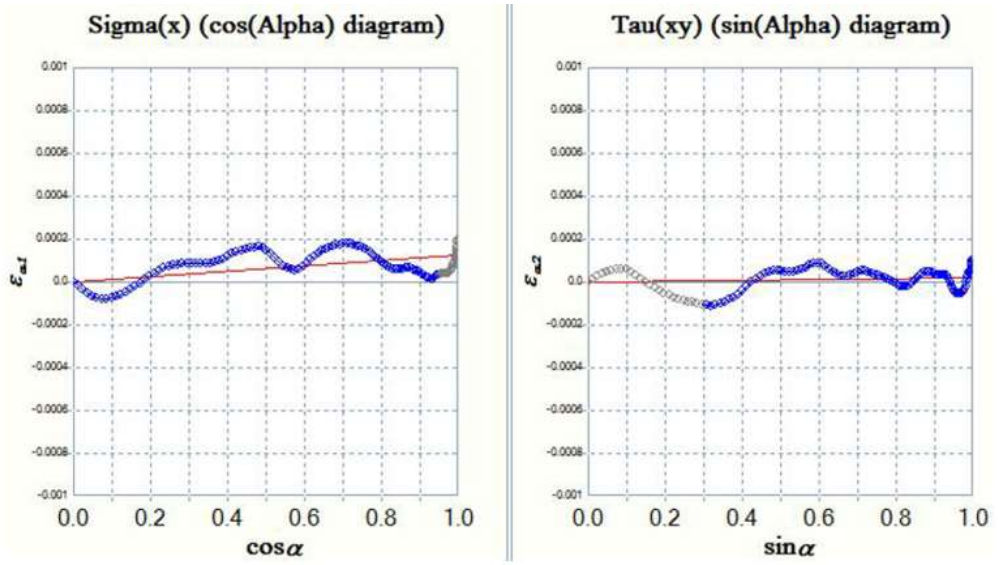

Figure 5.57:Strain values at 700 rpm & 82.5 mm/min for sample R30 against cos & sin of alpha in NZ

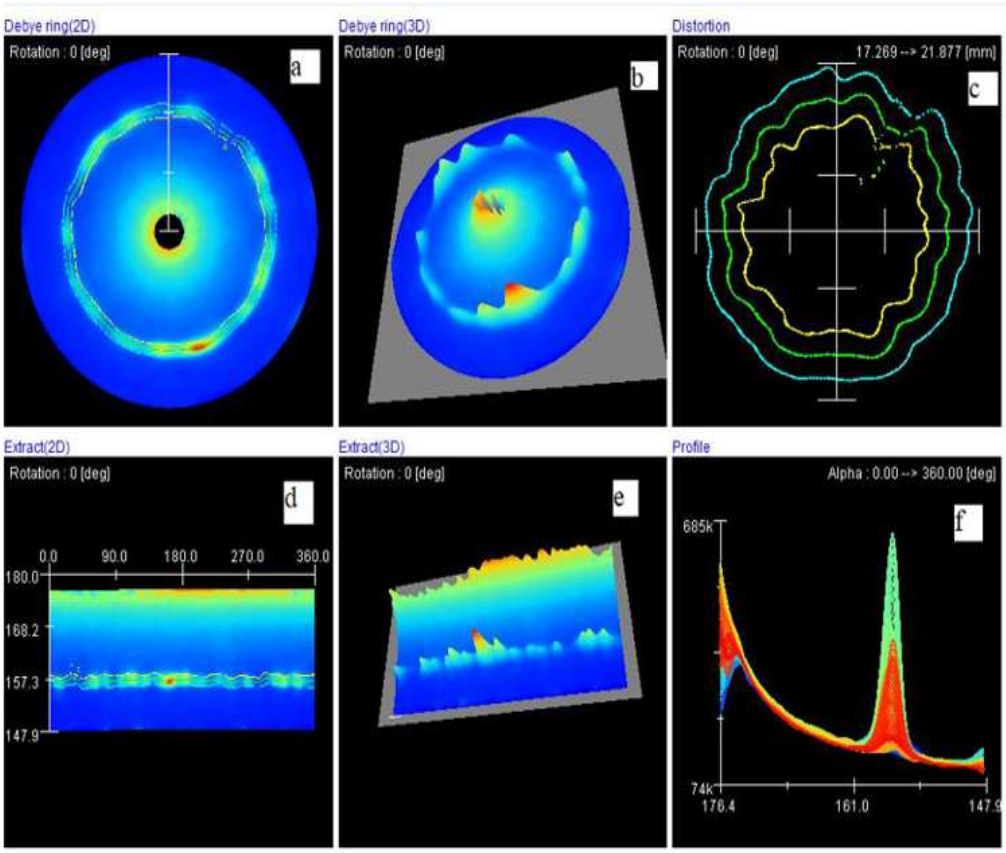

Figure 5.58: Debye ring at 700 rpm & 82.5 mm/min for sample R 18 on the retreating side

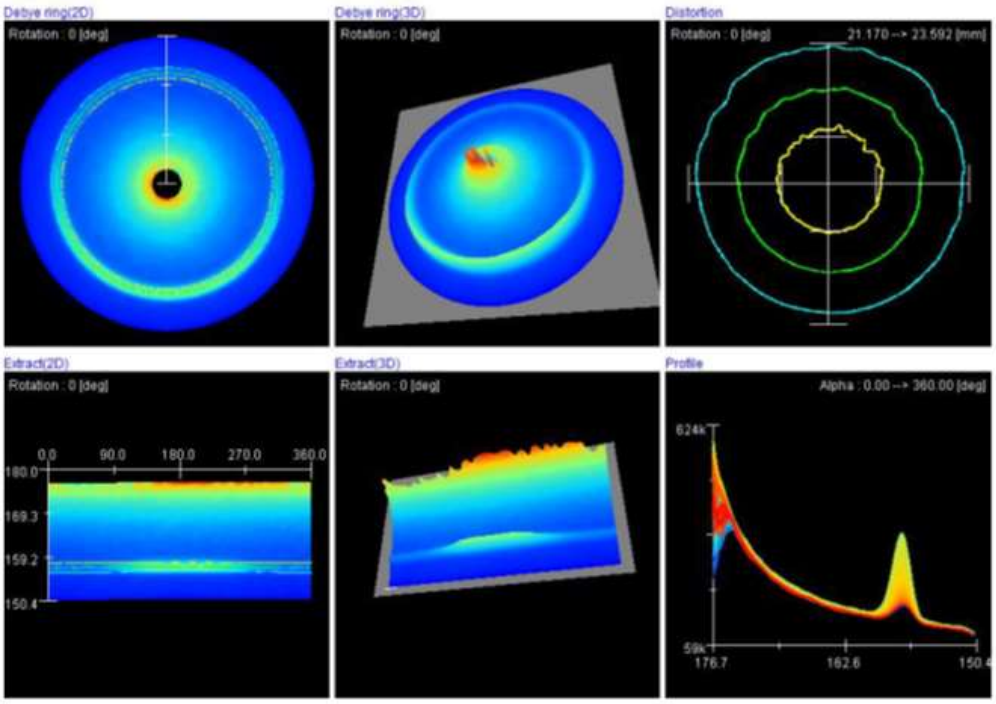

Figure 5.59: Debye ring at 700 rpm & 82.5 mm/min for sample R4 in the nugget NZ

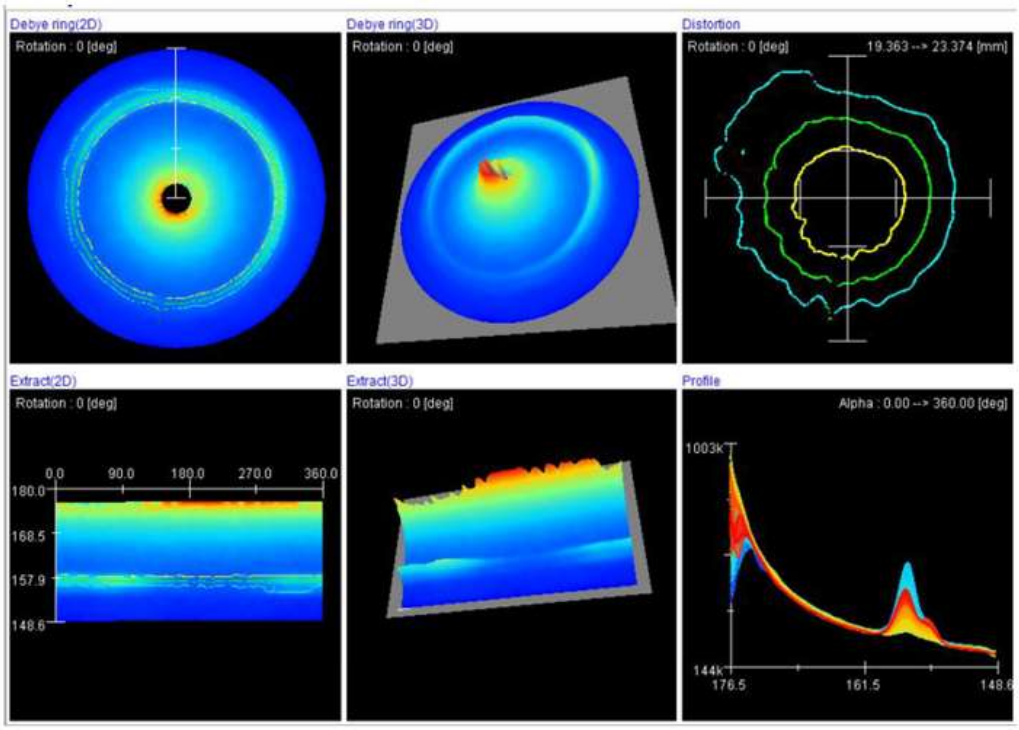

Figure 5.60: Debye ring at 700 rpm & 82.5 mm/min for sample R18 in NZ

Figure 5.55 indicates the Debye ring and other details of sample R30 for the nugget zone and explained subsequently. The graphs presented in Figure 5.55 were generated from the machine set up, micro X360 used for measuring residual stresses by cos (α) method. Figure 5.55 (a) and (b) indicate 2-Dimensional (2D) and 3-Dimensional (3D) Debye ring respectively. The 5.55 (d) represents the extract of the Debye ring, i.e., the 2D ring in 5.55 (a) has been linearly opened up (extracted) with diffraction angle 2θ on the left-hand side and total angle of the ring on top of the diagram from zero to 360 degrees. Also, two different lines (intensity profiles) have been indicated at 157.6 degrees and another at 176.5 degrees in 5.55(d). The value 176.5 has been evaluated from 5.55(f), indicates the profile diagram with 2θ on the x-axis and intensity (arbitrary units) on the y-axis. Image 5.55 (e) indicates the extracted image of 5.55(b), 3-D Debye ring. The two lines in 2-D extracted image may be visualized as a consequence of profiles in different colors in the 3-D extracted image. The profile image 5.55 (f) may be visualized as the 2-D profile of the protruded 3-D extracted image. The different colors of profile image 5.55 (f) are indicative of variation of protrusion height at the different positions in the longitudinal direction of 3-D extract 5.55 (e). The profile peaks in image 5.55 (f) are at two different angular positions (2 theta), i.e., at 157.6 and 176.5 degrees. Angle 157.6 degrees may be evaluated by, as indicated in image 5.55 (d). Image 5.55 (c) indicates the distortion of the Debye ring circle and has been indicated by distorted circles. Debye ring visual inspection may reveal the grain size coarsening. Figure 5.57 indicates the plots of εα1 and cos (α), and εα2 and sin (α). The slopes of the plots give the value of normal residual stress (-20 MPa) and tangential residual stress (3 MPa).

Figure 5.58 illustrates the grain coarsening as a variation of intensity in the 3-dimensional Debye ring. Grain coarsening is indicated by the large variation in the intensity along the circumference of the Debye ring, as indicated by Figure 5.58 (b). The same may be visualized by more variation in different colors at 2(theta) value of 157.3 (peak position) in profile diagram 5.58 (f). Also, it may be elucidated from Figure 5.58 (e), indicating the 3-Dimensional extract of the Debye ring. FWHM values were also made from the profile diagram and interrelated to residual stresses.

The grain size in the nugget zone is small and an increase in its size may be observed on the advancing and retreating side. The visual and analytical details of the Debye ring may reveal other details besides the residual stresses. The Debye ring is also utilized to understand the grain size relationship with full width half maximum. As the grain size in the advancing and retreating side is more than that in the nugget zone, the full width half maximum value of the former is less than that of the latter. The grain size in the nugget zone is small and an increase in its size may be observed on the advancing and retreating side. The visual and analytical details of the Debye ring may reveal other details besides the residual stresses. The Debye ring may also be utilized to understand the grain size relationship with a full width half maximum. As the grain size in the advancing and retreating side is more than that in the nugget zone, the full width half maximum value of the former is less than that of the latter. Further, for smaller grain size the Debye ring is thicker and consequently, the peak generated is also thicker in comparison to that of larger grain size.

From Table 5.14, 5.15 and, 5.16, and Figure 5.59 and 5.60, and comparing R4 and R18 it has been observed that at for same process parameters (tool RPM, traverse speed and tilt angle), FSW with higher pin size results in lower value of FWHM, and hence more value of compressive stress in magnitude. Further, on the

advancing and retreating side the value of the FWHM is more with the FSW joint with a higher pin size. Fixing process parameters (tool RPM, traverse speed and pin size) at the constant value for R4 and R30 (Figure 5.56 and 5.59), the higher value of tool tilt angle results in lower FWHM and higher value of residual stress in the nugget zone.

5.10 XRD ANALYSIS AND MICROSTRUCTURE

In the previous section, the residual stress measurement and interpretation were presented. In this section, the X-ray Diffractometer and microstructure analysis (optical and SEM) have been manifested. The XRD for the base material has been presented in Figure 5.60. The base material has 3 peaks and the corresponding position in terms of 2 (theta) for AA 5083-O are 38.4881, 44.6668 and 64.9242 degrees and corresponding FWHM are 0.192, 0.288 and 0.288 degrees. The peak positions for AA-6082-T651 are 38.5779, 44.8337 and 65.1725 degrees and corresponding FWHM are 0.192, 0.144 and 0.288 degrees. Figure 5.60 to Figure 5.75 presents the XRD graphs and SEM microstructure graphs for different samples (nugget zone).

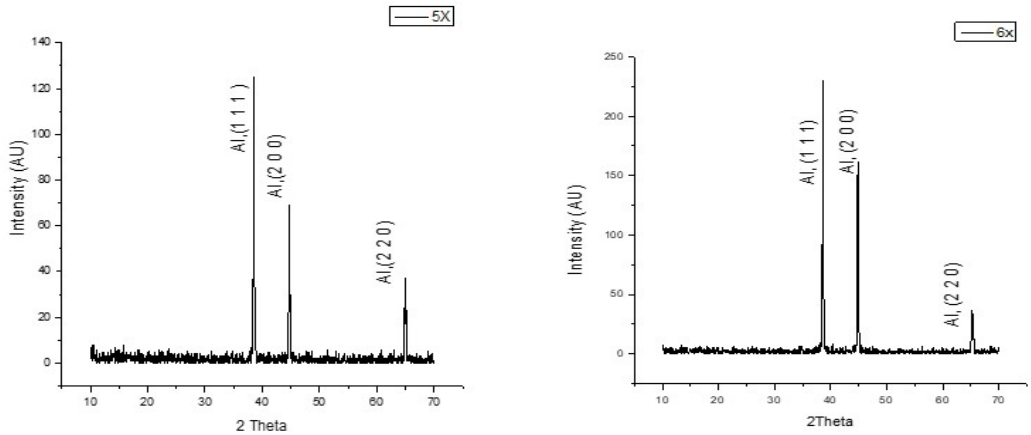

Figure 5.61: XRD plots of base material 5083-O and 6082-T651

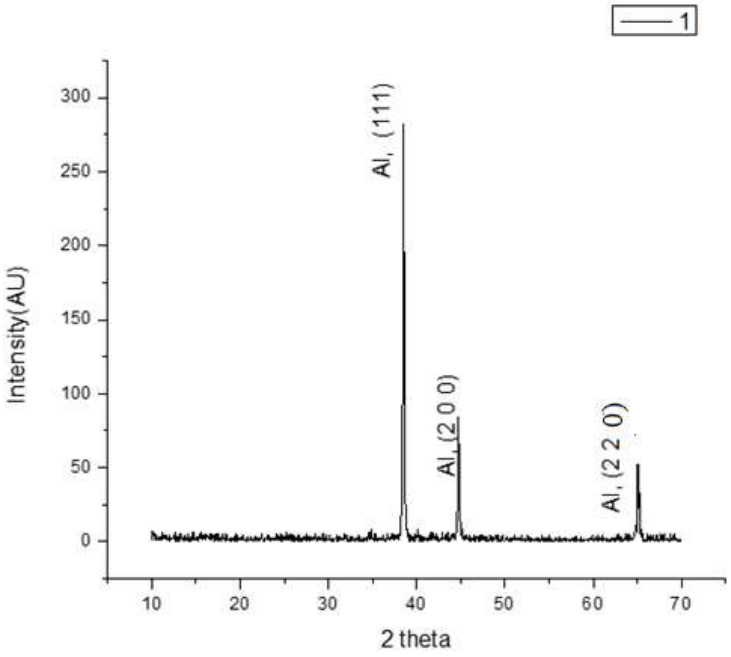

Figure 5.62: XRD plot for the sample at 600 rpm, 65 mm/min, R1

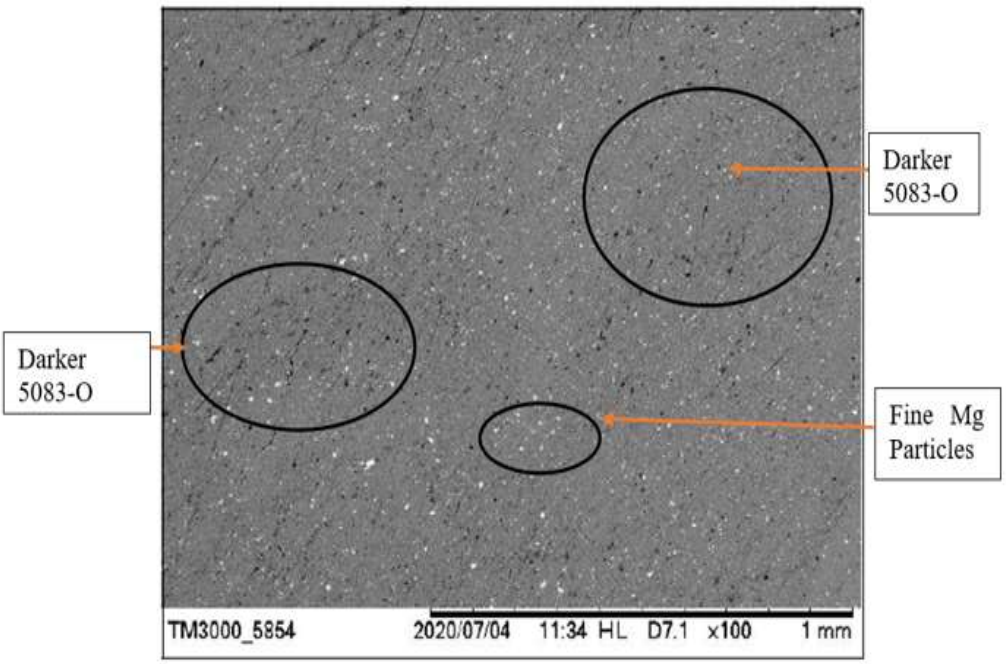

Figure 5.63: SEM analysis at 600 rpm, 65 mm/min, R1 at 100X

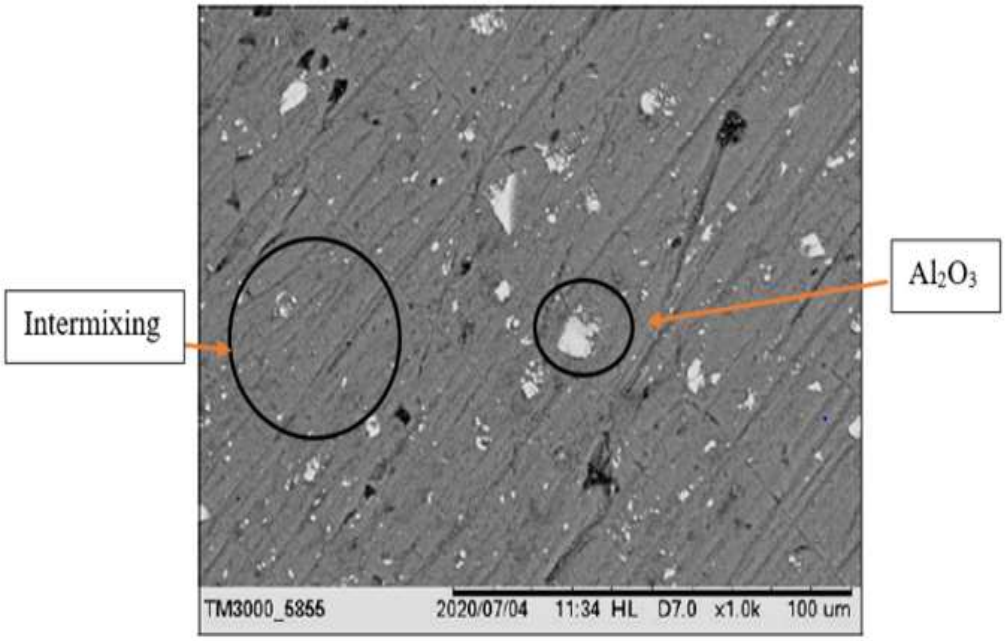

Figure 5.64: SEM analysis at 600 rpm, 65 mm/min, R1 at 1000 X

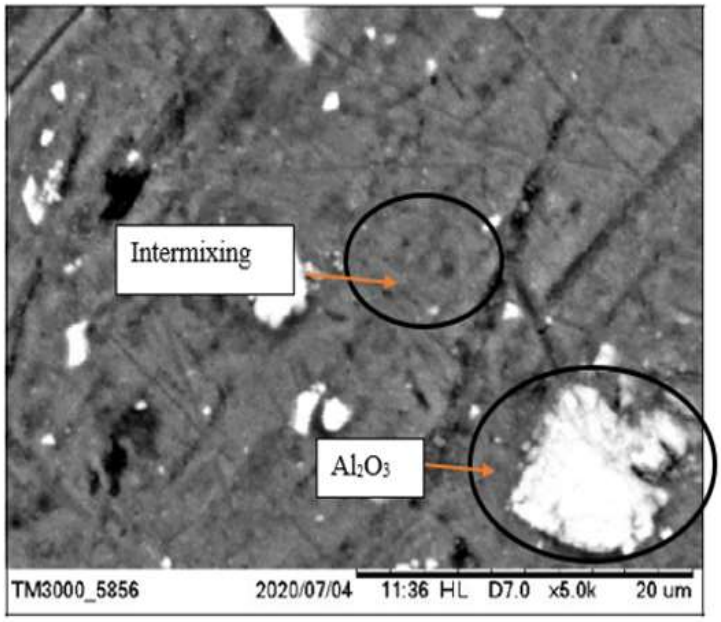

Figure 5.65: SEM analysis at 600 rpm, 65 mm/min, R1 at 5000 X

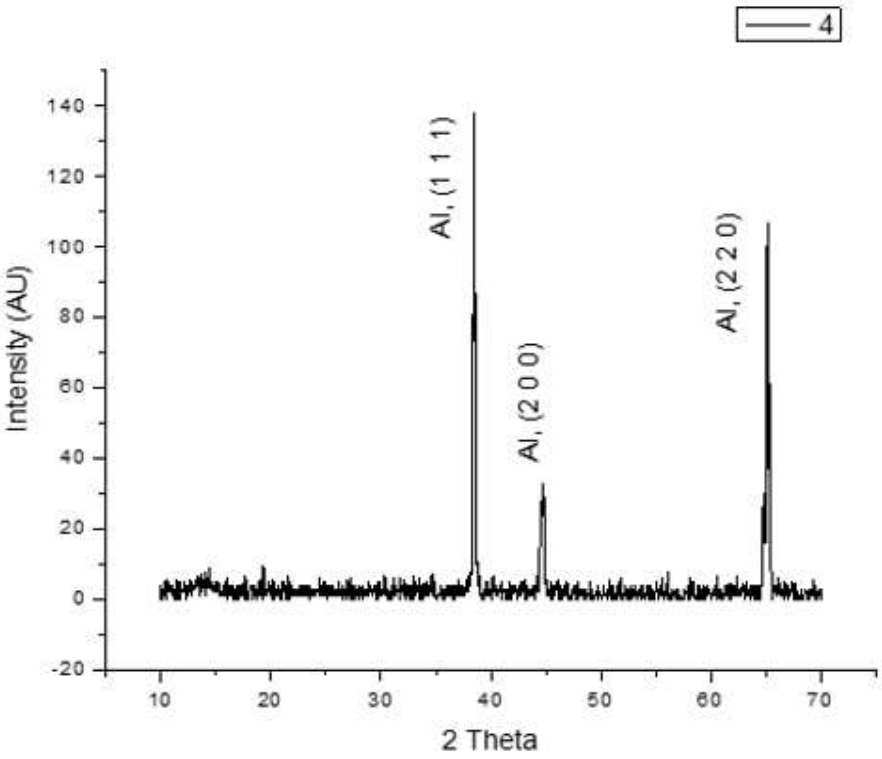

Figure 5.66: The XRD plots at 700rpm,82.5 mm/min, R4

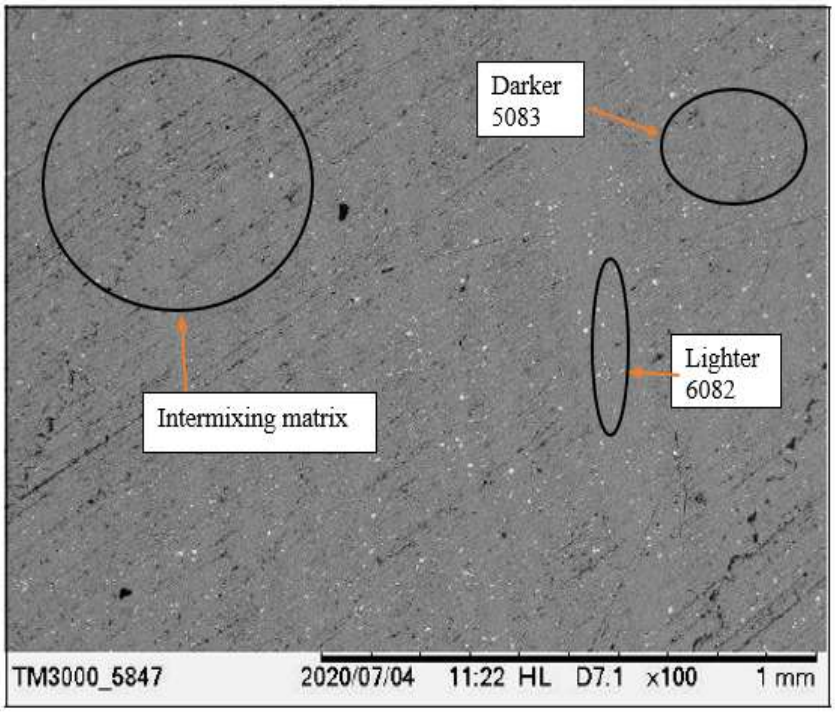

Figure 5.67: SEM analysis at 700rpm,82.5 mm/min, R4 at 100X

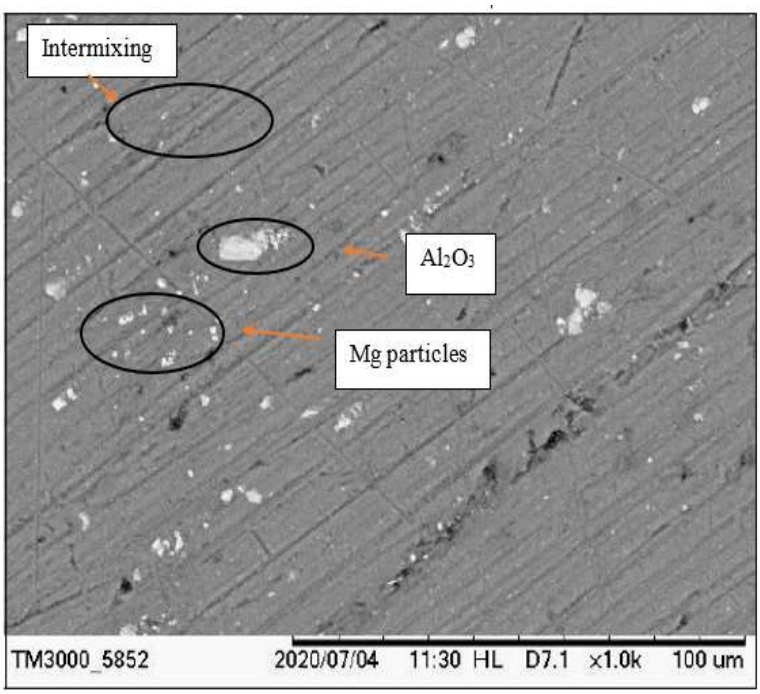

Figure 5.68: SEM analysis at 700rpm,82.5 mm/min, R4 at 1000X

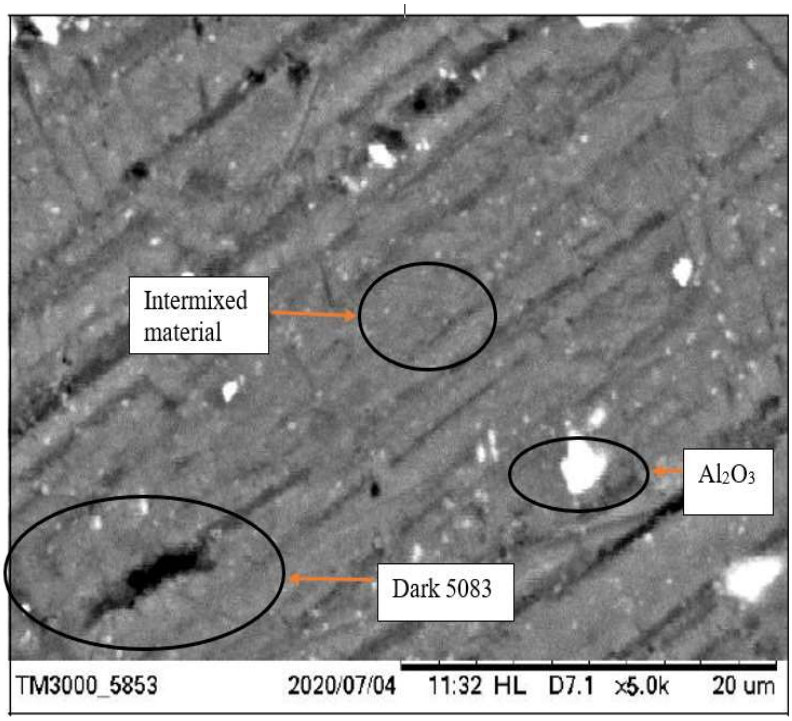

Figure 5.69: SEM analysis at 700rpm,82.5 mm/min, R4 at 5000X

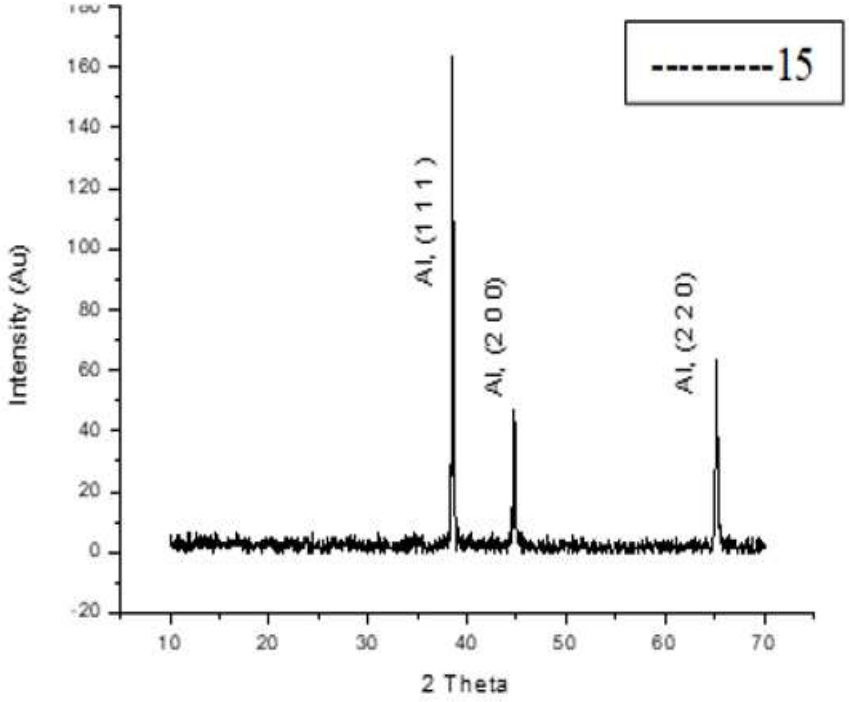

Figure 5.70: The XRD plots at 800 rpm, 65 mm/min, R15

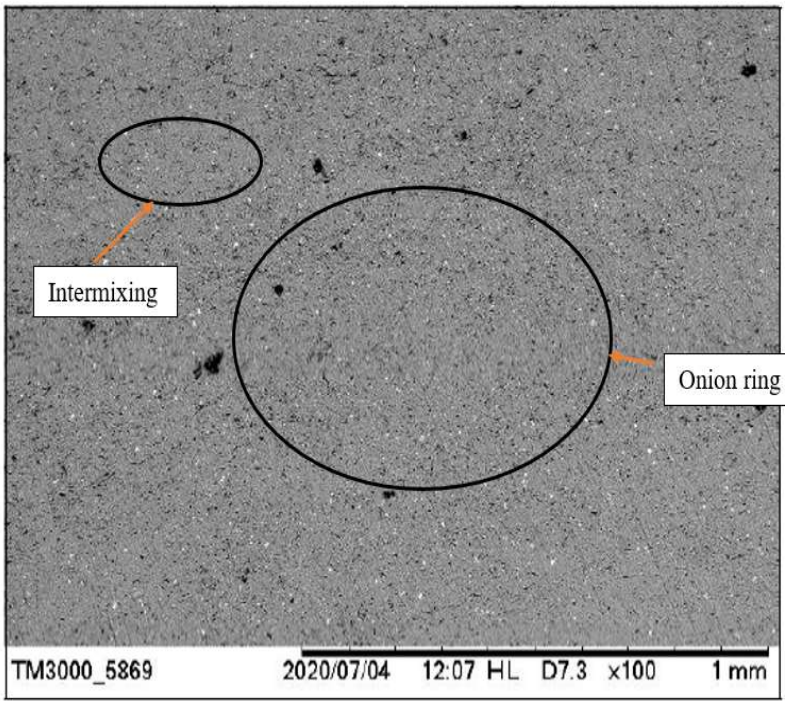

Figure 5.71: SEM analysis at 800 rpm, 65 mm/min, R15 at 100X

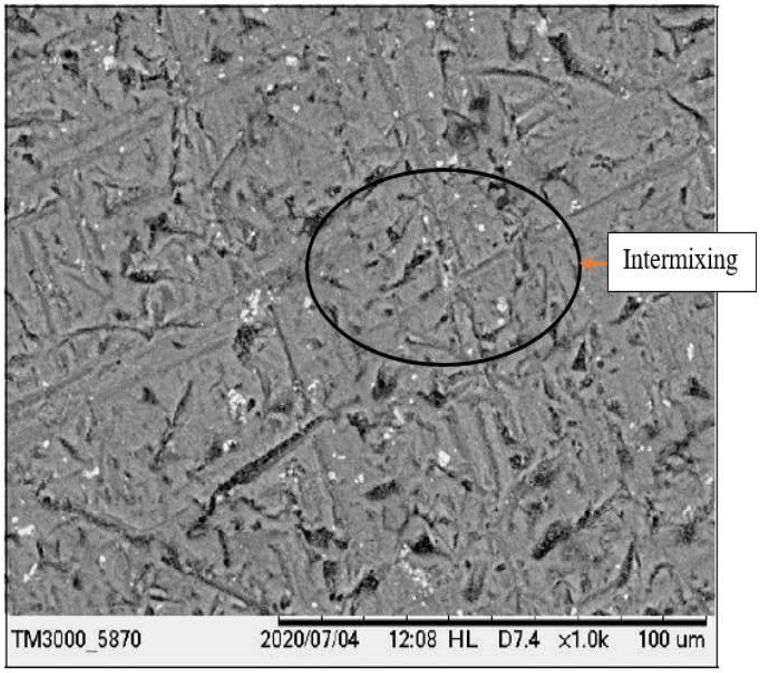

Figure 5.72: SEM analysis at 800 rpm, 65 mm/min, R15 at 1000X

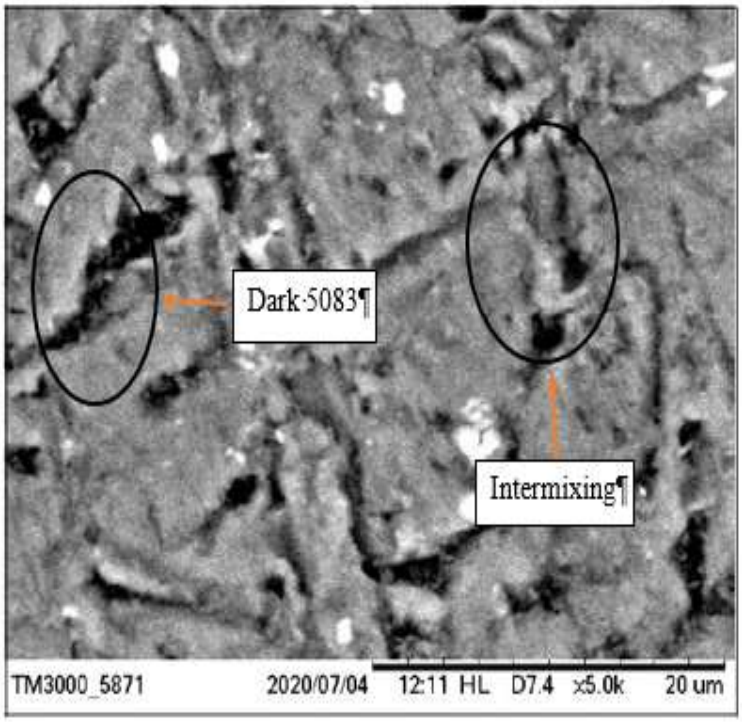

Figure 5.73: SEM analysis at 800 rpm, 65 mm/min, R15 at 5000X

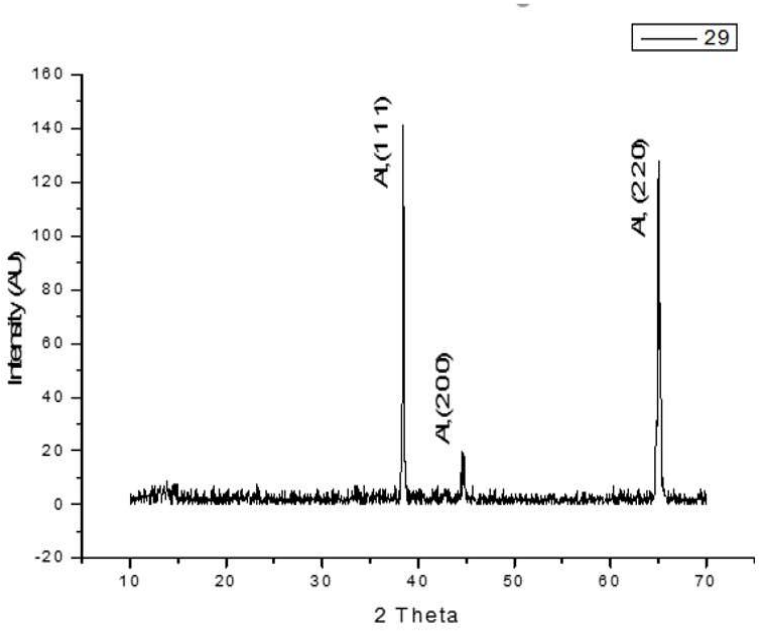

Figure 5.74: The XRD plot at 800 rpm, 30 mm/min, R29

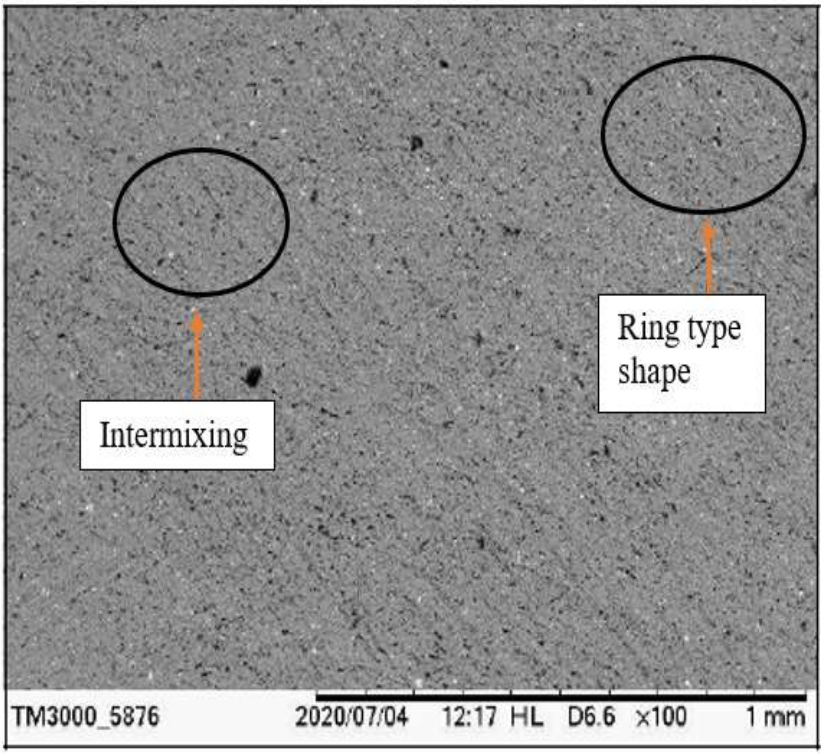

Figure 5.75: SEM analysis at 800 rpm, 30 mm/min, R29 at 100X

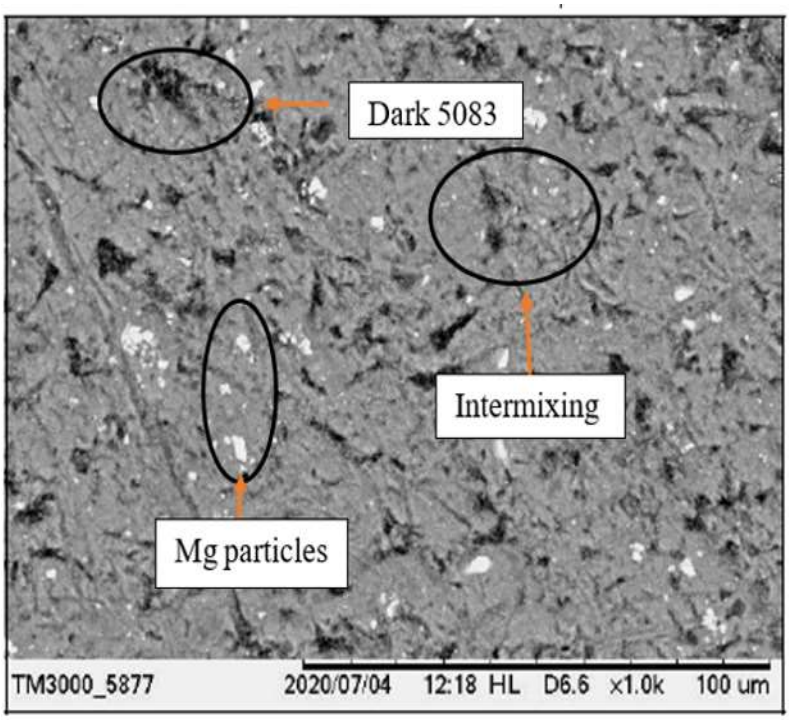

Figure 5.76: SEM analysis at 800 rpm, 30 mm/min, R29 at 1000X

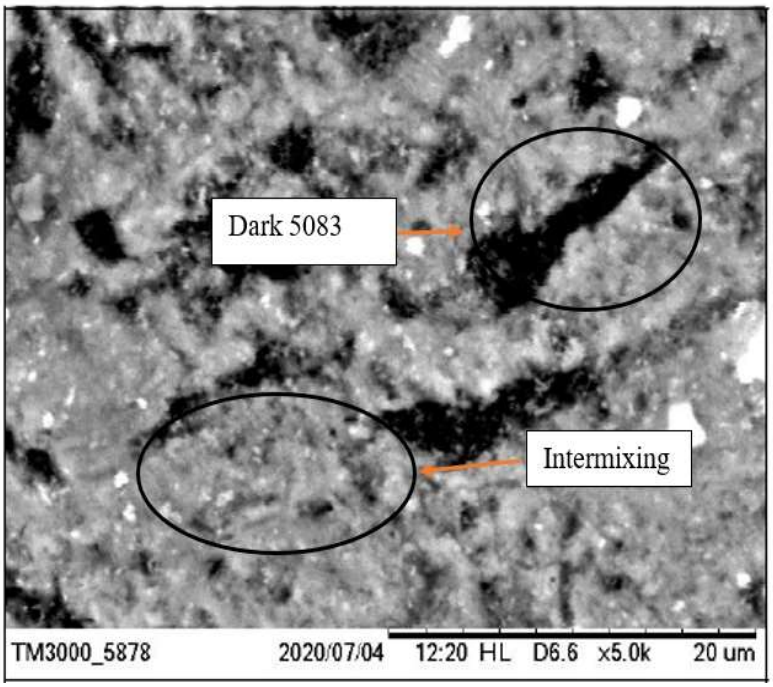

Figure 5.77: SEM analysis at 800 rpm, 30 mm/min, R29 at 5000X

`

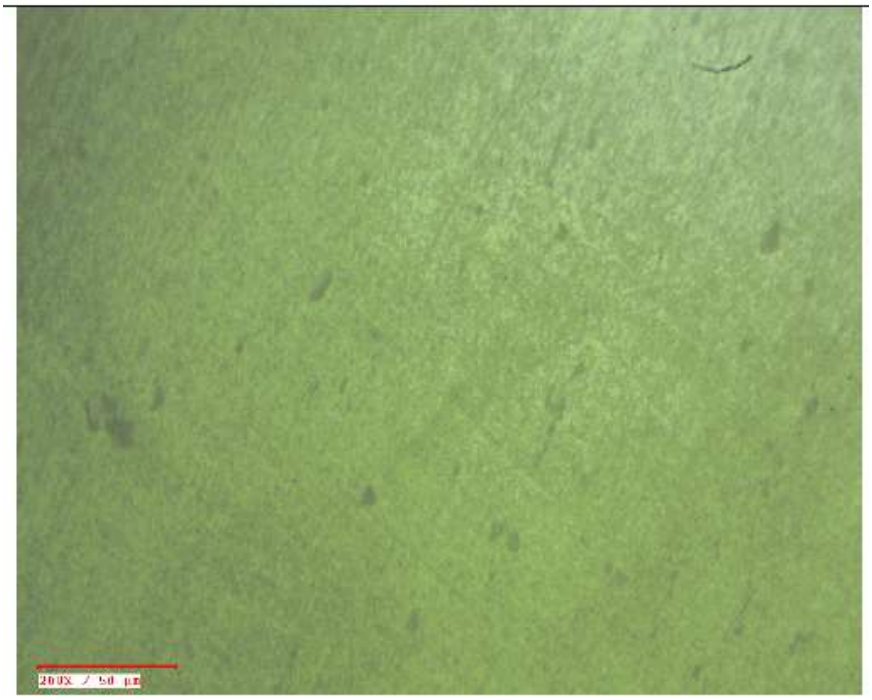

Figure 5.78: Optical microscope image at 600 rpm, 65 mm/min, R1, AS at 200X

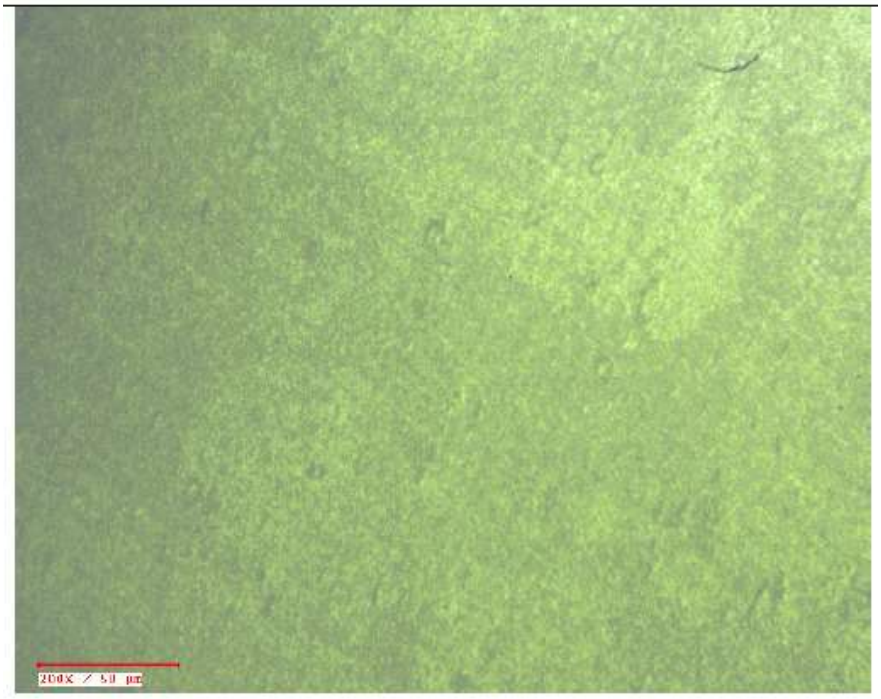

Figure 5.79:Optical microscope image at 600 rpm, 65 mm/min, R1, RS at 200X

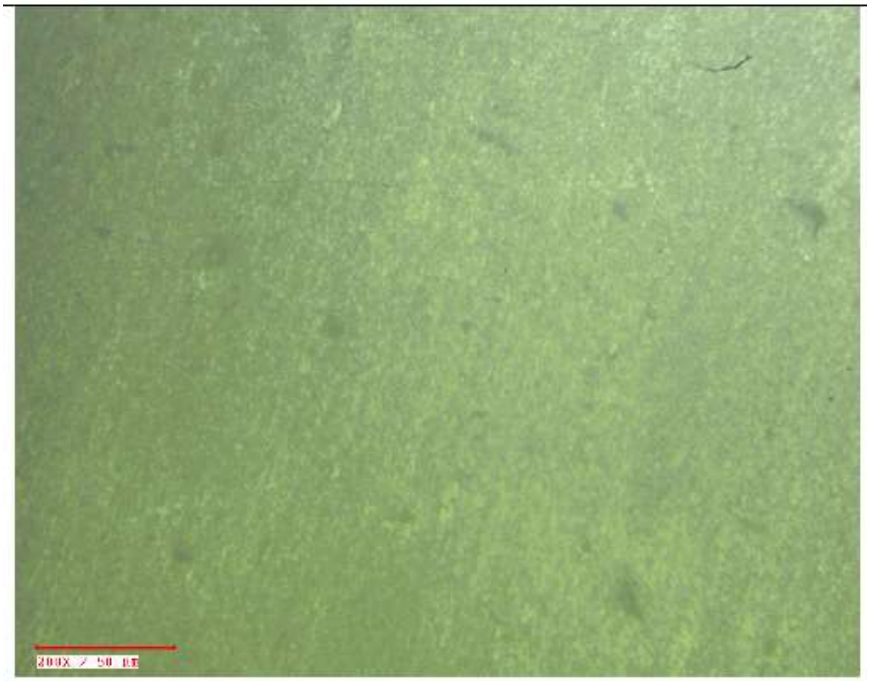

Figure 5.80: Optical microscope image at 700rpm, 82.5 mm/min, R4, AS, at 200X

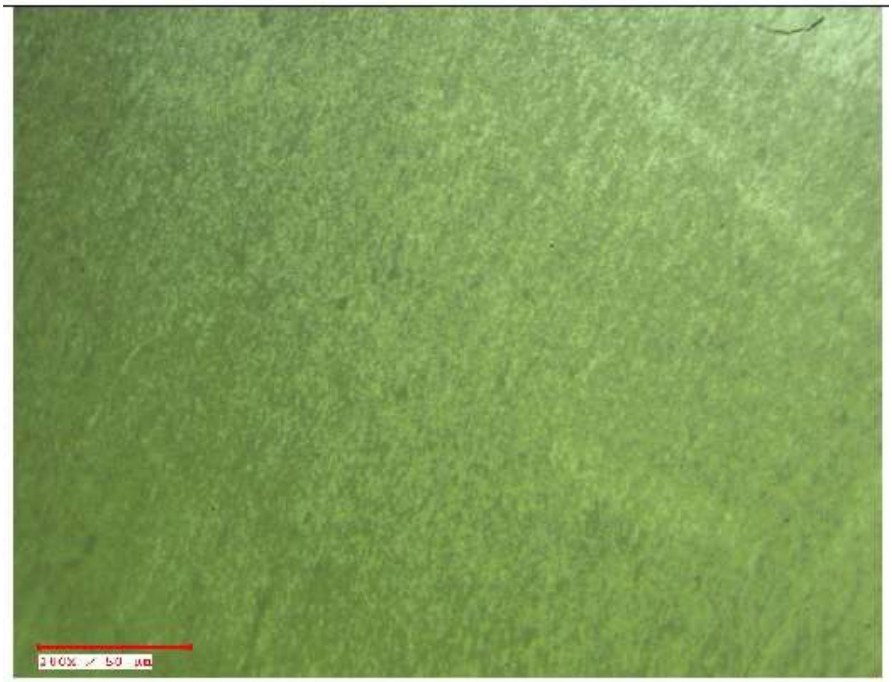

Figure 5.81: Optical microscope image at 700rpm,82.5 mm/min, R4, RS, at 200X

Figure 5.82: Optical microscope image at 800rpm, 65 mm/min, R15, AS, at 200X

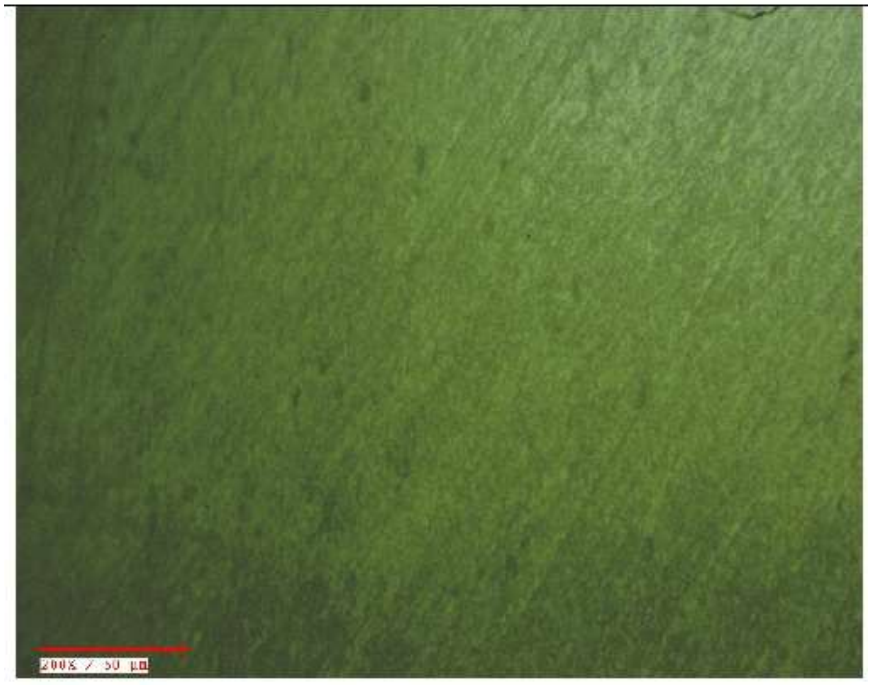

Figure 5.83: Optical microscope image at 800rpm, 65 mm/min, R15, RS, at 200X

The SEM graphs are presented at different values of magnifications. The SEM graphs are at a magnification of 100X, 1000X and 5000 X. XRD graphs are at different values of 2(theta) varying from ten to seventy degrees and had three peaks with different Miller indices. Two different software Origin and Xpert high score were used to complete the XRD analysis. Three peaks were generated by XRD analysis. The high intensity of the XRD peaks indicates a high level of crystallinity.

In SEM images (nugget zone) generated the 6082-T651 indicated are lighter area while 5083-O is indicated by the darker area. Figure 5.62 indicates the SEM image of specimen R1 at magnification 100X with maximum yield strength. The SEM image has proper intermixing, with elongated grains. The white patch in Figure 5.64 indicates the presence of Al_2O_3. Figure 5.70 indicates the onion ring of sample R 15 (maximum percentage elongation) in the SEM image at a magnification of 100X. Other images of R15 indicate the equiaxed grains in the nugget zone. In SEM image of the nugget zone of R29 (maximum impact strength) has been presented from Figure 5.74 to 5.76. The respective XRD plot has been presented in Figure 5.73.

The optical microscopy images of the specimen R1, R4 and R15 (AS and RS) have been presented in Figure 5.77 to 5.82. The AS and RS of the joint include the AA 6082-T651 and AA 5083-O respectively. All the images have been presented at 200X magnification.

CHAPTER 6: CONCLUSIONS AND FUTURE WORK

In the present chapter, precise conclusions have been presented. The second section of this chapter presents the future work that may be further extended from the findings of this study.

6.1 CONCLUSIONS

- In this work, experimentation was performed as per rotatable central composite design to study and analyse an integrated effect of tool rotation speed, tool traverse speed, tool tilt angle and square-shaped pin size on the ultimate tensile strength, yield strength, percentage elongation and impact strength of friction Stir welding of dissimilar AA 5083-O and AA 6082-T651.
- Mathematical models were established for ultimate tensile strength, yield strength, percentage elongation and impact strength. Analysis of the models was performed using RSM and ANOVA.
- In this work, the square shaped pin size was varied from 4.2 mm to 5.8 mm. It was observed that maximum value of all the responses was obtained at pin size of 5.8 mm.
- Ultimate tensile strength is most prominently affected by tool tilt angle and welding speed.
- The optimal value of UTS is 224.5 MPa at 600 rpm, 100 mm/min welding speed, 2-degree tilt angle and 5.8 mm side length at the desirability of 0.761.
- Yield strength is prominently influenced by linear velocity and tilt angle.

- The optimal value of YS is 200.18 MPa at 600 rpm, 100 mm/min welding speed, 2-degree tilt angle and 5.8 mm side length at the desirability of 0.998.
- Percentage Elongation is most influenced by linear velocity and tool tilt angle.
- The optimal value of percentage elongation is 25.8 percent at 1000 rpm, 60 mm/min, 1.75-degree tool tilt angle and 4.6 mm side length at the desirability of one.
- Impact strength is most significantly affected by tool tilt angle and tool rpm.
- The optimal value of impact strength is 63.3 J at 1000 rpm, 30 mm/min, 1.8-degree tool tilt angle and 4.2 mm side length at the desirability of 0.548.
- Optimal values according to multi-objective analysis for ultimate yield strength, yield strength, percentage elongation and impact strength are 224.7 MPa, 200.2 MPa, and 23 percent and 49.69 J respectively at 600 rpm, 100mm/min traverse speed, 2-degree tilt angle and 5.8 mm square pin size at desirability 0.717.
- XRD analysis was performed and three phases of aluminum are observed in the study at 2 theta values (70 degrees).
- Vickers hardness is observed minimum at the retreating side and confirmed by fracture positions of tensile test samples.
- SEM and optical microscopy were utilized to analyze the microstructure of the test specimen.
- The microstructure profile of light optical microscope and SEM analysis has justified the results for maximum valued response samples.
- Residual stresses are measured using the cos (α) method.

- Minimum values of Full-Width Half Maximum correspond to the compressive residual stress and provide good fatigue strength and vice versa.

6.2 SCOPE FOR THE FUTURE WORK

- The high rigidity FSW machine may be used with a higher range of tool rotational velocity and linear speed.
- Underwater welding of dissimilar AA 5083-O and AA 6082-T651 may be performed with an appropriate experimental set-up.
- Material flow and thermal analysis of the two dissimilar friction stir welded alloys may be performed with suitable techniques.
- Different joints of two dissimilar alloys may be joined by friction stir welding and welded joints properties may be analyzed.
- The analysis of variable thickness joints fabricated by friction stir welding of the two dissimilar alloys may be performed.

REFERENCES

[1] W. M. Thomas, E. D. Nicholas, J. C. Needham, M. G. Murch, P. Templesmith, and C. J. Dawes, "GB Patent application no. 9125978.8," *Int. Pat. Appl. No PCTGB9202203*, 1991.

[2] G. Buffa, A. Ducato, and L. Fratini, "FEM based prediction of phase transformations during Friction Stir Welding of Ti6Al4V titanium alloy," *Mater. Sci. Eng. A*, vol. 581, pp. 56–65, Oct. 2013, doi: 10.1016/j.msea.2013.06.009.

[3] W. M. Thomas, P. L. Threadgill, and E. D. Nicholas, "Feasibility of friction stir welding steel," *Sci. Technol. Weld. Join.*, vol. 4, no. 6, pp. 365–372, 1999.

[4] S. Mironov, Y. S. Sato, and H. Kokawa, "Development of grain structure during friction stir welding of pure titanium," *Acta Mater.*, vol. 57, no. 15, pp. 4519–4528, Sep. 2009, doi: 10.1016/j.actamat.2009.06.020.

[5] P. Heurtier, M. J. Jones, C. Desrayaud, J. H. Driver, F. Montheillet, and D. Allehaux, "Mechanical and thermal modelling of Friction Stir Welding," *J. Mater. Process. Technol.*, vol. 171, no. 3, pp. 348–357, 2006, doi: 10.1016/j.jmatprotec.2005.07.014.

[6] R. S. Mishra and M. W. Mahoney, "Friction Stir Welding and Processing. 2007," *Mater. Park OH ASM Int.*, 2007.

[7] D. Lohwasser and Z. Chen, *Friction stir welding: From basics to applications*. Elsevier, 2009.

[8] W. M. U. Thomas, E. D. Nicholas, A. Hall, and C. Cb, "Friction stir welding for the transportation industries," vol. 18, pp. 269–273, 1998.

[9] A. Heinz, A. Haszler, C. Keidel, S. Moldenhauer, R. Benedictus, and W. S. Miller, “Recent development in aluminium alloys for aerospace applications,” *Mater. Sci. Eng. A*, vol. 280, no. 1, pp. 102–107, 2000.

[10] J. R. Davis, *Alloying: understanding the basics*. ASM international, 2001.

[11] F. U. Zhi-Hong, H. Di-Qiu, and W. Hong, “Friction stir welding of aluminum alloys,” *J. Wuhan Univ. Technol.-Mater Sci Ed*, vol. 19, no. 1, pp. 61–64, 2004.

[12] R. S. Mishra and Z. Y. Ma, “Friction stir welding and processing,” *Mater. Sci. Eng. R Rep.*, vol. 50, no. 1–2, pp. 1–78, 2005, doi: 10.1016/j.mser.2005.07.001.

[13] V. Saravanan, S. Rajakumar, N. Banerjee, and R. Amuthakkannan, “Effect of shoulder diameter to pin diameter ratio on microstructure and mechanical properties of dissimilar friction stir welded AA2024-T6 and AA7075-T6 aluminum alloy joints,” *Int. J. Adv. Manuf. Technol.*, 2016, doi: 10.1007/s00170-016-8695-0.

[14] Esab, “Friction Stir Welding - the ESAB Way,” *Weld. J.*

[15] M. Ghosh, K. Kumar, S. V. Kailas, and A. K. Ray, “Optimization of friction stir welding parameters for dissimilar aluminum alloys,” *Mater. Des.*, vol. 31, no. 6, pp. 3033–3037, 2010.

[16] R. Palanivel, P. Koshy Mathews, N. Murugan, and I. Dinaharan, “Effect of tool rotational speed and pin profile on microstructure and tensile strength of dissimilar friction stir welded AA5083-H111 and AA6351-T6 aluminum alloys,” *Mater. Des.*, vol. 40, pp. 7–16, Sep. 2012, doi: 10.1016/j.matdes.2012.03.027.

[17] M. Koilraj, V. Sundareswaran, S. Vijayan, and S. K. Rao, “Friction stir welding of dissimilar aluminum alloys AA2219 to AA5083–Optimization of process parameters using Taguchi technique,” *Mater. Des.*, vol. 42, pp. 1–7, 2012.

[18] J. F. Guo, H. C. Chen, C. N. Sun, G. Bi, Z. Sun, and J. Wei, “Friction stir welding of dissimilar materials between AA6061 and AA7075 Al alloys effects of process parameters,” *Mater. Des. 1980-2015*, vol. 56, pp. 185–192, 2014.

[19] Y. S. Sato, M. Urata, and H. Kokawa, “Parameters controlling microstructure and hardness during friction-stir welding of precipitation-hardenable aluminum alloy 6063,” *Metall. Mater. Trans. A*, vol. 33, no. 3, pp. 625–635, 2002.

[20] M. N. James, D. G. Hattingh, and G. R. Bradley, “Weld tool travel speed effects on fatigue life of friction stir welds in 5083 aluminium,” *Int. J. Fatigue*, vol. 25, no. 12, pp. 1389–1398, 2003.

[21] M. Ericsson, “Influence of welding speed on the fatigue of friction stir welds, and comparison with MIG and TIG,” *Int. J. Fatigue*, vol. 25, no. 12, pp. 1379–1387, 2003, doi: 10.1016/S0142-1123(03)00059-8.

[22] M. Peel, A. Steuwer, M. Preuss, and P. J. Withers, “Microstructure, mechanical properties and residual stresses as a function of welding speed in aluminium AA5083 friction stir welds,” *Acta Mater.*, vol. 51, no. 16, pp. 4791–4801, 2003.

[23] S. Lim, S. Kim, C.-G. Lee, and S. Kim, “Tensile behavior of friction-stri-welded Al 6061-T651,” *Metall. Mater. Trans. A*, vol. 35, no. 9, pp. 2829–2835, 2004.

[24] S. Lim, S. Kim, C.-G. Lee, and S. J. Kim, “Mechanical properties of friction stir welded Al alloys with different hardening mechanisms,” *Met. Mater. Int.*, vol. 11, no. 2, p. 113, 2005.

[25] P. Cavaliere, G. Campanile, F. Panella, and a. Squillace, “Effect of welding parameters on mechanical and microstructural properties of AA6056 joints produced by Friction Stir Welding,” *J. Mater. Process. Technol.*, vol. 180, pp. 263–270, 2006, doi: 10.1016/j.jmatprotec.2006.06.015.

[26] S. R. Ren, Z. Y. Ma, and L. Q. Chen, “Effect of welding parameters on tensile properties and fracture behavior of friction stir welded Al – Mg – Si alloy,” vol. 56, pp. 69–72, 2007, doi: 10.1016/j.scriptamat.2006.08.054.

[27] A. H. Feng, D. L. Chen, and Z. Y. Ma, “Effect of welding parameters on microstructure and tensile properties of friction stir welded 6061 Al joints,” in *Materials Science Forum*, 2009, vol. 618, pp. 41–44.

[28] W. Xu, J. Liu, G. Luan, and C. Dong, “Microstructure and mechanical properties of friction stir welded joints in 2219-T6 aluminum alloy,” *Mater. Des.*, vol. 30, no. 9, pp. 3460–3467, 2009.

[29] S. Cui, Z. W. Chen, and J. D. Robson, “A model relating tool torque and its associated power and specific energy to rotation and forward speeds during friction stir welding/processing,” *Int. J. Mach. Tools Manuf.*, vol. 50, no. 12, pp. 1023–1030, 2010.

[30] G. Singh, K. Singh, and J. Singh, “Effect of process parameters on microstructure and mechanical properties in friction stir welding of aluminum alloy,” *Trans. Indian Inst. Met.*, vol. 64, no. 4–5, pp. 325–330, 2011.

[31] S. M. Chowdhury, D. L. Chen, S. D. Bhole, and X. Cao, “Tensile properties of a friction stir welded magnesium alloy: Effect of pin tool thread orientation and weld pitch,” *Mater. Sci. Eng. A*, vol. 527, no. 21–22, pp. 6064–6075, 2010.

[32] M. J. Peel, A. Steuwer, P. J. Withers, T. Dickerson, Q. Shi, and H. Shercliff, “Dissimilar friction stir welds in AA5083-AA6082. Part I: process parameter effects on thermal history and weld properties,” *Metall. Mater. Trans. A*, vol. 37, no. 7, pp. 2183–2193, 2006.

[33] S. T. Amancio-Filho, S. Sheikhi, J. F. dos Santos, and C. Bolfarini, “Preliminary study on the microstructure and mechanical properties of dissimilar friction stir welds in aircraft aluminium alloys 2024-T351 and 6056-T4,” *J. Mater. Process. Technol.*, vol. 206, no. 1–3, pp. 132–142, 2008, doi: 10.1016/j.jmatprotec.2007.12.008.

[34] A. Steuwer, M. J. Peel, and P. J. Withers, “Dissimilar friction stir welds in AA5083–AA6082: the effect of process parameters on residual stress,” *Mater. Sci. Eng. A*, vol. 441, no. 1–2, pp. 187–196, 2006.

[35] N. Rajamanickam, V. Balusamy, G. M. Reddy, and K. Natarajan, “Effect of process parameters on thermal history and mechanical properties of friction stir welds,” *Mater. Des.*, vol. 30, no. 7, pp. 2726–2731, 2009.

[36] M. A. Gharacheh, A. H. Kokabi, G. H. Daneshi, B. Shalchi, and R. Sarrafi, “The influence of the ratio of ‘rotational speed/traverse speed’($ømega$/v) on mechanical properties of AZ31 friction stir welds,” *Int. J. Mach. Tools Manuf.*, vol. 46, no. 15, pp. 1983–1987, 2006.

[37] L. Commin, M. Dumont, J.-E. Masse, and L. Barrallier, “Friction stir welding of AZ31 magnesium alloy rolled sheets: Influence of processing parameters,” *Acta Mater.*, vol. 57, no. 2, pp. 326–334, 2009.

[38] X. Cao and M. Jahazi, “Effect of tool rotational speed and probe length on lap joint quality of a friction stir welded magnesium alloy,” *Mater. Des.*, vol. 32, no. 1, pp. 1–11, 2011.

[39] H. Rezaei, M. H. Mirbeik, and H. Bisadi, “Effect of rotational speeds on microstructure and mechanical properties of friction stir-welded 7075-T6 aluminium alloy,” *Proc. Inst. Mech. Eng. Part C J. Mech. Eng. Sci.*, vol. 225, no. 8, pp. 1761–1773, 2011.

[40] J.-H. Cho, S. H. Han, and C. G. Lee, “Cooling effect on microstructure and mechanical properties during friction stir welding of Al-Mg-Si aluminum alloys,” *Mater. Lett.*, vol. 180, pp. 157–161, 2016.

[41] A. Goyal and R. K. Garg, “Effect of tool rotational and transverse speed on mechanical properties of friction stir welded AA5086-H32 aluminium alloy,” *Int. J. Microstruct. Mater. Prop.*, vol. 12, no. 1–2, pp. 79–93, 2017.

[42] M. A. Wahid, Z. A. Khan, A. N. Siddiquee, R. Shandley, and N. Sharma, “Analysis of process parameters effects on underwater friction stir welding of aluminum alloy 6082-T6,” *Proc. Inst. Mech. Eng. Part B J. Eng. Manuf.*, vol. 233, no. 6, pp. 1700–1710, 2019.

[43] M. Melendez, W. Tang, C. Schmidt, J. C. McClure, A. C. Nunes, and L. E. Murr, “Tool forces developed during friction stir welding,” 2003.

[44] K. Kumar and S. V. Kailas, “On the role of axial load and the effect of interface position on the tensile strength of a friction stir welded aluminium alloy,” *Mater. Des.*, vol. 29, no. 4, pp. 791–797, 2008.

[45] S. Rajakumar, C. Muralidharan, and V. Balasubramanian, “Predicting tensile strength, hardness and corrosion rate of friction stir welded AA6061-T6 aluminium alloy joints,” *Mater. Des.*, vol. 32, no. 5, pp. 2878–2890, 2011.

[46] A. R. Rose, K. Manisekar, and V. Balasubramanian, “Effect of axial force on microstructure and tensile properties of friction stir welded AZ61A magnesium alloy,” *Trans. Nonferrous Met. Soc. China*, vol. 21, no. 5, pp. 974–984, 2011.

[47] K. P. Mehta and V. J. Badheka, “Effects of tilt angle on the properties of dissimilar friction stir welding copper to aluminum,” *Mater. Manuf. Process.*, vol. 31, no. 3, pp. 255–263, 2016.

[48] A. Arici and S. Selale, “Effects of tool tilt angle on tensile strength and fracture locations of friction stir welding of polyethylene,” *Sci. Technol. Weld. Join.*, vol. 12, no. 6, pp. 536–539, 2007.

[49] K. R. Seighalani, M. B. Givi, A. M. Nasiri, and P. Bahemmat, “Investigations on the effects of the tool material, geometry, and tilt angle on friction stir welding of pure titanium,” *J. Mater. Eng. Perform.*, vol. 19, no. 7, pp. 955–962, 2010.

[50] G. H. Payganeh, N. M. Arab, Y. D. Asl, F. A. Ghasemi, and M. S. Boroujeni, “Effects of friction stir welding process parameters on appearance and strength of polypropylene composite welds,” *Int. J. Phys. Sci.*, vol. 6, no. 19, pp. 4595–4601, 2011.

[51] S. Zhang, Q. Shi, Q. Liu, R. Xie, G. Zhang, and G. Chen, “Effects of tool tilt angle on the in-process heat transfer and mass transfer during friction stir welding,” *Int. J. Heat Mass Transf.*, vol. 125, pp. 32–42, 2018.

[52] M. Elyasi, H. Aghajani Derazkola, and M. Hosseinzadeh, “Investigations of tool tilt angle on properties friction stir welding of A441 AISI to AA1100 aluminium,” *Proc. Inst. Mech. Eng. Part B J. Eng. Manuf.*, vol. 230, no. 7, pp. 1234–1241, 2016.

[53] S. D. Meshram and G. M. Reddy, “Influence of Tool Tilt Angle on Material Flow and Defect Generation in Friction Stir Welding of AA2219.,” *Def. Sci. J.*, vol. 68, no. 5, 2018.

[54] C. Rajendran, K. Srinivasan, V. Balasubramanian, H. Balaji, and P. Selvaraj, “Effect of tool tilt angle on strength and microstructural characteristics of friction stir welded lap joints of AA2014-T6 aluminum alloy,” *Trans. Nonferrous Met. Soc. China*, vol. 29, no. 9, pp. 1824–1835, 2019.

[55] A. Banik, B. S. Roy, J. D. Barma, and S. C. Saha, “An experimental investigation of torque and force generation for varying tool tilt angles and their effects on microstructure and mechanical properties: Friction stir welding of AA 6061-T6,” *J. Manuf. Process.*, vol. 31, pp. 395–404, 2018.

[56] J. Kundu and H. Singh, “Friction stir welding of dissimilar Al alloys: effect of process parameters on mechanical properties,” *Eng. Solid Mech.*, vol. 4, no. 3, pp. 125–132, 2016.

[57] A. K. Lakshminarayanan and V. Balasubramanian, “Process parameters optimization for friction stir welding of RDE-40 aluminium alloy using Taguchi technique,” *Trans. Nonferrous Met. Soc. China*, vol. 18, no. 3, pp. 548–554, 2008.

[58] S. Rajakumar, C. Muralidharan, and V. Balasubramanian, “Influence of friction stir welding process and tool parameters on strength properties of AA7075-T6 aluminium alloy joints,” *Mater. Des.*, vol. 32, no. 2, pp. 535–549, 2011.

[59] N. Mendes, A. Loureiro, C. Martins, P. Neto, and J. N. Pires, “Effect of friction stir welding parameters on morphology and strength of acrylonitrile

butadiene styrene plate welds," *Mater. Des.*, vol. 58, pp. 457–464, 2014, doi: 10.1016/j.matdes.2014.02.036.

[60] V. Balasubramanian, "Relationship between base metal properties and friction stir welding process parameters," *Mater. Sci. Eng. A*, vol. 480, no. 1–2, pp. 397–403, 2008.

[61] K. Elangovan, V. Balasubramanian, and S. Babu, "Predicting tensile strength of friction stir welded AA6061 aluminium alloy joints by a mathematical model," *Mater. Des.*, vol. 30, no. 1, pp. 188–193, 2009.

[62] H. A. Derazkola and A. Simchi, "An investigation on the dissimilar friction stir welding of T-joints between AA5754 aluminum alloy and poly (methyl methacrylate)," *Thin-Walled Struct.*, vol. 135, pp. 376–384, 2019.

[63] K. K. Ramachandran, N. Murugan, and S. S. Kumar, "Friction stir welding of aluminum alloy AA5052 and HSLA steel," *Weld J*, vol. 94, no. 9, 2015.

[64] Y. Zhao, S. Lin, L. Wu, and F. Qu, "The influence of pin geometry on bonding and mechanical properties in friction stir weld 2014 Al alloy," *Mater. Lett.*, vol. 59, no. 23, pp. 2948–2952, 2005.

[65] H. Fujii, L. Cui, M. Maeda, and K. Nogi, "Effect of tool shape on mechanical properties and microstructure of friction stir welded aluminum alloys," *Mater. Sci. Eng. A*, vol. 419, no. 1–2, pp. 25–31, 2006.

[66] A. Scialpi, L. A. C. De Filippis, and P. Cavaliere, "Influence of shoulder geometry on microstructure and mechanical properties of friction stir welded 6082 aluminium alloy," *Mater. Des.*, vol. 28, no. 4, pp. 1124–1129, 2007, doi: 10.1016/j.matdes.2006.01.031.

[67] F. C. Liu and Z. Y. Ma, “Influence of Tool Dimension and Welding Parameters on Microstructure and Mechanical Properties of Friction-Stir-Welded 6061-T651 Aluminum Alloy,” 2008, doi: 10.1007/s11661-008-9586-2.

[68] K. Elangovan, V. Balasubramanian, and M. Valliappan, “Effect of tool pin profile and tool rotational speed on mechanical properties of friction stir welded AA6061 aluminium alloy,” *Mater. Manuf. Process.*, vol. 23, no. 3, pp. 251–260, 2008.

[69] K. Kumar, S. V. Kailas, and T. S. Srivatsan, “Influence of tool geometry in friction stir welding,” *Mater. Manuf. Process.*, vol. 23, no. 2, pp. 188–194, 2008.

[70] C. N. Suresha, B. M. Rajaprakash, and S. Upadhya, “A study of the effect of tool pin profiles on tensile strength of welded joints produced using friction stir welding process,” *Mater. Manuf. Process.*, vol. 26, no. 9, pp. 1111–1116, 2011.

[71] L. Trueba Jr, G. Heredia, D. Rybicki, and L. B. Johannes, “Effect of tool shoulder features on defects and tensile properties of friction stir welded aluminum 6061-T6,” *J. Mater. Process. Technol.*, vol. 219, pp. 271–277, 2015.

[72] K. K. Mugada and K. Adepu, “Influence of ridges shoulder with polygonal pins on material flow and friction stir weld characteristics of 6082 aluminum alloy,” *J. Manuf. Process.*, vol. 32, pp. 625–634, 2018.

[73] K. K. Mugada and K. Adepu, “Influence of tool shoulder end features on friction stir weld characteristics of Al-Mg-Si alloy,” *Int. J. Adv. Manuf. Technol.*, vol. 99, no. 5–8, pp. 1553–1566, 2018.

[74] K. K. Mugada and K. Adepu, “Effect of knurling shoulder design with polygonal pins on material flow and mechanical properties during friction stir welding of Al–Mg–Si alloy,” *Trans. Nonferrous Met. Soc. China*, vol. 29, no. 11, pp. 2281–2289, 2019.

[75] Y. K. Periyasamy, A. V. Perumal, and B. K. Periyasamy, “Influence of Tool Shoulder Concave Angle and Pin Profile on Mechanical Properties and Microstructural Behaviour of Friction Stir Welded AA7075-T651 and AA6061 Dissimilar Joint,” *Trans. Indian Inst. Met.*, vol. 72, no. 4, pp. 1087–1109, 2019.

[76] K. Panneerselvam and K. Lenin, “Joining of Nylon 6 plate by friction stir welding process using threaded pin profile,” *Mater. Des.*, vol. 53, pp. 302–307, 2014.

[77] S. J. Vijay and N. Murugan, “Influence of tool pin profile on the metallurgical and mechanical properties of friction stir welded Al–10 wt.% TiB2 metal matrix composite,” *Mater. Des.*, vol. 31, no. 7, pp. 3585–3589, 2010.

[78] A. Kumar and L. S. Raju, “Influence of tool pin profiles on friction stir welding of copper,” *Mater. Manuf. Process.*, vol. 27, no. 12, pp. 1414–1418, 2012.

[79] P. Motalleb-Nejad, T. Saeid, A. Heidarzadeh, K. Darzi, and M. Ashjari, “Effect of tool pin profile on microstructure and mechanical properties of friction stir welded AZ31B magnesium alloy,” *Mater. Des.*, vol. 59, pp. 221–226, 2014.

[80] J. Marzbanrad, M. Akbari, P. Asadi, and S. Safaee, “Characterization of the Influence of Tool Pin Profile on Microstructural and Mechanical Properties of Friction Stir Welding,” *Metall. Mater. Trans. B Process Metall. Mater. Process. Sci.*, vol. 45, no. 5, pp. 1887–1894, 2014, doi: 10.1007/s11663-014-0089-9.

[81] S. Shanavas and J. E. R. Dhas, “Parametric optimization of friction stir welding parameters of marine grade aluminium alloy using response surface methodology,” *Trans. Nonferrous Met. Soc. China*, vol. 27, no. 11, pp. 2334–2344, 2017.

[82] H. J. Liu, H. Fujii, M. Maeda, and K. Nogi, “Tensile properties and fracture locations of friction-stir-welded joints of 2017-T351 aluminum alloy,” vol. 142, no. 2003, pp. 692–696, 2017, doi: 10.1016/S0924-0136(03)00806-9.

[83] A. Heidarzadeh, H. Khodaverdizadeh, A. Mahmoudi, and a E. Nazari, “Tensile behavior of friction stir welded AA 6061-T4 aluminum alloy joints,” *Mater. Des.*, vol. 37, pp. 166–173, 2012.

[84] M. Szkodo, J. Adamowski, and A. Sitko, “Assessment of FSW welds made of aluminum alloy AW7075-T651,” *Solid State Phenom.*, vol. 165, no. June 2010, pp. 201–206, 2010, doi: 10.4028/www.scientific.net/SSP.165.201.

[85] A. Silva-Magalhães, J. De Backer, J. Martin, and G. Bolmsjö, “In-situ temperature measurement in friction stir welding of thick section aluminium alloys,” *J. Manuf. Process.*, vol. 39, pp. 12–17, 2019.

[86] J. Kundu and H. Singh, “Modelling and analysis of process parameters in friction stir welding of AA5083-H321 using response surface methodology,” *Adv. Mater. Process. Technol.*, vol. 4, no. 2, pp. 183–199, 2018.

[87] K. Boulahem, S. B. Salem, and J. Bessrour, “Prediction model of ultimate tensile strength and investigation on microstructural characterization of friction stir welded AA2024-T3,” *Int. J. Adv. Manuf. Technol.*, vol. 95, no. 1–4, pp. 1473–1486, 2018.

[88] M. P. Iqbal, R. Jain, and S. K. Pal, “Numerical and experimental study on friction stir welding of aluminum alloy pipe,” *J. Mater. Process. Technol.*, vol. 274, p. 116258, Dec. 2019, doi: 10.1016/j.jmatprotec.2019.116258.

[89] N. Z. Khan, A. N. Siddiquee, Z. A. Khan, and A. K. Mukhopadhyay, “Mechanical and microstructural behavior of friction stir welded similar and

dissimilar sheets of AA2219 and AA7475 aluminium alloys," *J. Alloys Compd.*, vol. 695, pp. 2902–2908, 2017.

[90] A. Scialpi, M. De Giorgi, L. A. C. De Filippis, R. Nobile, and F. W. Panella, "Mechanical analysis of ultra-thin friction stir welding joined sheets with dissimilar and similar materials," *Mater. Des.*, vol. 29, no. 5, pp. 928–936, 2008, doi: 10.1016/j.matdes.2007.04.006.

[91] P. Cavaliere, E. Cerri, and A. Squillace, "Mechanical response of 2024-7075 aluminium alloys joined by Friction Stir Welding," *J. Mater. Sci.*, vol. 40, no. 14, pp. 3669–3676, 2005.

[92] N. T. Kumbhar and K. Bhanumurthy, "Friction stir welding of Al 5052 with Al 6061 alloys," *J. Metall.*, vol. 2012, 2012.

[93] P. M. G. P. Moreira, A. M. P. de Jesus, A. S. Ribeiro, and P. M. S. T. de Castro, "Fatigue crack growth in friction stir welds of 6082-T6 and 6061-T6 aluminium alloys: A comparison," *Theor. Appl. Fract. Mech.*, vol. 50, no. 2, pp. 81–91, 2008, doi: 10.1016/j.tafmec.2008.07.007.

[94] P. L. Threadgill, M. M. Z. Ahmed, J. P. Martin, J. G. Perrett, and B. P. Wynne, "The use of bobbin tools for friction stir welding of aluminium alloys," in *Materials Science Forum*, 2010, vol. 638, pp. 1179–1184.

[95] C. Leitão, R. Louro, and D. M. Rodrigues, "Analysis of high temperature plastic behaviour and its relation with weldability in friction stir welding for aluminium alloys AA5083-H111 and AA6082-T6," *Mater. Des.*, vol. 37, pp. 402–409, 2012.

[96] M. I. Costa, D. Verdera, C. Leitão, and D. M. Rodrigues, "Dissimilar friction stir lap welding of AA 5754-H22/AA 6082-T6 aluminium alloys: Influence of

material properties and tool geometry on weld strength," *Mater. Des.*, vol. 87, pp. 721–731, 2015.

[97] S.-K. Park, S.-T. Hong, J.-H. Park, K.-Y. Park, Y.-J. Kwon, and H.-J. Son, "Effect of material locations on properties of friction stir welding joints of dissimilar aluminium alloys," *Sci. Technol. Weld. Join.*, vol. 15, no. 4, pp. 331–336, 2010.

[98] L. H. A. Shah, S. Sonbolestan, A. R. Midawi, S. Walbridge, and A. Gerlich, "Dissimilar friction stir welding of thick plate AA5052-AA6061 aluminum alloys: effects of material positioning and tool eccentricity," *Int. J. Adv. Manuf. Technol.*, vol. 105, no. 1–4, pp. 889–904, 2019.

[99] Y. K. Periyasamy, A. V. Perumal, and B. K. Periyasamy, "Optimization of process parameters on friction stir welding of AA7075-T651 and AA6061 joint using response surface methodology," *Mater. Res. Express*, vol. 6, no. 9, p. 096558, 2019.